E.O. Paton Electric Welding Institute of the National Academy of Science of Ukraine
International Association “Welding”

The Paton Welding Journal

07
2025

International Scientific-Technical and Production Journal ♦ Founded in January 2000 (12 Issues Per Year)

Address of Editorial Office:
E.O. Paton Electric Welding Institute, 11 Kazymyr Malevych Str., 03150, Kyiv, Ukraine
E-mail: office@paton.kiev.ua; https://paton.org.ua/en/

Address of Publisher:
International Association “Welding”, 11 Kazymyr Malevych Str., 03150, Kyiv, Ukraine
Tel.: (38044) 205 23 90, E-mail: patonpublishinghouse@gmail.com; journal@paton.kiev.ua
https://patonpublishinghouse.com/eng/journals/tpwj

The Journal was registered by the National Council of Ukraine on Television and Radio Broadcasting on 09.05.2024, carrier identifier R30-04569
ISSN 0957-798X (Print), ISSN 3041-2293 (Online)
DOI: https://doi.org/10.37434/tpwj, from #01, 2020 to now; DOI: https: //doi.org/10.15407/tpwj from #01, 2014 to #12, 2019.

Subscriptions, 12 issues per year:
348 Euro — annual subscription for the printed (hard copy) version, air postage and packaging included;
288 Euro — annual subscription for the electronic version (sending issues in pdf format or providing access to IP addresses).

Representative Offices of “The Paton Welding Journal”:

BRAZIL, Arc Dynamics
Address: Nova Iguacu, Rio de Janeiro, Brazil
Daniel Adolpho, Tel.: +55 21 9 6419 5703,
E-mail: dadolpho@arcdynamics.com.br

CHINA, China-Ukraine Institute of Welding, Guangdong Academy of Sciences
Address: Room 210, No. 363 Changxing Road, Tianhe, Guangzhou, 510650, China
Zhang Yupeng, Tel.: +86-20-61086791,
E-mail: patonjournal@gwi.gd.cn

BULGARIA, Bulgarian Welding Society
Address: Blvd. Asen Yordanov No.10, Sofia 1592, Bulgaria
Pavel Popgeorgiev, Tel.: +359 899 96 22 20,
E-mail: office@bws-bg.org

POLAND, PATON EUROPE Sp. z o. o.
Address: ul. Kapitałowa 4, 35-213, Rzeszów, Poland
Anton Stepakhno, Tel.: +38067 509 95 67,
E-mail: Anton.Stepakhno@paton.ua

The content of the Journal includes articles received from authors from around the world in the field of welding, cutting, cladding, soldering, brazing, coating, 3D additive technologies, electrometallurgy, material science, NDT and selectively includes translations into English of articles from the following journals, published in Ukrainian:

- «Avtomatychne Zvaryuvannya» (Automatic Welding), https://patonpublishinghouse.com/eng/journals/as;
- «Suchasna Elektrometalurhiya» (Electrometallurgy Today), https://patonpublishinghouse.com/eng/journals/sem;
- «Tekhnichna Diahnostyka ta Neruinivnyi Kontrol» (Technical Diagnostics & Nondestructive Testing), https://patonpublishinghouse.com/eng/journals/tdnk.

CONTENTS

ORIGINAL ARTICLES

*Translated Article(s) from “Avtomatychne Zvaryuvannya” (Automatic Welding), No. 3, 2025.

**Translated Article(s) from “Tekhnichna Diahnostyka ta Neruinivnyi Kontrol” (Technical Diagnostics & Nondestructive Testing), No. 2, 2025.

***Translated Article(s) from “Tekhnichna Diahnostyka ta Neruinivnyi Kontrol” (Technical Diagnostics & Nondestructive Testing), No. 1, 2025.

Indexing: The electronic edition of the Journal is stored in the V.I. Vernadsky National Library of Ukraine (eVerLib), included in the OPEN UKRAINIAN CITATION INDEX database and international databases: CROSSREF, EBSCO, Google Scholar, INDEX COPERNICUS, ULRICHSWEB.

DOI: https://doi.org/10.37434/tpwj2025.07.01

EFFECTIVENESS OF APPLICATION OF PULSED MODE OF ARC BURNING IN WET UNDERWATER WELDING

S. Maksymov, D. Krazhanovskyi

E.O. Paton Electric Welding Institute of the NASU
11 Kazymyr Malevych Str., 03150, Kyiv, Ukraine

ABSTRACT

A comparative analysis of methods for implementing the pulsed nature of arc burning — pulsed-arc welding by changing the shape of the external volt-ampere characteristic of the power source and pulsed wire feeding and their parameters when welding with flux-cored wire with a non-stationary arc in an aqueous environment was carried out. The results obtained showed the greater efficiency of using pulsed welding wire feed: the coefficient of variation in voltage decreases by 1.5 times, and the frequency of short circuits — by 2.5 times; the depth of penetration and reinforcement of the weld changes by 63 and 55 %, respectively; the transition of alloying elements C, Si, Mn and Ni increases by 38, 30, 47 and 35 %, respectively; a study of the hydrogenation mechanism during wet underwater welding showed that most of the hydrogen (60–70 %) enters the weld pool along with a drop of electrode metal, which is saturated with it from the atmosphere of the vapour-gas bubble. Pulse action shortens the lifetime of liquid metal at the droplet stage, which leads to a decrease in the hydrogen content in the weld metal by an average of 27 %.

KEYWORDS: wet underwater welding, flux-cored wire, pulsed mode, effectiveness

INTRODUCTION

Pulsed methods of controlling the welding process allow for improving the welded joint quality, performing adjustable heat input into the welded joint zone, regulating the electrode metal melting mode and formation of the structure of weld metal and heat-affected zone (HAZ), and reducing the burnout and spattering losses [1–5]. Pulsed-arc welding (PAW) is considered the best-known variant of adjusting the value of thermal energy input into the arc burning zone. In this case, the power source directly controls, according to a set program, the electric parameters of the welding arc, namely pause and pulse currents and their duration [6–10].

A power source with a flat volt-ampere characteristic (VAC) is usually used in flux-cored wire wet underwater welding. The range of welding current variation during welding can reach 150–200 A. The welding process proper is accompanied by periodical short-circuiting (Figure 1) [11–13]. Such a chaotic state partially depends on the specificity of the environment. In particular, in wet underwater welding, the process stability will be additionally influenced by the collapse of the vapour-gas bubble. Turbulent flows forming in this case,

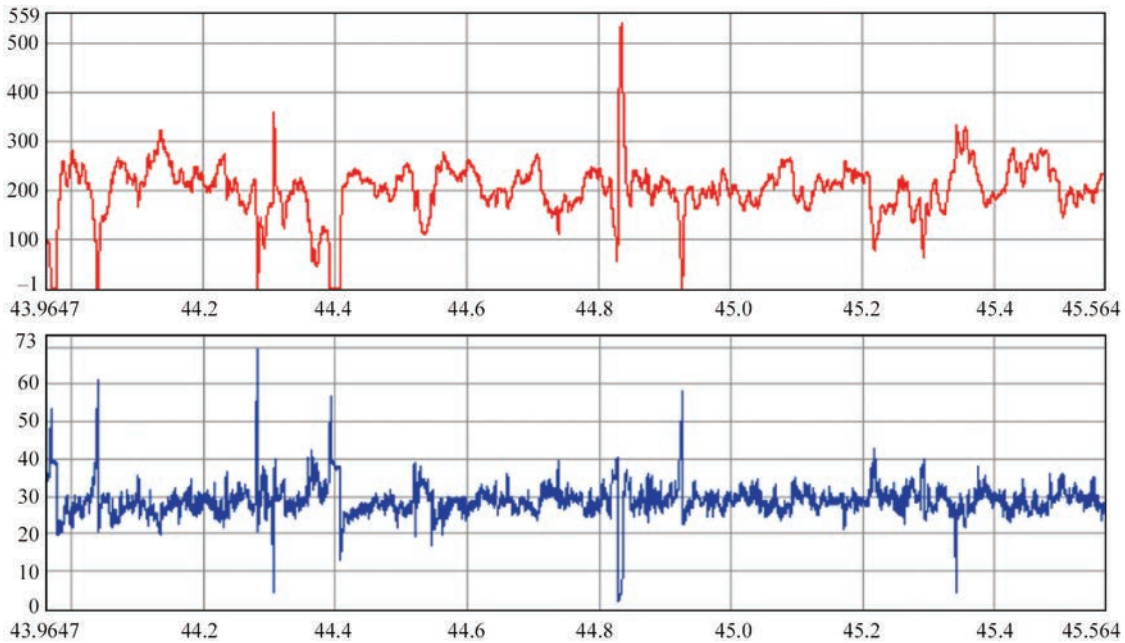

Figure 1. A typical oscillogram of the process of underwater welding with PPS-AN1 flux-cored wire

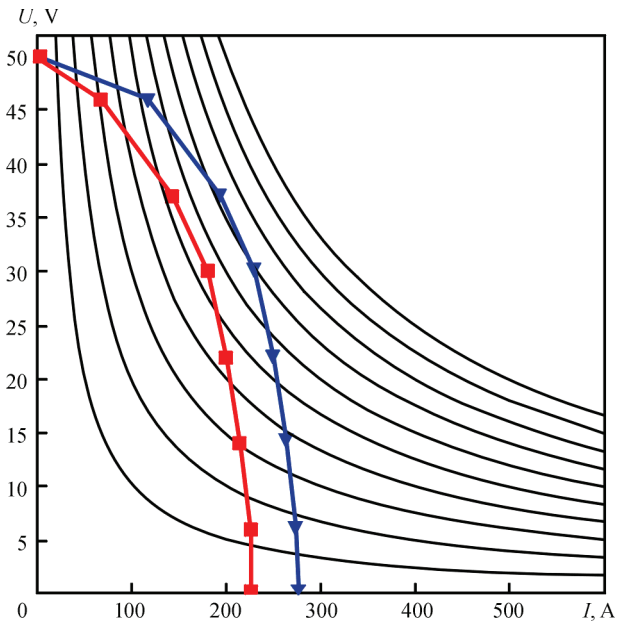

Figure 2. Example of VAC shape for pulsed welding

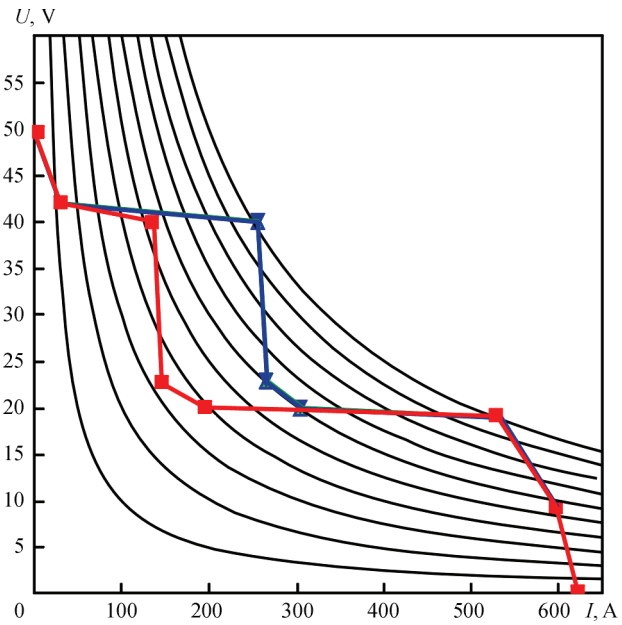

Figure 3. Example of VAC with shape correction

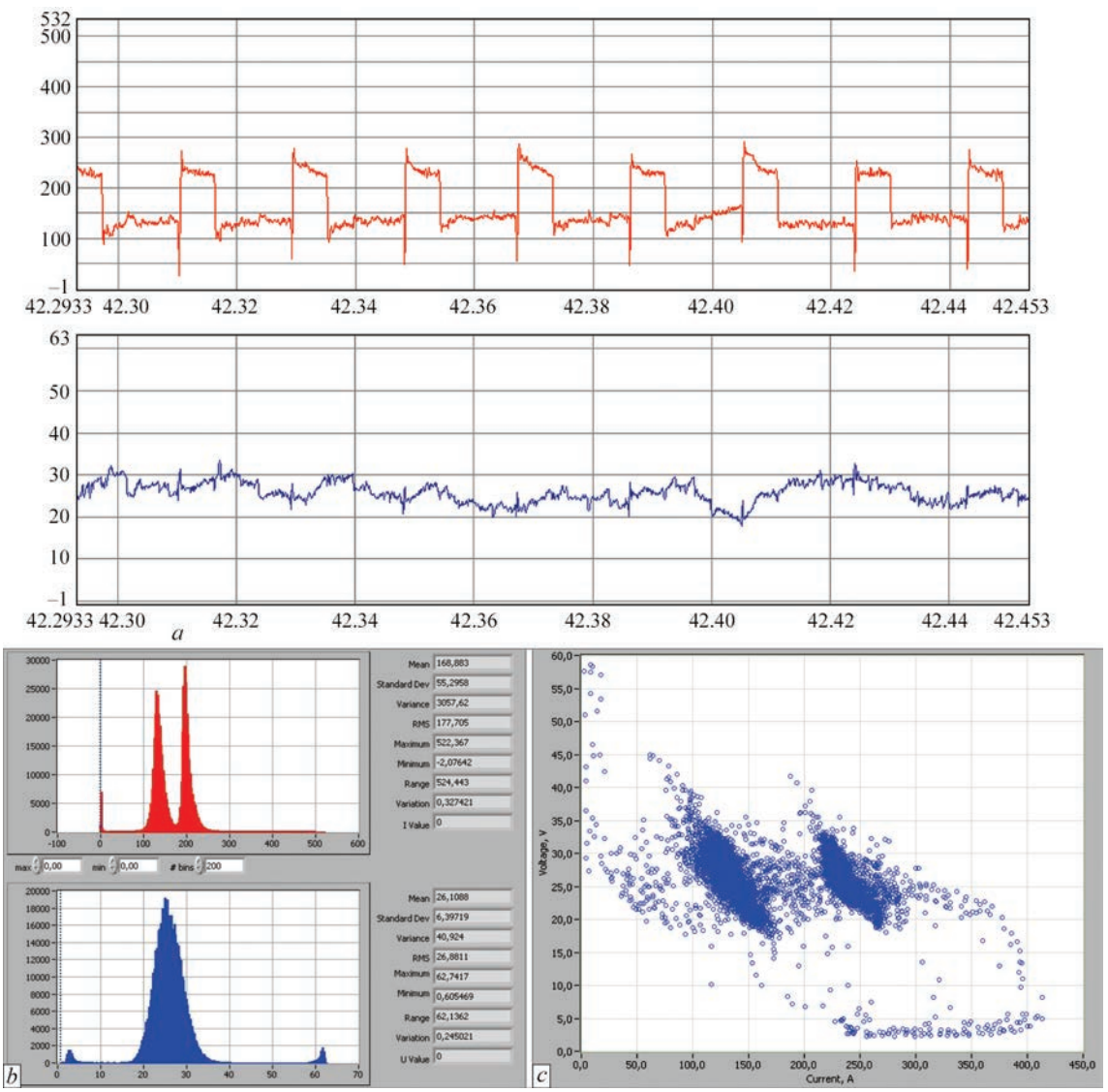

Figure 4. *a* — oscillogram of pulsed welding process, *b* — statistical data and *c* — the arc VAC

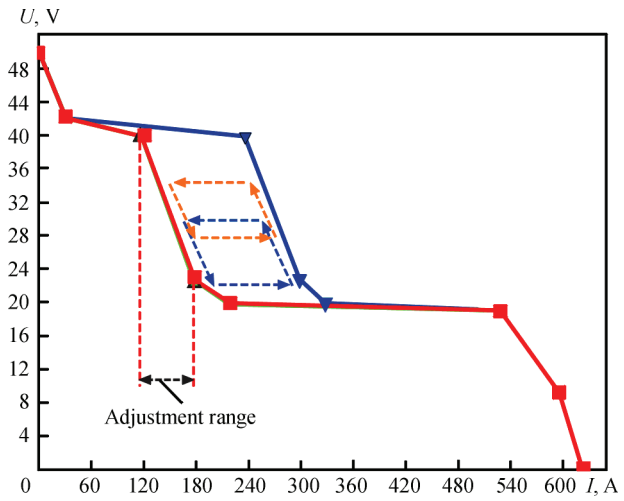

Figure 5. Variants of the trajectory, depending on wire feed rate and range of possible values

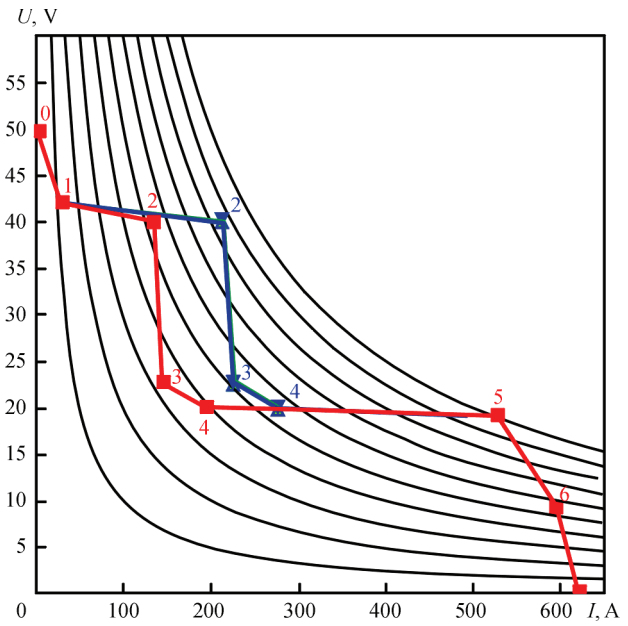

Figure 6. VAC sections for pulsed welding

throw the bubble up. As a result, part of the drops will be lost to spatter. When penetrating into the weld pool, the other part of the drops, usually after gaining a certain weight, causes disturbance on the latter's surface. Considering the high cooling rate, these disturbances do not have enough time to subside, and after solidification, we observe an irregularity of the weld surface.

The research aimed to conduct a comparative analysis of the methods for implementing the pulsed nature of arc burning — pulsed arc welding (PAW) — by changing the shape of the external volt-ampere characteristic (VAC) and the pulse feed of the welding wire (PFW) and their parameters when performing the flux-cored wire welding process with a non-stationary arc in an aqueous environment.

METHODS

LET-500 power source was used to solve the welding problem, which allows relatively flexible adjustment of most process parameters, including the shape of external volt-ampere characteristics [14, 15]. Its pulsed mode of operation enables using two such VACs, each with its own operating time, as shown in Figure 2. When switching from one characteristic to another, the welding current changes to the respective value for the currently used characteristic.

Previous experiments showed that this combination of VAC shapes is unstable and can lead to freezing and interruption of the welding process. To avoid such a situation, it is necessary to correct the VAC shape, by adding arc power at the moment close to the short-circuit (Figure 3). A typical oscillogram of the process, statistical data and VAC of the arc are shown in Figure 4. One can see from the oscillogram how the pulse-to-pause transition is realized. The Figure also shows the graphs of current and voltage distribution.

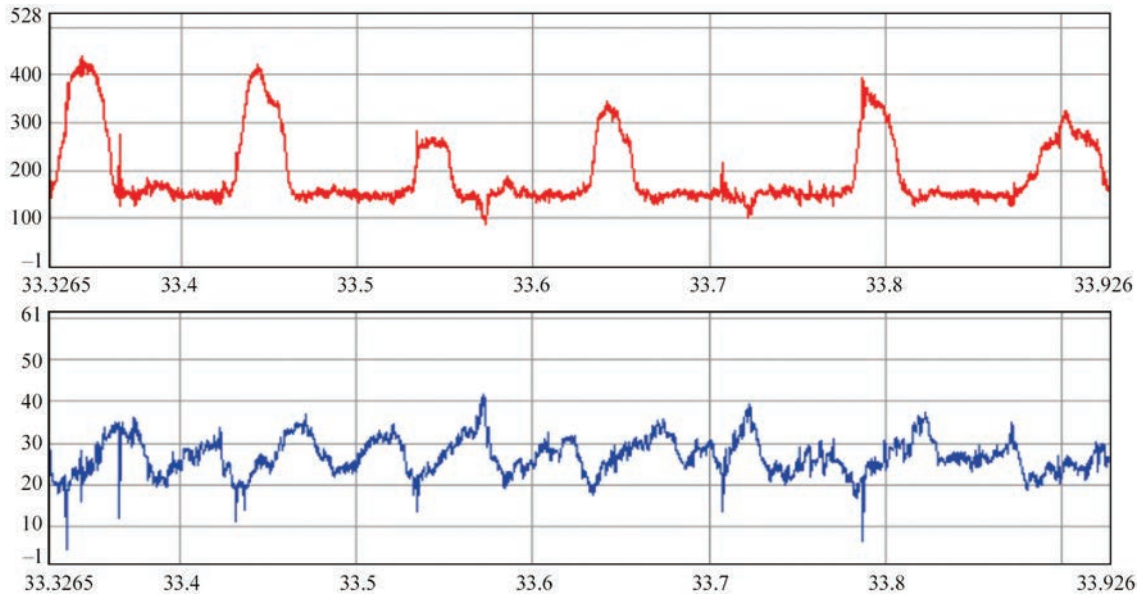

Figure 7. Oscillogram of the process of underwater welding with PWF (f = 20 Hz, S = 3.3)

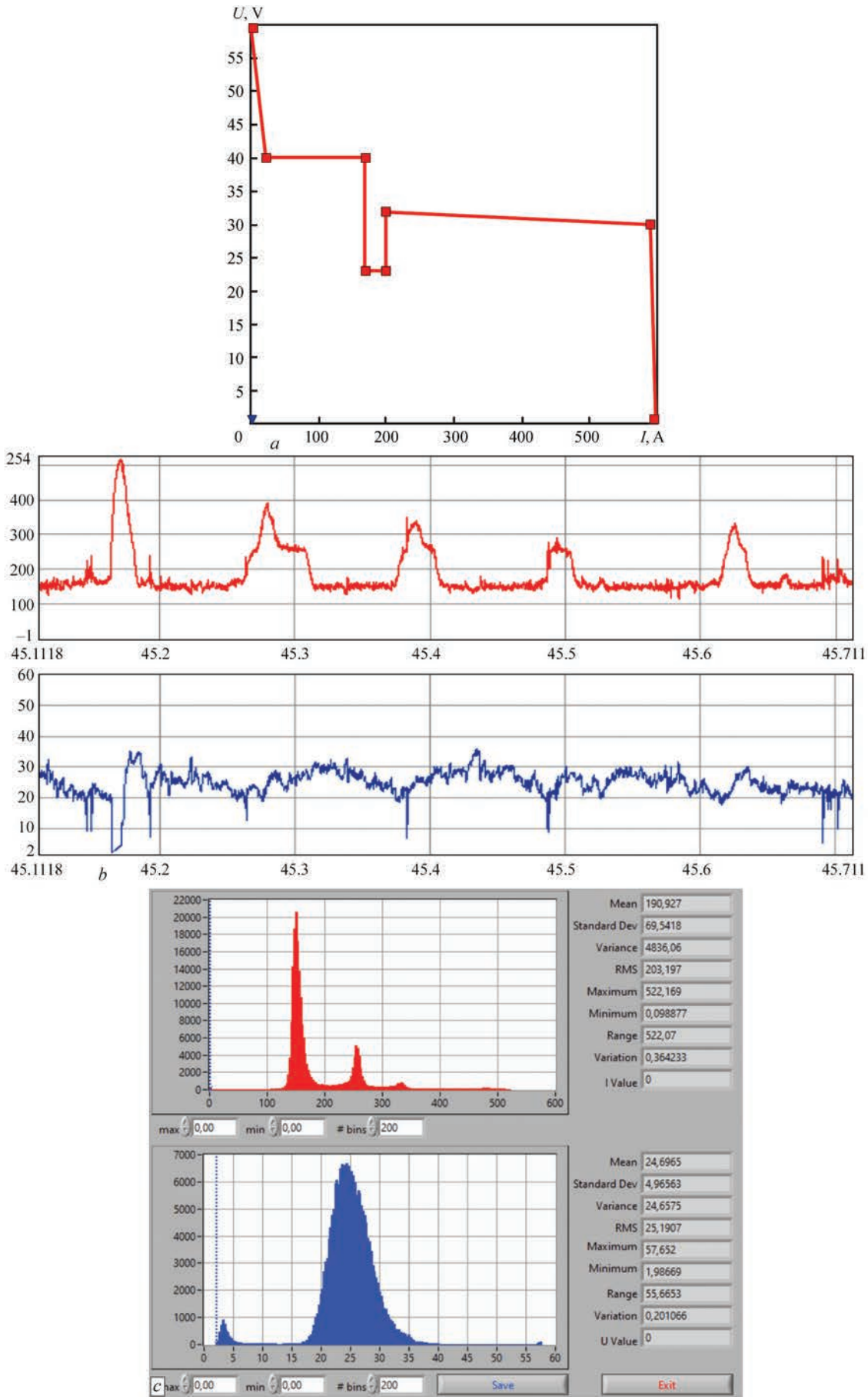

Figure 8. *a* — VAC for realization of the pulsed process based on the principle of pulsed self-regulation, *b* — oscillogram and *c* — histogram of the process of welding with this VAC

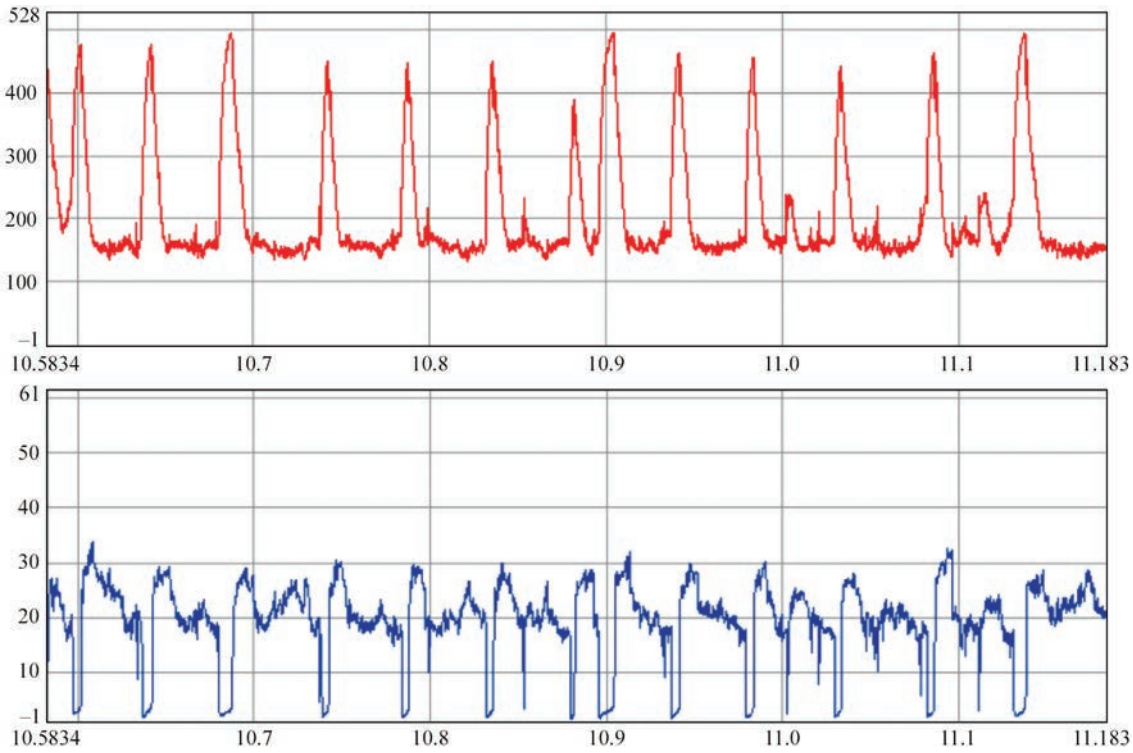

Figure 9. Oscillogram of the welding process with VAC based on the principle of pulsed self-regulation in combination with PWF (f = 20 Hz, S = 3.3)

Note that during welding, it is difficult for us to influence the arc directly. It can cause the formation of rolls and slag entrapment along the weld edges. To a greater extent, the voltage will depend on the distance from the molten electrode tip to the weld pool. At a constant feed rate, a current change promotes a change in the electrode melting rate. This leads to the electrode tip moving closer to or farther from the weld pool. Here, the working point of welding on the volt-ampere characteristic moves according to a trajectory shown in Figure 5. The resulting average voltage value is between the trajectory upper and lower boundaries. Given the above, we can influence the voltage in several ways. The first parameter that should be paid attention to is welding speed. A slight increase or decrease in the welding speed will shift the trajectory and, as a result, change the position of its boundaries. The second important factor is the slope and duration of the falling portion of the power source VAC. Adjustment sensitivity and its degree depend on it.

Pulse and pause current were determined by current in point 3 for the VAC blue and red line (Figure 6). Such selection is conditional, as more parameters should be taken into account for a more accurate determination. Despite that, the current in point 3 approximately coincides with peak values on current distribution graphs. To set a certain pulse or pause current, fixed region 2–3–4 was shifted along the horizontal.

Welding with pulsed welding wire feed (PWF) should be regarded as another variant with pulsed process of welding control [16–18]. This process is performed through adjustment of welding wire rate and duration of movement during the pulse and pause in the feed mechanism (Figure 7).

This process was realized by applying a drive based on a collectorless valve motor, which ensures both the pulsed and constant welding wire feed [19]. The range of feed frequency in the pulsed mode is from 1 up to 60 Hz, and the wire feed rate is up to 2280 m/h. Unlike PWF, where the power source is electronically controlled, and the process of switching from the pulse to pause runs instantly, a smooth change between these phases is observed in this process. This is due to the inertia of the system, which appropriately incorporates the engine, wire feed mechanism, and welding wire.

We should also mention welding with a broken VAC, which is based on the principle of pulsed self-regulation (Figure 8). In the current histogram (Figure 8, *b*), one can see an absence of arc breaks, unlike the regular process (Figure 1). The latter variant can be combined with the variant with PWF for more flexible control of the welding process (Figure 9).

The given examples and available equipment confirm that the specified welding and control modes ensure a pulsed process and also allow the following:

- establishing the value and duration of pause and pulse current for PWF.
- determining the rate and duration of the wire feed in the pause and pulse phase for welding with PWF. In this case, the pause current depends on the wire feed rate. Due to inertia, a smooth change of current and voltage parameters at the switching of pause and pulse phases is observed.

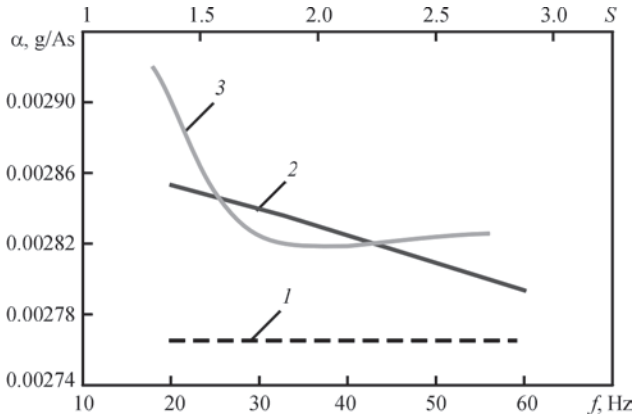

Figure 10. Dependence of deposition rate on the relative pulse duration (*S*) and frequency (*f*) of the process of welding with PWF: *1* — no pulse; *2* — *S* =3.3; *3* — *f* = 40 Hz

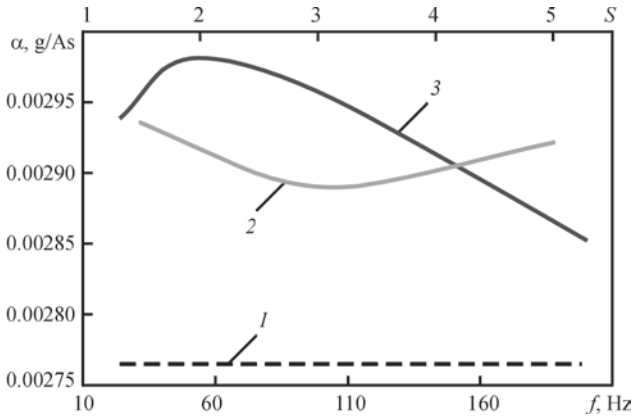

Figure 11. Dependence of deposition rate on relative pulse duration (*S*) and frequency (*f*) of the process for PWF: *1* — no pulse; *2* — *S* =2; *3* — *f* = 50 Hz

● pause current limiting by VAC falling portion for the welding variant with broken VAC. It provides a better-controlled process in combination with PWF. In this case, unlike the simple process with PWF, there is the possibility of a more accurate determination of the pause current. Unlike pulsed self-regulation, PWF enables more precise control of the process stability.

In order to assess the influence of pulsed actions on the efficiency of the process of flux-cored wire wet underwater welding, bead deposition on plates from 10 mm 09G2S steel was performed. During welding, the current and voltage signals were recorded for further processing. In order to increase the accuracy of the obtained results, the number of tests in one point was equal to 3. The derived data were used to plot the respective graphs of the dependencies.

RESULTS AND DISCUSSION

Results of measurements of the deposition rate are given in Figures 10 and 11. As one can see from the given data, with the pulsed nature of the arc burning, a slight increase in the amount of deposited metal is possible within 6–8 %.

To detect the influence of welding process parameters on weld geometry, the welding modes remained fixed: welding speed of 9 m/h with approximately the same average welding current of 185 A. Table 1 shows the degree of the influence of pulsed process parameters on weld dimensions for both the welding processes.

Obtained results demonstrate the possibility of adjustment of the geometrical parameters of the weld metal, using the pulsed process parameters in welding in an aqueous environment. Compared to PWF with the same current and voltage, applying pulsed wire feed allows a more significant impact on weld penetration depth and convexity in the frequency range from 20 to 60 Hz and relative pulse duration from 1.43 to 10 units. Compared to welding in the stationary mode, it is possible to control the penetration depth in the range from –18 up to +45 % and weld convexity in the range from –38 up to +17 %. The extent of influence on the weld width is small in both cases.

Table 1. Influence of pulsed process parameters on weld dimensions

Parameter	Welding with PWF			PAW		
	min, mm	max, mm	Influence, %	min, mm	max, mm	Influence, %
w	14	16.44	15.5	11.66	13.5	13.6
h	2.07	3.65	62.7	1.21	1.71	29.2
g	2.97	5.63	55.2	4,51	5.11	11.7

Table 2. Results of chemical composition analysis

No.	*f*, Hz	S	C, %	Si, %	Mn, %	Ni, %
1	–	–	0.08	0.02	0.17	1
2	40	1.43	0.08	0.018	0.11	0.9
3	40	3.33	0.1	0.021	0.18	1.35
4	40	10	0.11	0.02	0.25	1.26
5	20	3.33	0.06	0.018	0.2	0.8
6	60	3.33	0.11	0.026	0.21	1.3

Table 3. Diffusible hydrogen content in the deposited metal

No.	*f*, Hz	S	[H], cm³/100 g
1	–	–	30.55
2	40	1.43	31.2
3	40	3.33	28.14
4	40	5	35.4
5	20	3.33	27.3
6	60	3.33	22.17

The main elements in the analysis of the influence of the pulsed mode of arc burning were carbon, silicon, manganese and nickel, present in the composition of flux-cored wire. As shown by the obtained data (Table 2), the use of PWF, compared to welding with constant wire feed, allows controlling the deposited metal chemical composition in a wide range: C — –25 to +38, Si — –10 to +30, Mn — –35 to +47, Ni — –20 to +35 %.

The presence of high hydrogen content in the weld metal is a critical factor that significantly impairs the quality of the welded joint. This issue is particularly urgent in underwater welding, where, under otherwise equal conditions, the quantity of hydrogen in the weld metal is 1.5–1.9 times greater than under normal conditions. This increase is due to the high partial pressure of hydrogen in the arc atmosphere and the higher weld pool crystallization rate, both of which are unique to underwater welding. Addressing this issue is crucial to improving the quality and reliability of underwater welds.

Pulsed welding processes influence the energy input, arc length, time of existence of molten metal pool, etc., which, in turn, determines weld metal saturation with hydrogen. Knowing the nature of this influence, it is possible to predict the probability of forming of the defects (pores, cold cracks, etc.), which impair the welded joint properties.

The chromatographic method was used to determine the diffusible hydrogen content $[H]_{dif}$ in the deposited metal. The deposition was performed on 10×15×25 mm samples, which were placed into gas analyzer chambers immediately after welding. The process with pulsed feed of flux-cored wire turned out to be more effective: total hydrogen content decreased by 37 % on average. Table 3 gives the results of $[H]_{dif}$ measurement for each sample.

Summary effects of welding with PWF are given in Table 4.

Table 4. Alloying element content in the weld metal

Parameter	Welding with PWF		
	min, %	max, %	Influence, %
C	0.06	0.11	45.5
Si	0.016	0.022	27.3
Mn	0.11	0.25	56
Ni	0.8	1.35	40.7
	min, cm³/100 g	max, cm³/100 g	
$[H]_{dif.}$	22.17	35.4	37.4

CONCLUSIONS

1. Comparative analysis of the methods of implementation of pulsed mode of arc burning, namely pulsed-arc welding (PAW) due to the change of external volt-ampere characteristic (VAC) and pulsed welding wire feed (PWF), and of their parameters during flux-cored wire non-stationary arc welding in an aqueous environment was performed. It was found that at PWF, it is possible to accurately determine the required value and duration of the pause and pulse current; welding with PWF allows the wire feed rate and duration to be established in the pause and pulse phase. In this case, the pause current depends on the wire feed rate. A smooth change of current and voltage parameters is observed due to inertia when switching between the pause and pulse phases. For the welding variant with a broken VAC, the VAC falling portion limits the pause current. This provides a better-controlled process in combination with PWF. In this case, unlike the simple process with PWF, it is possible to determine the pause current more accurately. And, unlike pulsed self-regulation, there is the possibility of more precise control of the process frequency due to PWF.

2. The pulsed process parameters influence on the weld metal dimensions and shape was assessed. The welding modes remained fixed: welding speed of 9 m/h, average welding current of 185 A. The rate of welding wire feed in the pulse (PWF) and pulse current (PAW) were the correction parameters to set the welding mode. Analysis of the measurement results of the weld geometrical dimensions showed that in welding with PWF at the same current and voltage, pulses allow much more significant influence on weld penetration depth and convexity — 63 and 55 %, respectively. The influence of PWF parameters on weld width is small. Compared to other devices, the influence on penetration depth is greater at the application of a pulsed power source, but it is not higher than 29 %. The influence on the width and convexity is 2.5 times smaller, equal to 13.5 and 11.7 %, respectively. Thus, welding with PFW widens the range of influence on weld dimensions at the change of process parameters.

3. It was established that the use of PWF, compared to welding with constant wire feed, allows for a significant degree of control over the deposited metal composition, with a range of up to 56 %. Modes with a frequency of 50 to 60 Hz and a relative pulse duration of 5 to 6 units correspond to a more significant transition of alloying elements.

4. The effectiveness of the pulsed process for weld metal degassing was thoroughly investigated. The study of the hydrogenation mechanism revealed that the majority of hydrogen (60–70 %) enters the weld pool with the electrode metal drop, which is saturated by it from the vapour-gas bubble atmosphere. Pulsed impact significantly reduces the time of existence of liquid metal at the drop stage, leading to a substantial reduction in the amount of hydrogen in the weld metal. The process with pulsed feed of flux-cored wire was found to be particularly effective, with the total hydrogen content decreasing by an average of 37 %. The influence of gas saturation for oxygen and nitrogen is minimal, not exceeding 5 %. This finding underscores the practical implications of the effectiveness of the pulsed process in reducing the amount of hydrogen in the weld metal.

REFERENCES

1. Ghosh, P.K. (2017) Concept of pulse current gas metal arc welding process. In: *Pulse Current Gas Metal Arc Welding: Characteristics, Control and Applications*. Springer Nature Singapore Pte Ltd., 31–45.
2. Kamal, Pal, Surjya, K. Pal (2011) Effect of pulse parameters on weld quality in pulsed gas metal arc welding: A Review. *J. of Materials Eng. and Performance*, 20(**6**), 918–931. DOI: https://doi.org/10.1007/s11665-010-9717-y
3. Correa, C.A., Mastelari, N., Moreno, J.R.S. (2014) Effect of welding parameters in flux core arc welding (FCAW) with conventional and pulsed current in the efficiency and fusion rate of melting coating. *Scientific Research and Essays*, 9(**23**), 976–983. DOI: https://doi.org/10.5897/SRE2014.6064
4. Hu, J., Tsai, H.L. (2006) Effects of current on droplet generation and arc plasma in gas metal arc welding. *J. of Applied Physics*, 100(**5**), 1–12. DOI: https://doi.org/10.1063/1.233726
5. Reisgen, U., Purrio, M., Buchholz, G., Willms, K. (2013) Possibilities of a control of the droplet detachment in pulsed gas metal arc welding. *Welding in the World*, 57(**5**), 701–706. DOI: https://doi.org/10.1007/s40194-013-0069-8
6. Zhao Yangyang, Chung Hyun (2018) Influence of power source dynamics on metal and heat transfer behaviors in pulsed gas metal arc welding. *Inter. J. of Heat and Mass Transfer*, **121**, 887–899. DOI: https://doi.org/10.1016/j.ijheatmasstransfer.2018.01.058
7. Maksimov, S., Gavrilyuk, A., Krazhanovskyi, D. (2021) Stabilization of the process of mechanized pulsed-arc welding. *Transfer of Innovative Technologies*, 4(**2**), 41–52. DOI: https://doi.org/10.32347/tit2021.42.0202
8. Zeiffarth, P., Kasatkin, O.G. (2002) Calculation models for evaluation of mechanical properties of HAZ metal in welding of low-alloy steels. In: *Proc. of Inter. Conf. on Mathematical Modeling and Information Technologies in Welding and Related Processes, Kyiv*, 103–106 [in Russian]. https://patonpublishinghouse.com/proceedings/mmw2002.pdf
9. Maksimov, S.Y., Shlapak, L.S., Gavrilyuk, A.A. et al. (2019) Regularities of welding by the process of mechanized pulse-arc welding to ensure its stability. *Exploration and Development of Oil and Gas Deposits*, 73(**4**), 65–76. DOI: https://doi.org/10.31471/1993-9973-2019-4(73)-65-76.
10. Silva, R.H.G., Galeazzi, D., Rocha, P.C.J. et al. (2021) Multiple output analysis for advanced waveform and controlled short-circuit MIG-MAG variants. *Welding in the World*, **65**, 2267–2282. DOI: https://doi.org/10.1007/s40194-021-01176-2
11. Ibarra, S., Grubbs, C.E., Liu, S. (1994) State-of-the-art and practice of underwater wet welding of steel. In: *Inter. Workshop on Underwater Welding of Marine Structures*. New Orleans, 49–112.
12. Lucas, W., Cooper, M.A. (1997) Underwater FCA wet welding. In: *Underwater Wet Welding and Cutting. Inter. Seminar and Workshop TWI North Middlesbrough, UK, 17–18 April 1997*, 105–113. Woodhead Publ. ltd.
13. Shen Chao, Li Zhizun, Ma Yunhe, Sun Liming (2019) Research and application of underwater wet welding technology. In: *Proc. of IOP Conf. Series on Materials Sci. and Eng*., 562(**1**). DOI: https://doi.org/10.1088/1757-899X/562/1/012161
14. Karpov, V.M., Murzin, V.V., Khabuzov, V.A., Vladimirov, A.V. (2014) Technology of digital synthesis of pulse welding of ship structures made of aluminum alloys. *Marine Intelligent Technologies*, 2(**24**), 94–100.
15. Vladimirov, A.V. (2015) Welding source for "wet" underwater welding with flux-cored wire. *Materials Sci*., 1(**81**), 259–262.
16. Paton, B.E., Lebedev, V.A., Pichak, V.H. et al. (2001) Analysis of technical and technological possibilities of the pulsed feed of electrode wire in arc welding and surfacing processes. *Welding Inter*., 16(**7**), 575–581. DOI: https://doi.org/10.1080/09507110209549580
17. Lebedev, V., Reisgen, U., Lendiel, I. (2016) Study of technological opportunities of GMA welding and surfacing with pulse electrode wire feed. *Welding in the World*, 60(**3**), 525–533. DOI: https://doi.org/10.1007/s40194-016-0321-0
18. Jorge, V.L., Santos, C.H.A., Scotti, F.M. et al (2018) Development and evaluation of wire feeding pulsing techniques for arc welding. *Soldagem & Inspecao*, 23(**3**), 326–339. DOI: https://doi.org/10.1590/0104-9224/si2303.03
19. Lebedev, V., Rymsha, V., Lendel, I. (2014) BLDC electric-drive in the mechanism of pulse feed of electrode wire. *Electrotechnic and Computer Systems*, 16(**92**), 35–39.

ORCID

S. Maksymov: 0000-0002-5788-0753,
D. Krazhanovskyi: 0000-0001-7292-7188

CONFLICT OF INTEREST

The Authors declare no conflict of interest

CORRESPONDING AUTHOR

S. Maksymov
E.O. Paton Electric Welding Institute of the NASU
11 Kazymyr Malevych Str., 03150, Kyiv, Ukraine.
E-mail: maksimov@paton.kiev.ua

SUGGESTED CITATION

S. Maksymov, D. Krazhanovskyi (2025)
Effectiveness of application of pulsed mode of arc burning in wet underwater welding.
The Paton Welding J., **7**, 3–10.
DOI: https://doi.org/10.37434/tpwj2025.07.01

JOURNAL HOME PAGE

https://patonpublishinghouse.com/eng/journals/tpwj

Received: 12.02.2025
Received in revised form: 17.04.2025
Accepted: 04.07.2025

DOI: https://doi.org/10.37434/tpwj2025.07.02

HIGH TEMPERATURE TITANIUM ALLOY TIG WELDING USING ACTIVATING FLUXES

S.V. Akhonin, V.Yu. Bilous, R.V. Selin, S.L. Schwab, I.K. Petrychenko, L.M. Radchenko

E.O. Paton Electric Welding Institute of the NASU
11 Kazymyr Malevych Str., 03150, Kyiv, Ukraine

ABSTRACT

High temperature titanium alloys are materials that can withstand high temperatures and maintain their mechanical properties under extreme heat load. The use of high temperature titanium alloys helps to increase the efficiency of engines and reduce the weight of structures, which in turn leads to reduced fuel consumption and increased overall equipment productivity. Welding of high temperature titanium alloys is complicated due to the presence of such impurities as aluminum, vanadium, molybdenum and other elements in their composition that increase their high temperature properties. Silicon is one of the elements that effectively increase the high temperature properties of titanium alloys. However, a significant defect of alloys with silicon is cold cracks in the welds, which occur at temperatures below 700 °C, when the material passes from a ductile to a brittle state. The brittleness of the weld in as-welded state, in turn, is determined by its structure and, with an increase in welding stresses during the cooling, it leads to the appearance of defects such as cold cracks, the source of which are microcracks, dislocations, etc. In this work, a study was conducted of the influence of the additional technological operations, such as flux welding and preheating before welding, on the structure and mechanical properties of welded joints of a high temperature titanium alloy of the Ti–6.5Al–5.3Zr–2.2Sn–0.6Mo–0.5Nb–0.75Si system.

KEYWORDS: high temperature titanium alloy, TIG welding, preheating, welding with fluxes

INTRODUCTION

High temperature titanium alloys are materials capable of withstanding high temperatures and preserving their mechanical properties under extreme heat load. These alloys have high strength, corrosion resistance and low density, making them ideal for application in the aerospace and automotive industry, as well as in the energy sector [1, 2].

Application of high temperature titanium alloys promotes an increase in the efficiency of engine operation and reduction in structure weight that, in its turn, leads to reduction in fuel consumption and increase in the overall productivity of the equipment. Despite their high cost and complex treatment, the advantages, which they offer, justify their application in critically important components, where the reliability and durability are the key factors [3].

Titanium alloys usually have impurities of aluminium, vanadium, molybdenum and other elements, which enhance their heat-resistance properties. They are used in production of the components of turbines, aircraft engines, car parts and in many other high-tech industries. Silicon (Si) is one of the elements, effectively enhancing the heat-resistance properties of the titanium alloys [4]. Silicon addition to the alloy promotes a strengthening of the material structure and increase of its stability at temperature gradients. This is achieved due to silicon forming solid solutions and dispersed particles in the titanium matrix, which prevents the movement of dislocations and reduces the deformation rate [5].

When producing the welded joints of the high temperature titanium alloys, containing silicon as the alloying element, their significant defect is cold cracks in the welds, initiating at temperatures below 700 °C, when the material goes from the ductile into the brittle state [6]. Brittleness of the weld in as-welded state, in its turn, is determined by its structure and at increase of the welding stresses during cooling it leads to initiation of defects of the type of cold cracks, the source of which are microcracks, dislocations, etc. Therefore, welding of such alloys requires application of additional technological operations such as local heat treatment and preheating [7, 8].

More over, these titanium alloys, compared to the conventional alloys, are more sensitive to such interstitial impurities as oxygen, nitrogen and carbon. Owing to the fact that silicon in the high temperature alloys is no longer an impurity, but an alloying element, increased silicon content may lead to development of chemical and physical heterogeneity in the cast metal and the HAZ, which may result in formation of brittle interlayers. The interstitial impurities lower the ductility and impact toughness of the weld metal, increase the brittle fracture susceptibility, and sensitivity to stress raisers. More over, in the high temperature alloys oxygen, nitrogen and carbon lower the thermal stability, which is associated with the fact that the above elements accelerate the processes of

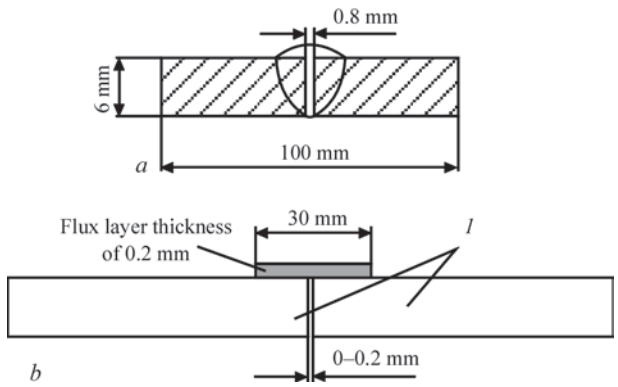

Figure 1. Schematic of sample assembly for welding: *a* — TIG welding with through penetration; *b* — TIG welding over a layer of flux

metastable phase decomposition. Oxygen, nitrogen and carbon impair the adaptability-to-fabrication of the high temperature alloys, in particular their weldability. Heat treatment — annealing is used to enhance the high temperature resistance of the titanium alloys [9, 10].

THE OBJECTIVE

of this work is investigation of the structure and properties of the high temperature titanium alloy after TIG welding, as well as determination of the influence of preheating on the structure and properties of welded joints.

MATERIALS AND PROCEDURE OF INVESTIGATION

Samples of the size of 200×100×6 mm were welded (Figure 1, *a*). Welding was conducted from one side. Welding modes were selected under the condition of ensuring complete penetration of the joints of 6 mm Ti–6.5Al–5.3Zr–2.2Sn–0.6Mo–0.5Nb–0.75Si alloy.

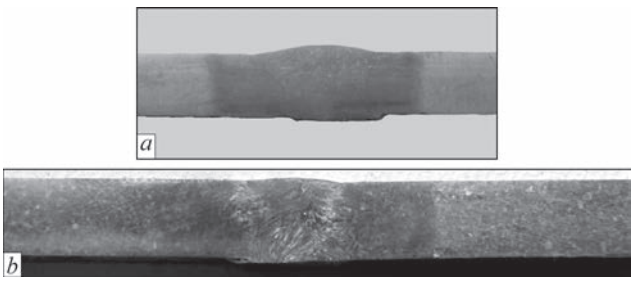

Figure 3. Transverse macrosection of a welded joint of high temperature titanium alloy Ti–6.5Al–5.3Zr–2.2Sn–0.6Mo–0.5Nb–0.75Si produced by: *a* — TIG welding; *b* — A-TIG welding

In addition to the standard argon-arc welding (TIG), also argon-arc welding over a layer of flux (A-TIG) with preheating was performed. This kind of welding is an effective means of influencing the penetrability of the arc, in which halogenides of alkali and alkali-earth metals are added to the arc atmosphere, leading to a change in the mode of weld metal penetration and weld formation due to arc constriction [11]. The flux promotes an increase in the penetration depth and change in the penetration shape. Owing to an increase in the arc penetrability, TIG welding with flux deposited on the surface of the edges being welded (Figure 1, *b*), allows welding in one pass the joints of titanium alloys up to 6 mm thick without edge preparation [12, 13].

The modes of TIG welding with through-penetration and over a layer of flux of the high temperature titanium alloy Ti–6.5Al–5.3Zr–2.2Sn–0.6Mo–0.5Nb–0.75Si from one side are given in Table 1.

Sample preparation for automatic TIG welding of titanium with through penetration is shown in Figure 1.

Before welding the 6 mm metal plates were subjected to vacuum annealing at the temperature of

Table 1. Mode of TIG welding with through-penetration of high temperature titanium alloy Ti–6.5Al–5.3Zr–2.2Sn–0.6Mo–0.5 Nb–0.75Si from one side

Mode No.	Welding current, I_w	Arc voltage, U_a, V	Welding speed, V_w, m/h	Arc length, L_a, mm	Preheating temperature, T_{pr}, °C
1	330	12	8	2	–
2 (over flux)	400	12	16	1	200
3 (over flux)	330	12	16	1	400

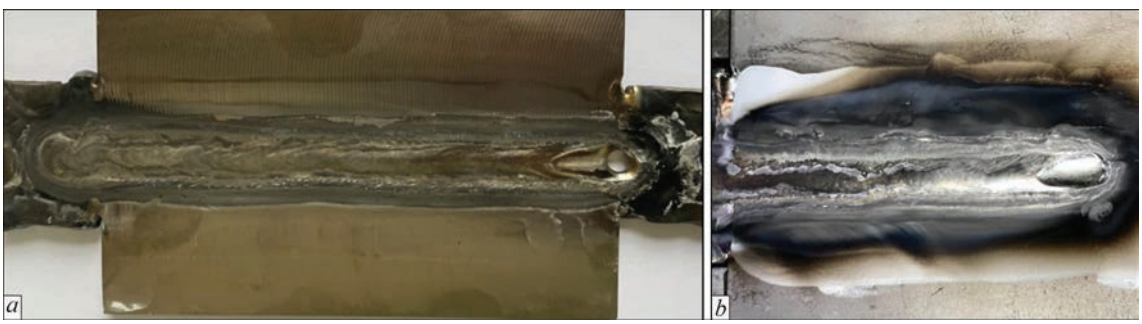

Figure 2. Example of an A-TIG welded joint of high temperature titanium alloy Ti–6.5Al–5.3Zr–2.2Sn–0.6Mo–0.5Nb–0.75Si: *a* — face side of the weld; *b* — sample in the furnace after welding

900 °C with cooling in the furnace. The appearance of welded joints of the produced weld is given in Figure 2. The microstructure of the welded joints is shown in Figure 3.

RESULTS AND THEIR DISCUSSION

MICROSTRUCTURAL STUDIES

Microstructure of the base metal (BM) of a welded joint made in mode No.1 (see Table 1), is shown in Figure 4. The base metal consists of equiaxed primary β-grains of 150–900 μm size with an intermittent interlayer of the α-phase along the grain boundaries. The intragranular structure is formed by colonies of α-plates of different size. The thickness of α-phase plates is equal to 1–3 μm.

The weld metal of the high temperature titanium alloy Ti–6.5Al–5.3Zr–2.2Sn–0.6Mo–0.5Nb–0.75Si consists of equiaxed primary β-grains elongated in the direction of the heat evolution, larger in the weld upper part (Figure 5, *a*, *b*) and finer in the middle and root parts. The equiaxed grains form predominantly along the weld axis. An interlayer of the α-phase is observed here and there along the grain boundaries. During rapid cooling of the weld metal from the temperatures in the β-region the β→α′ martensitic transformation occurs with formation of colonies of plates of 5–50 μm size. The fusion zone in the near-weld zone consists of equiaxed grains of 100–600 μm size. In the HAZ adjacent to the weld, where the metal was heated in welding to temperatures in the β-region, an α-phase with a lamellar morphology could form after cooling at a high rate (Figure 5, *c*, *d*). Plate thickness was 1–2 μm. In the HAZ region adjacent to the base metal, heated to temperatures in the (α+β)-region during welding, the α-, β- and α′-phase differing from the α-phase by another level of alloying, can be present (Figure 5, *e*, *f*).

The metal of the welded joint produced by A-TIG welding with application of preheating at 200 °C (mode No. 2), consists of equiaxed grains of 200–400 μm size with a lamellar intragranular structure (Figure 6, *a*, *b*), the width of α-plates being 1–4 μm. The metal microstructure in the fusion zone consists

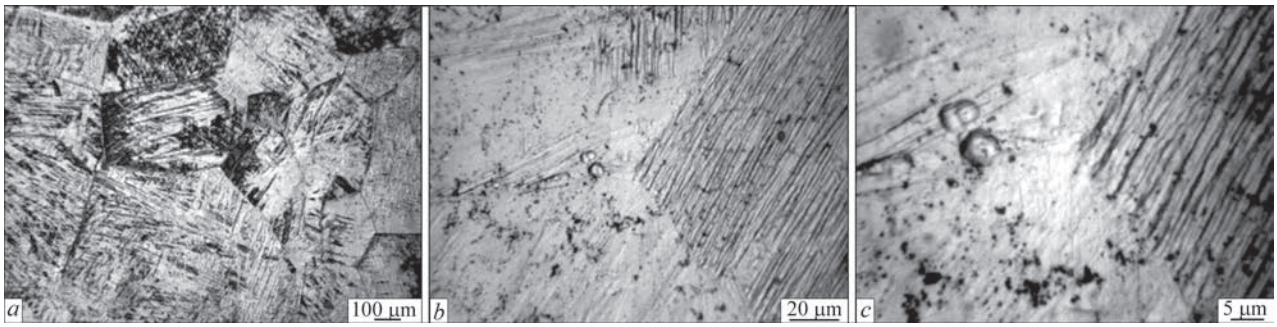

Figure 4. Microstructure of the base metal in a joint of high temperature titanium alloy Ti–6.5Al–5.3Zr–2.2Sn–0.6Mo–0.5Nb–0.75Si

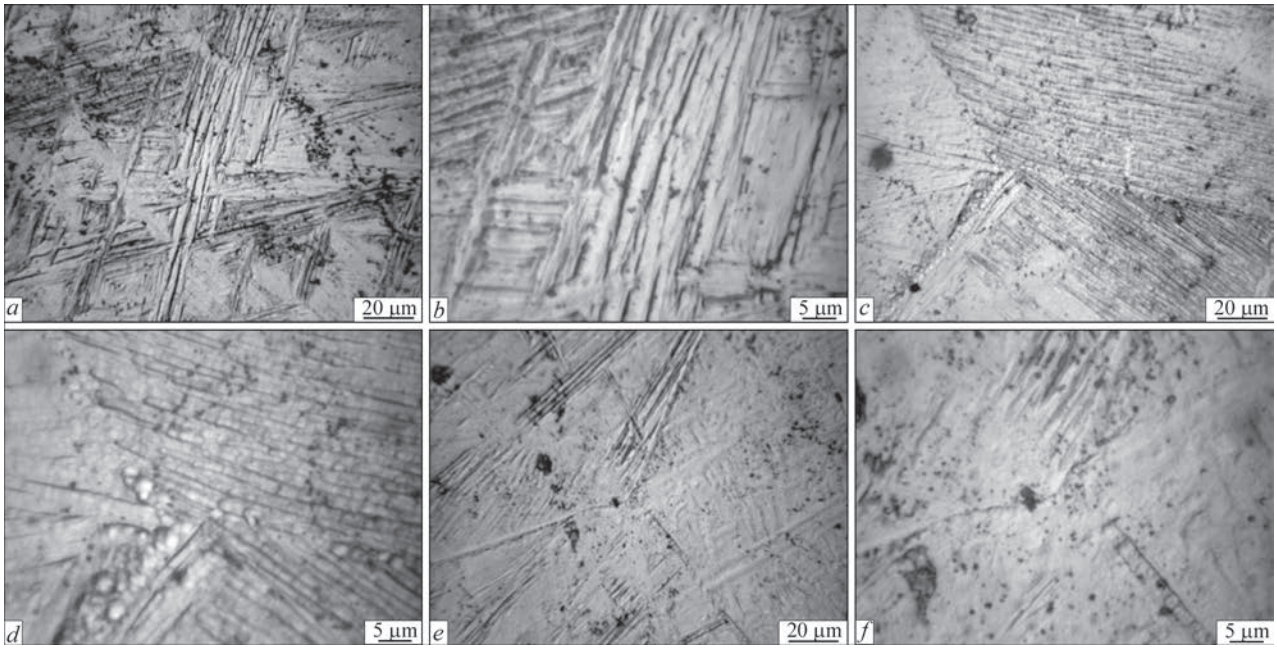

Figure 5. Microstructure of a joint of high temperature titanium alloy Ti–6.5Al–5.3Zr–2.2Sn–0.6Mo–0.5Nb–0.75Si welded in mode No. 1: *a*, *b* — weld metal; *c*, *d* — HAZ adjacent to the weld; *d*, *f* — HAZ adjacent to the base metal

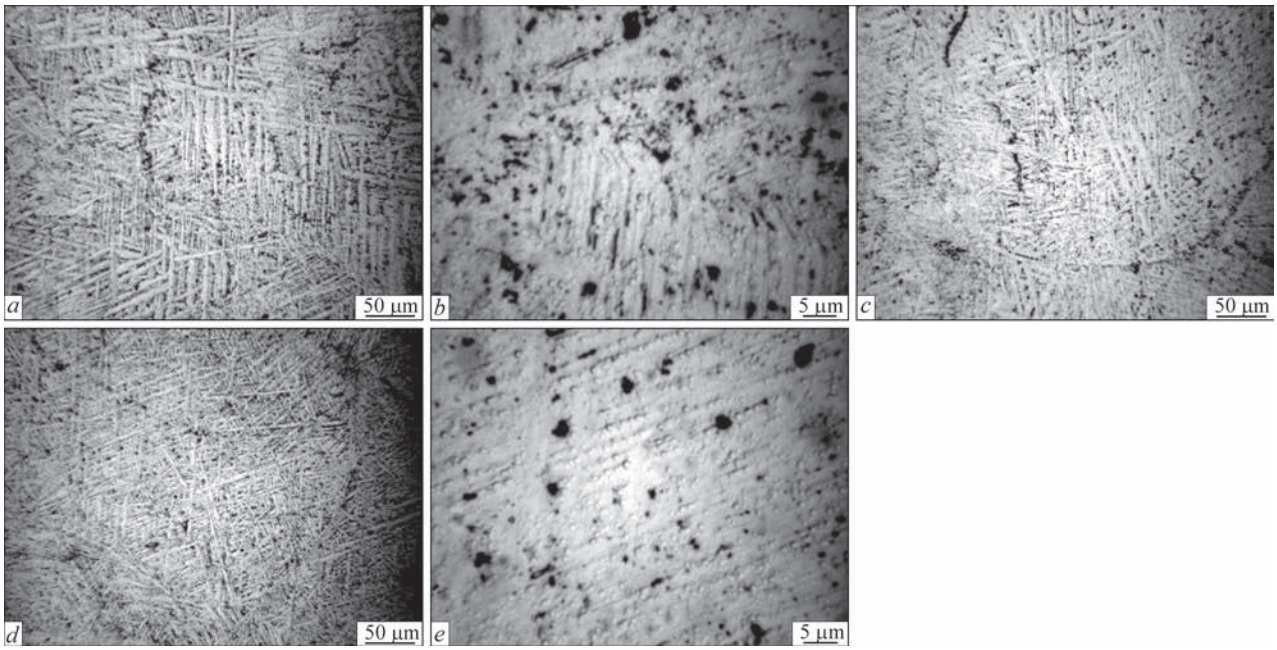

Figure 6. Microstructure of a joint of high temperature titanium alloy Ti–6.5Al–5.3Zr–2.2Sn–0.6Mo–0.5Nb–0.75Si welded in mode No. 2: *a*, *b* — weld metal; *c* — HAZ adjacent to the weld; *d*, *f* — HAZ adjacent to the base metal

of equiaxed grains of 100–600 μm size. Dispersed particles in the form of isolated precipitates and their clusters can be also present in the metal structure, their size being less that 1 μm (Figure 6, *c*). In the HAZ region adjacent to the base metal, which was heated to the temperatures in the (α+β)-region during welding, the α-, β- and α′-phase differing from the α-phase by another level of alloying, are present (Figure 6, *d*, *e*). The physical and mechanical properties of the α′-phase in pseudo-α alloys, however, are close to those for the α-phase, so that the presence of α′-phase in the welded joint will not impair its physical and mechanical properties. A lamellar structure is observed in the HAZ metal, similar to the weld metal, as well as the above-described dispersed particles.

The weld metal of the joint produced in mode No. 3, consists of grains of 100–500 μm dimensions (Figure 7, *a*, *b*) with a lamellar intragranular α-phase. Dispersed precipitates of two kinds are observed between the plates in the figures: light- and dark-coloured. The nature and arrangement of the dispersed particles are similar to those in the welded joint made in mode No. 2. In the fusion zone fine polyhedral equiaxed grains of 50–150 μm size are located between

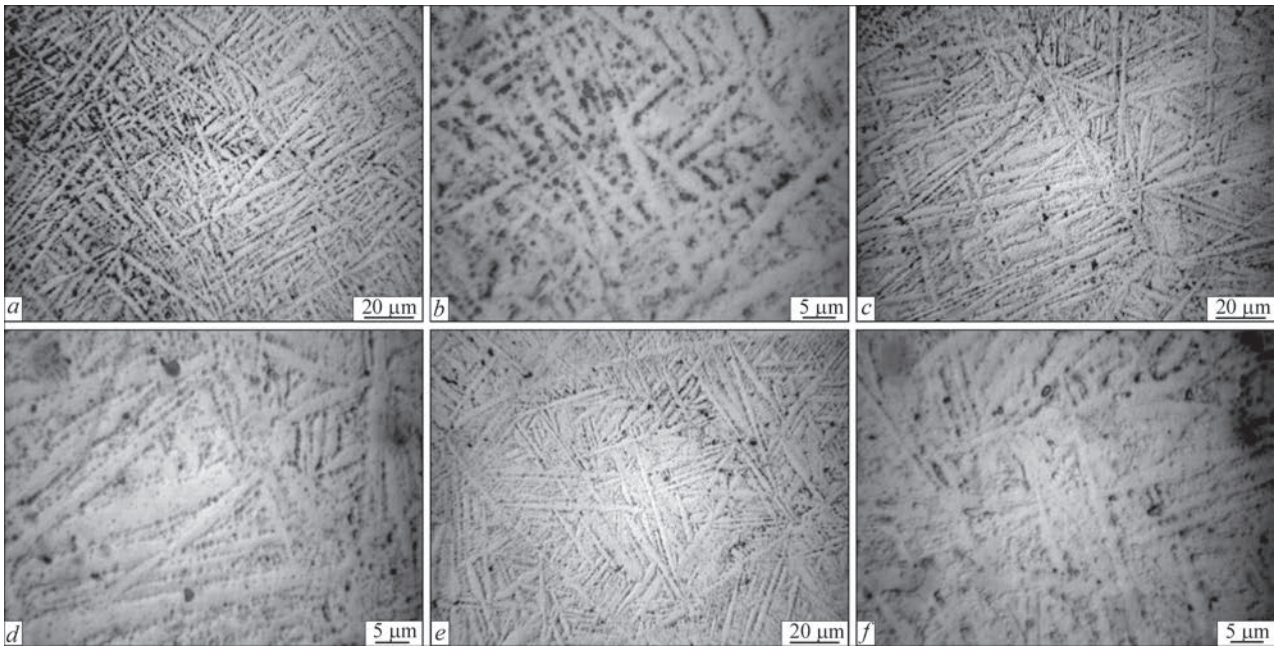

Figure 7. Microstructure of a joint of high temperature titanium alloy Ti–6.5Al–5.3Zr–2.2Sn–0.6Mo–0.5Nb–0.75Si welded in mode No. 3: *a*, *b* — weld metal; *c*, *d* — HAZ adjacent to the weld; *d*, *f* — HAZ adjacent to the base metal

Table 2. Mechanical properties of welded joints of high temperature titanium alloy Ti–6.5Al–5.3Zr–2.2Sn–0.6Mo–0.5Nb–0.75Si

Mode No.	T_{pr}, °C	σ_t < MPa	$\sigma_{0.2}$, MPa	δ_s, %	*KCV*, J/cm^2
As-rolled base metal	–	1044	975	4.5	12.7
TIG, mode No.1	–	969	80	11.2	8.9
A-TIG, mode No. 2	200	1007	929	–	9.7
A-TIG, mode No. 3	400	1091	988	6.8	9.0

the weld metal and HAZ grains elongated in the direction of heat removal (Figure 7, *c*, *d*), the width of the layer of such grains being 300–400 μm. Dispersed precipitates and α-, β- and α′-phases are present in the HAZ metal adjacent to the base metal which was heated in welding to temperatures in the (α+β)-region (Figure 7, *e*, *f*). In all the HAZ regions dispersed particles of the same size as those in other welded joint regions are present, being located along the boundaries of the grains and plates. Among such particles the most probable is the titanium silicide, as silicon concentration in the alloy significantly exceeds the limit of its solubility in α-titanium. Local presence of dispersed particles of the α_2- and β-phases in the HAZ metal is not excluded.

Thus, the conducted studies allowed us to conclude that the microstructure in different regions of the welded joints of high temperature titanium pseudo-α alloy is identical and similar with different methods and modes of welding. It can be assumed that the phase composition of the metal in different regions of the welded joints will not have any sharp differences. A change in the welding energy input makes a greater contribution to the joint structure. At application of the basic technological process — TIG with through penetration — coarsened packs of the size in the

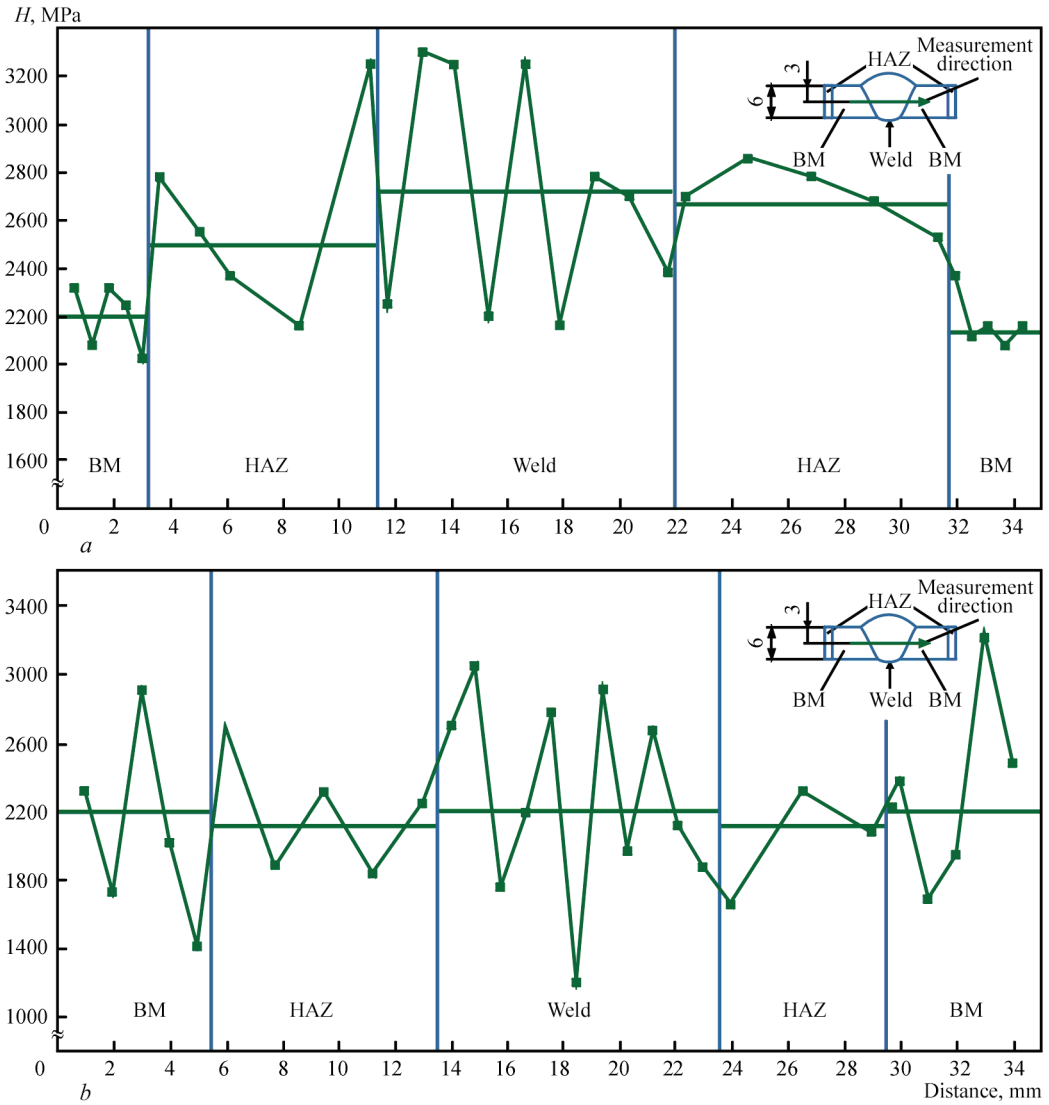

Figure 8. Microhardness distribution in the welded joint of high temperature titanium alloy Ti–6.5Al–5.3Zr–2.2Sn–0.6Mo–0.5Nb–0.75Si: *a* — welding mode No. 1; *b* — mode No. 3

range of 10–30 μm (by the size of the largest plates) are formed. At lowering of the specific power during application of A-TIG welding a reduction in the pack dimensions and an increase in the microstructure homogeneity are observed, which should have a positive effect on the welded joint mechanical properties.

INVESTIGATION OF MECHANICAL PROPERTIES

Investigation of the welded joint mechanical properties showed that the joints produced by TIG welding with through penetration without preheating application in mode no.1 (Table 2) have the lowest strength values in as-welded condition (Table 2), equal to 969 MPa or 93 % of that of as-rolled base metal. Welded joints produced by TIG welding with application of preheating to 400 °C (mode No.3) have the highest strength values equal to 1091 MPa, which is at the level of the base metal strength. Welded joints made by TIG welding with application of preheating to 200 °C (mode No. 2) have medium strength values at the level of 1007 MPa or 96 % of base metal strength.

Distribution of metal microhardness in welded joints of high temperature titanium alloy Ti–6.5Al–5.3Zr–2.5Sn–0.6Mo–0.5–Nb–0.75Si, produced by TIG welding with preheating to 400 °C in as-welded state, showed that the microhardness level in the base metal remained unchanged, while in the metal of the weld and the HAZ the microhardness level decreased, has leveled out and is in the range of 1800–2800 MPa (Figure 8).

Thus, in A-TIG welding with reduced specific power a fine highly homogeneous structure is formed. Preheating to 400 °C leads to a certain coarsening of the structure; coarsened packs of the size in the range of 10–30 μm (by the size of the largest plates) form in the weld metal, and its application can be justified only by technological reasons, namely lowering the risk of cracking. With lowering of the specific power during application of A-TIG welding a reduction in the pack size is observed and an increase in the microstructure homogeneity, which will have a positive effect on the welded joint mechanical properties. That is why it is rational to perform TIG welding of the high temperature titanium pseudo-α alloy of Ti–6.5Al–5.3Zr–2.2Sn–0.6Mo–0.5Nb–0.75Si system with application of fluxes and preheating to the temperature of 400 °C, which provide the highest values of strength in as-welded state at the level of 1091 MPa.

CONCLUSIONS

1. The influence of preheating in TIG welding on the properties of welded joints of the high temperature titanium alloy Ti–6.5Al–5.3zr–2.2Sn–0.6Mo–0.5Nb–0.75Si was studied, and it was determined that application of preheating of the joints to 400 °C in A-TIG welding ensures formation in the welded joint of structures of α-phase plates 1–4 μm thick and dispersed particles of the α_2- and β-phase of average size of up to 1 μm.

2. Investigation of the mechanical properties of welded joints of the high temperature titanium alloy Ti–6.5Al–5.3Zr–2.2Sn–0.6Mo–0.5Nb–0.75Si showed that TIG welded joints produced with application of preheating to 400 °C have the highest strength values, which are equal to 1091 MPa for alloy Ti–6.5 Al–5.3Zr–2.2Sn–0.6Mo–0.5Nb–0.75Si and are at the level of 0.95–1.05 of base metal strength.

3. Determination of microhardness distribution in the TIG welded joint of the high temperature titanium alloy Ti–6.5Al–5.3Zr–2.2Sn–0.6Mo–0.5Nb–0.75Si allowed us to establish that application of preheating to 400 °C in TIG welding enables lowering the average microhardness level in the weld metal and the HAZ from 2700 to 2300 MPa, which corresponds to base metal microhardness.

4. A technological process of A-TIG welding of the high temperature titanium alloy Ti–6.5 Al–5.3Zr–2.2Sn–0.6Mo–0.5Nb–0.75Si was proposed, which envisages welding with energy input of 700–800 kJ/m over a layer of ANT25 flux and welded joint preheating to the temperature of 400 °C, which provides formation of a fine highly homogeneous microstructure in the joints and the strength values of as-welded joints at the level of not less than 0.95 of base metal strength.

REFERENCES

1. Gogia, A.K. (2005) High temperature titanium alloys. *Defence Science J.*, 55(**2**), 149–173.
2. Eylon, D.S.P.J., Fujishiro, S., Postans, P.J., Froes, F.H. (1984) High temperature titanium alloys — A review. *JOM*, 36(**11**), 55–62.
3. Tabie, V.M., Li, C., Saifu, W., Li, J., Xu, X. (2020) Mechanical properties of near alpha titanium alloys for high temperature applications — A review. *Aircraft Engineering and Aerospace Technology*, 92(**4**), 521–540. DOI: https://doi.org/10.1108/AEAT-04-2019-0086
4. Akhonin., S.V., Bilous, V.Yu., Selin, R.V. et al. (2022) Argon-arc welding of heat-resistant titanium alloy doped with silicon. *Avtomatychne Zvaryuvannya,* **5**, 33–39. DOI: https://doi.org/10.37434/as2022.05.05
5. Zhao, E., Sun, S., Zhang, Y. (2021) Recent advances in silicon containing high temperature titanium alloys. *J. of Materials Research and Technology*, **14**, 3029–3042. DOI: https://doi.org/10.1016/j.jmrt.2021.08.117
6. Selin, R.V., Bilous, V.Yu., Rukhanskyi, S.B. et al. (2023) Influence of preheating on thermal cycle of argon-arc welding of heat-resistant titanium alloy of Ti–Al–Zr–Sn–Mo–Nb–Si system. *Avtomatychne Zvaryuvannya,* **12**, 18–23. DOI: https://doi.org/10.37434/as2023.12.03
7. Akhonin, S.V., Belous, V.Y., Selin, R.V., Schwab, S.L. (2023) Effect of TIG-welding on the structure and mechanical properties of low-cost titanium alloy Ti–2.8 Al–5.1 Mo–4.9 Fe

welded joints. *Mat. Sci. Forum*, **1095**, 105–110. DOI: https://doi.org/10.4028/p-2njAz3
8. Akhonin, S.V., Belous, V.Y., Selin, R.V. (2022) Effect of preheating and post-weld local heat treatment on the microstructure and mechanical properties of low-cost β-titanium alloy welding joints, obtained by EBW. *Defect and Diffusion Forum*, **416**, 87–92. DOI: https://doi.org/10.4028/ p-o8uehr
9. Prilutsky, V.P., Akhonin, S.V. (2014) TIG welding of titanium alloys using fluxes. *Welding in the World*, **58**, 245–251. DOI: https://doi.org/10.1007/s40194-013-0096-5
10. Sun, Z., Pan, D. (2004) Welding of titanium alloys with activating flux. *Sci. and Technol. of Welding and Joining*, 9(**4**), 337–344. DOI: https://doi. org/10.1179/136217104225021571
11. Zamkov, V.N., Prilutsky, V.P., Gurevich, S.M. (1977) Influence of flux composition on the non-consumable electrode welding of titanium. *Avtomatich. Svarka,* **4**, 22–26.
12. Gurevich, S.M., Zamkov, V.N., Blashchuk, V.E. et al. (1986) *Metallurgy and technology of welding of titanium and its alloys: Monograph.* Kyiv, Naukova Dumka.
13. Gurevich, S.M. (1961) Fluxes for automatic welding of titanium alloys. *Aviats. Promyshlennost,* **5**, 55–59.

ORCID
S.V. Akhonin: 0000-0002-7746-2946,
V.Yu. Bilous: 0000-0002-0082-8030,
R.V. Selin: 0000-0002-2990-1131,
S.L. Schwab: 0000-0002-4627-9786,
I.K. Petrychenko: 0000-0002-0476-3983,
L.M. Radchenko: 0009-0008-1097-7137

CONFLICT OF INTEREST
The Authors declare no conflict of interest

CORRESPONDING AUTHOR
R.V. Selin
E.O. Paton Electric Welding Institute of the NASU
11 Kazymyr Malevych Str., 03150, Kyiv, Ukraine.
E-mail: selinrv@gmail.com

SUGGESTED CITATION
S.V. Akhonin, V.Yu. Bilous, R.V. Selin, S.L. Schwab, I.K. Petrychenko, L.M. Radchenko (2025)
High temperature titanium alloy TIG welding using activating fluxes. *The Paton Welding J.*, **7**, 11–17.
DOI: https://doi.org/10.37434/tpwj2025.07.02

JOURNAL HOME PAGE
https://patonpublishinghouse.com/eng/journals/tpwj

Received: 19.12.2024
Received in revised form: 04.03.2025
Accepted: 04.07.2025

DOI: https://doi.org/10.37434/tpwj2025.07.03

WELDING AND TECHNOLOGICAL PROPERTIES OF SPARSELY ALLOYED FLUX-CORED WIRES FOR STRENGTHENING AND REPAIR OF PARTS BY ARC SURFACING

S.Yu. Maksymov, A.A. Babinets, I.P. Lentyugov, V.V. Osin

E.O. Paton Electric Welding Institute of the NASU
11 Kazymyr Malevych Str., 03150, Kyiv, Ukraine

ABSTRACT

The results of a comparative study of the welding and technological properties of the developed sparsely alloyed flux-cored wires (FCWs) of two types: PP-Np-50Kh2MNSGF and PP-Np-20KhGS are presented. The evaluation was performed using a comprehensive procedure that includes three components: visual inspection of the surfacing process, evaluation of melting characteristics, and determination of arc process stability. A digital self-recording ANENG AN9002 multimeter was used to monitor the surfacing parameters. As a reference, the standard FCW of PP-Np-25Kh5FMS grade, developed at the E.O. Paton Electric Welding Institute of the NAS of Ukraine (PWI), was used. The experimental comparative analysis demonstrated that surfacing with the developed FCWs is characterized by high process stability, good quality of the deposited metal formation, absence of macrodefects, and satisfactory slag crust separation. Microstructural analysis of the deposited layers confirmed the absence of microdefects (pores, cracks, lacks of fusion) and revealed a distinct fusion line between the base metal and the deposited metal. The results of the comprehensive comparative analysis of the developed sparsely alloyed FCWs demonstrated that they possess similar or improved welding and technological characteristics compared to the standard reference wire. This indicates the feasibility of using the developed FCWs for arc surfacing applications. Considering the purpose of the developed FCWs, they can be effectively used to enhance the wear resistance and service life of parts in special-purpose and industrial equipment, which is particularly relevant in the context of Ukraine's post-war reconstruction and strengthening of its defence capability.

KEYWORDS: arc surfacing, flux-cored wire, deposited metal, welding and technological properties, resource saving

INTRODUCTION

In the context of Ukraine's post-war reconstruction and ensuring its defence capability, it is crucial to introduce efficient and cost-effective technologies for repair and restoration of damaged parts of military equipment and industrial machinery. Flux-cored wire (FCW) arc surfacing is one of the most promising methods that allows restoring and strengthening the surfaces of various parts due to its wide capabilities of ensuring the required composition of the deposited metal at minimal material consumption [1–7].

FCW arc surfacing has a number of significant advantages [1–7]. Firstly, this method makes it possible to form wear-resistant coatings with the required hardness, strength and corrosion resistance, which significantly extends the service life of parts. Secondly, the technology ensures high efficiency, as it allows surfacing large volumes of metal in a short time with minimal material losses. Thirdly, FCWs make it possible to obtain a stable quality of the deposited metal due to the uniform distribution of alloying elements and the ability to adjust their composition.

However, the available FCWs are often imported and/or not adapted to the specific operating conditions of special and industrial machinery parts used in Ukraine. In addition, when solving the problem of restoring a specific part, it is necessary to take into account its operating conditions, chemical composition of the material, and required properties, and, therefore, it is often necessary to develop a new FCW that will ensure the achievement of the set tasks.

The use of FCW with an optimized composition ensures effective alloying of the deposited metal, allowing the reduction in the content of scarce alloying elements without losses in mechanical properties [8–12]. This is especially important in the context of the need in shortening the raw material costs. The introduction of sparsely alloyed FCWs will promote the creation of resource-saving technologies, reduce dependence on imported materials and increase the technological autonomy of the defence and repair industries. Thus, the development of sparsely alloyed FCWs for arc surfacing is an urgent task due to the need in improving the efficiency of repair and restoration of parts, especially in the context of Ukraine's post-war reconstruction and ensuring its defence capability.

The main task in developing new FCWs is to determine their welding and technological properties, which directly affect the stability of the surfacing process, quality and service life of restored parts. Deter-

mining the optimal surfacing modes to improve the process stability and efficiency, reduction in the tendency to defect formation, and ensuring high quality of deposited metal formation are crucial in providing the reliability and efficiency of restoration of machine and machinery parts.

THE AIM

of the study is to determine and comparatively analyze the welding and technological characteristics of the developed sparsely alloyed FCWs for arc surfacing with the standard FCW reference to evaluate the possibility of using the developed experimental FCWs in strengthening and restoration of various parts for the needs of the defence industry and Ukraine's post-war reconstruction.

MATERIALS AND RESEARCH PROCEDURES

Parameters related to welding and technological properties depend on the object of study. Therefore, researchers choose or develop procedure for their determination in each specific case, depending on the set tasks. Based on the above, the evaluation of welding and technological properties was performed according to the developed comprehensive experimental procedure, which consists of three components [13].

The first component includes a visual expert evaluation of the arc surfacing process and the produced deposited metal. The controlled parameters included in the mentioned component are the arc excitation nature, the quality of the deposited metal formation, the presence of visible defects and the quality of slag crust separation (provided that submerged arc surfacing or surfacing using self-shielded FCW is applied).

The second component includes the evaluation of the melting characteristics (efficiency) of FCW, which is determined by the melting, deposit and loss factors. The higher the melt and deposition indices and the lower the loss rate, the higher the FCW deposition efficiency.

The third component includes the evaluation of the arc surfacing process stability, which was performed based on the dispersion of the actual values of arc current and voltage during their repeated record by the calculated corresponding constants of variation. The use of the constant of variation as a controlled parameter makes it possible to eliminate the influence of the scale of different samples of the obtained data.

Figure 1. Appearance of the laboratory surfacing installation: *1* — welding automatic machine A-1406; *2* — control panel; *3* — welding table with a fixed test specimen; *4* — measuring shunt; *5* — digital self-recording ANENG AN9002 multimeter

To record the mode parameters during the surfacing process, a digital self-recording ANENG AN9002 multimeter equipped with a high-speed analogue-to-digital converter was used (Figure 1).

As the base metal, plates of St.3 steel, as well as plates of special 13Kh11N2V2MF and SWEBOR ARMOR 560 (35G2KhS) steels of 12 mm thick were used. Two types of experimental FCWs were studied in the work:

- No. 1 — PP-Np-50Kh2MNSGF microalloyed with boron (0.01 %), which provides a deposited metal with high wear and impact resistance and hardness of 55–59 *HRC*. It is applied for surfacing armour plates of parts operating under conditions of mechanical wear and local high-intensity impact loads;
- No. 2 — PP-Np-20KhGS, which provides a deposited metal of low-carbon low-alloy steel with a hardness of 30–35 *HRC*. It is applied for surfacing worn parts of the propulsion system of tracked special and military vehicles.

The standard FCW of the PP-Np-25Kh5FMS grade, manufactured in accordance with the technical specifications, developed at the PWI, was used as a reference [14]. The diameter of all used FCWs was 2.4 mm, and the filling factor was 25 %. The protective medium in surfacing was AN-26P flux. The sur-

Table 1. Comparative evaluation of welding and technological properties of FCW

No.	Type of deposited metal	Arc excitation nature	Quality of deposited metal formation	Presence of defects	Quality of slag crust separation	Total number of points	Factors, %				
							Melting	Surfacing	Losses	Current variation	Voltage variation
1	50Kh2MNSGF	2	1	2	1	6	16.2	15.1	6.8	15.2	7.6
2	20KhGS	2	1	2	2	7	15.3	14.4	5.4	14.7	6.2
3	25Kh5FMS	2	1	2	1	6	16.4	15.2	7.3	17.2	8.5

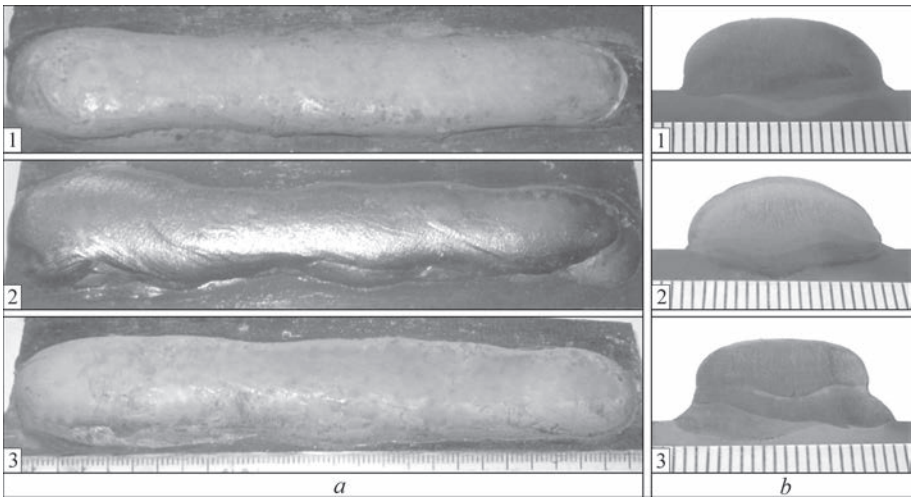

Figure 2. Appearance (*a*) and cross macrosections (*b*) of billets deposited using FCWs Nos 1–3. Wire designations are given in Table 1

facing conditions were chosen using the recommendations [4], which were the same for all specimens: voltage — 28 V, current — 300 A, deposition rate — 20 m/h.

RESEARCH RESULTS

Table 1 below summarizes the information on the evaluation of welding and technological properties. The appearance of the billets of St.3 after deposits on them performed using PP-Np-50Kh2MNSGF, PP-Np-20KhGS and PP-Np-25Kh5FMS wires, as well as their cross-sections are shown in Figure 2.

The quality of metal formation deposited on plates made of special 13Kh11N2V2MF and SWEBOR ARMOR 560 steels using PP-Np-50Kh2MNSGF wire is shown in Figure 3. Histograms of the distribution of current and voltage values on the arc, which were used to evaluate the stability of the surfacing process, are shown in Figure 4.

It was experimentally determined that the studied developed wires provide easy arc excitation, satisfactory quality of the deposited metal and the absence of defects in it (Figure 2), as well as satisfactory quality of slag crust separation.

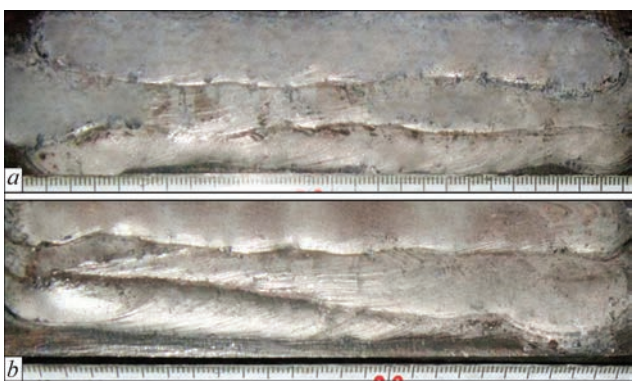

Figure 3. Quality of metal formation, deposited using PP-Np-50Kh2MNSGF wire on billets of 13Kh11N2V2MF (*a*) and SWEBOR ARMOR 560 (*b*) steel

An experimental evaluation of the possibility of using wire No. 1 (PP-Np-50Kh2MNSGF) as a material for surfacing wear-resistant layers on special steels of domestic (13Kh11N2V2MF) and imported (SWEBOR ARMOR 560) production showed the prospects of its use. According to the results of surfacing using the developed FCW on the plates of the abovementioned steels, good quality of multilayer metal formation and the absence of defects in the form of cracks, pores, lacks of fusion, etc. were noted (Figure 3).

Analyzing the obtained data (see Table 1, Figure 4), it was found that the experimental FCWs No. 1 and 2 have similar or better welding and technological characteristics compared to the reference FCW No. 3. Wire No. 1 demonstrates melting and deposit factors similar to the indices of the reference wire and exceeds the similar characteristics of wire No. 2. The loss factor is the lowest for wire No. 2, which indicates its greater efficiency in the use. Wire No. 1 has a lower loss factor than the reference wire, which also indicates its efficiency. The best surfacing stability is demonstrated by wire No. 2, which has the lowest constants of variation in current and voltage (14.7 and 6.2 %, respectively), while for wire No. 1 they amount to 15.2 and 7.6 %, which is also better compared to the reference (17.2 and 8.5 %, respectively).

The analysis of the microstructure of the specimens deposited using FCWs No. 1 and 2 showed (Figure 5) that in the specimens deposited using both types of wires, the fusion line of the deposited (top) and base (bottom) metal is quite distinct, and there are no internal microdefects in the form of pores, cracks, lacks of fusion, nonmetallic inclusions, etc.

Thus, the developed experimental FCWs No. 1 (PP-Np-50Kh2MNSGF) and No. 2 (PP-Np-20KhGS) have advantages over the reference wire or are not inferior to it in terms of the main welding and techno-

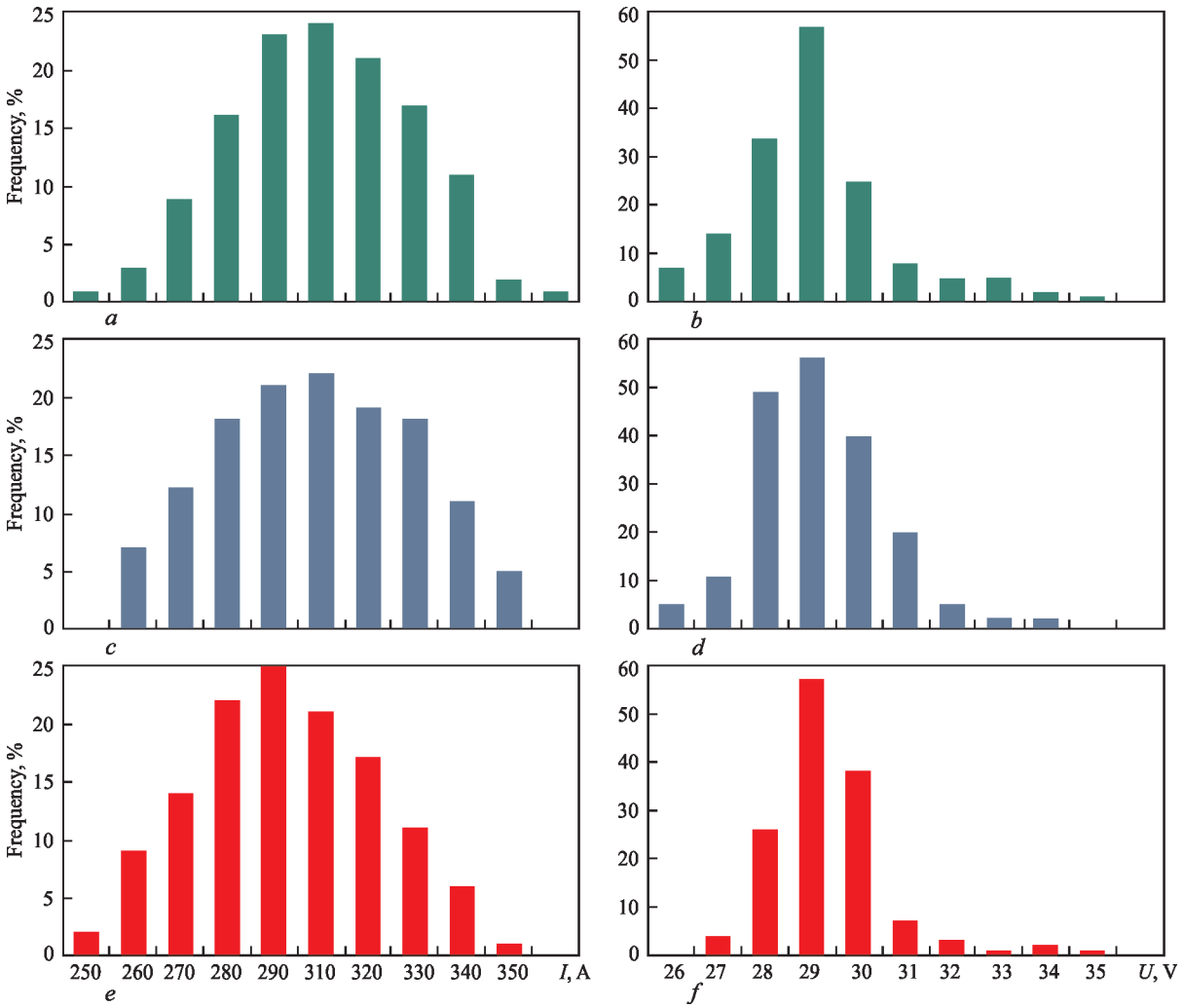

Figure 4. Histograms of current (*a*, *c*, *e*) and voltage (*b*, *d*, *f*) distribution during surfacing using FCWs: No. 1 (*a*, *b*), No. 2 (*c*, *d*) and No. 3 (*e*, *f*). Wire designations are shown in Table 1

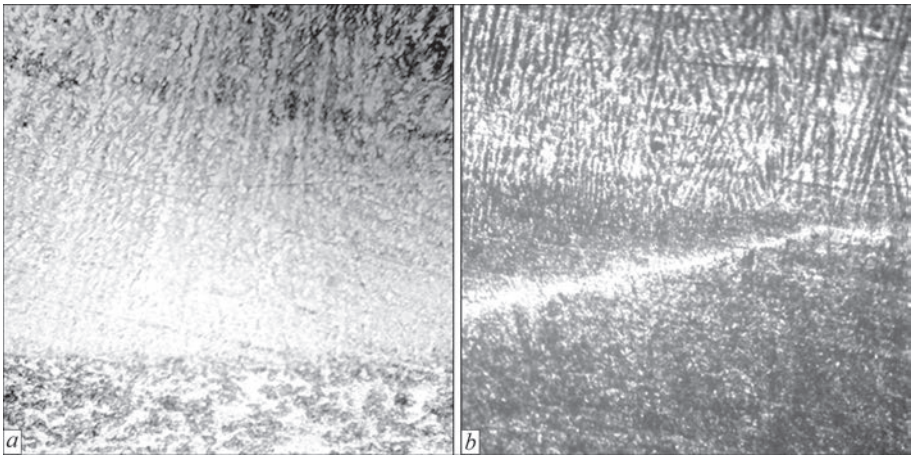

Figure 5. Microstructure of metal near the fusion line in specimens deposited using PP-Np-50Kh2MNSGF (*a*) and PP-Np-20KhGS (*b*) wires, ×240

logical characteristics, which confirms the possibility of their use for electric arc surfacing. The developed sparsely alloyed FCWs of two types, in accordance with their purpose, as described above, can be used in the manufacture or restoration of parts of special and industrial machinery to increase its service life.

CONCLUSIONS

1. According to the developed comprehensive procedure, a comparative analysis of the welding and technological characteristics of the developed sparsely alloyed flux-cored PP-Np-50Kh2MNSGF and PP-Np-20KhGS wires was carried out to deter-

mine the possibility of their wide practical application in electric arc surfacing of parts for various purposes.

2. As a result of the conducted comparative studies, it was found that the developed sparsely alloyed experimental flux-cored wires are not inferior, and in some aspects exceed the characteristics of the standard reference wire in terms of the main welding and technological parameters (ease of arc excitation, quality of deposited metal, factors of melting, deposit, losses and current/voltage constants of variation).

3. The obtained results confirm the feasibility of further development and implementation of experimental FCWs in repair and production processes for the needs of the defence industry and post-war restoration of infrastructure in Ukraine.

REFERENCES

1. Pokhodnya, I.K., Shlepakov, V.N., Maksimov, S.Yu., Ryabtsev, I.A. (2010) Research and developments of the E.O. Paton Electric Welding Institute in the field of electric arc welding and surfacing using flux-cored wire (Review). *The Paton Welding J.*, **12**, 26–33.
2. Kuskov, Yu.M. (2019) Application of flux-cored wires at surfacing, remelting and in metallurgy. *The Paton Welding J.*, **3**, 27–33. DOI: https://doi.org/10.15407/tpwj2019.03.05
3. Poznyakov, V.D., Gajvoronsky, A.A., Klapatyuk, A.V. et al. (2019) Flux-cored wire for restoration surfacing of worn surfaces of railway wheels. *The Paton Welding J.*, **7**, 36–40. DOI: https://doi.org/10.15407/tpwj2019.07.08
4. Babinets, A.A. (2023) Control of formation of metal produced by arc methods of layer-by-layer deposition of material with flux-cored wires. *The Paton Welding J.*, **11**, 35–40. DOI: https://doi.org/10.37434/tpwj2023.11.04
5. Kuskov, Yu.M., Zhdanov, V.A., Ryabtsev, I.O. et al. (2020) Methods for increasing the corrosion resistance of coatings deposited under a flux layer from high-chromium powder wires. *Mater Sci.*, **55**, 710–715. DOI: https://doi.org/10.1007/s11003-020-00362-9
6. Szymura, M., Czupryński, A., Ochodek, V. (2024) Development of a mathematical model of the self-shielded flux-cored arc surfacing process for the determination of deposition rate. *Materials*, 17(**22**), 5616. DOI: https://doi.org/10.3390/ma17225616
7. Shlepakov, V.N. (2014) Physical-metallurgical and welding-technological properties of gas-shielded flux-cored wires for welding of structural steels. *The Paton Welding J.*, **6–7**, 53–56. DOI: https://doi.org/10.15407/tpwj2014.06.10
8. Golovko, V., Kotelchuk, O., Naumeiko, S., Golyakevich, A.A. (2022) Development of self-shielded flux-cored wires for arc welding of low-alloy steels. *Defect and Diffusion Forum*, **416**, 103–114. DOI: https://doi.org/10.4028/p-58v9g5
9. Trembach, B.O., Silchenko, Yu.A., Sukov, M.G. et al. (2024) Development of a model of transition element factor of alloying elements of self-shielding flux-cored powder wire and optimization of its core filler composition. *Mater Sci.*, **59**, 733–740. DOI: https://doi.org/10.1007/s11003-024-00834-2
10. Stupnyts'kyi, T.R., Student, M.M., Pokhmurs'ka, H.V., Hvozdets'kyi, V.M. (2016) Optimization of the chromium content of powder wires of the Fe–Cr–C and Fe–Cr–B systems according to the corrosion resistance of electric-arc coatings. *Mater Sci.*, **52**, 165–172. DOI: https://doi.org/10.1007/s11003-016-9939-8
11. Zhang, T., Yang, K., Zhu, Z. et al. (2024) Effect of Cr and W on microstructure and wear resistance of arc additive manufactured flux-cored wire for railway wheels. *J. of Materials Research and Technology*, **30**, 3438–3447. DOI: https://doi.org/10.1016/j.jmrt.2024.04.088
12. Malinov, V.L. (2006) Sparsely alloyed consumables providing in the deposited metal deformation hardening in operation. *The Paton Welding J.*, **8**, 25–28.
13. Babinets, A.A., Ryabtsev, I.O., Lentyugov, I.P. (2025) Methodology for evaluating the welding and technological properties of flux-cored wires for arc surfacing. *Avtomatychne Zvaryuvannya*, **2**, 38–44 [in Ukrainian]. DOI: https://doi.org/10.37434/as2022.02.05
14. TUU 28.7.05416923.066–2002: *Flux-cored wires for surfacing*. Kyiv, PWI [in Russian].

ORCID

S.Yu. Maksymov: 0000-0002-5788-0753,
A.A. Babinets: 0000-0003-4432-8879,
I.P. Lentyugov: 0000-0001-8474-6819,
V.V. Osin: 0009-0001-3257-8515

CONFLICT OF INTEREST

The Authors declare no conflict of interest

CORRESPONDING AUTHOR

A.A. Babinets
E.O. Paton Electric Welding Institute of the NASU
11 Kazymyr Malevych Str., 03150, Kyiv, Ukraine.
E-mail: a_babinets@ukr.net

SUGGESTED CITATION

S.Yu. Maksymov, A.A. Babinets, I.P. Lentyugov, V.V. Osin (2025) Welding and technological properties of sparsely alloyed flux-cored wires for strengthening and repair of parts by arc surfacing. *The Paton Welding J.*, **7**, 18–22.
DOI: https://doi.org/10.37434/tpwj2025.07.03

JOURNAL HOME PAGE

https://patonpublishinghouse.com/eng/journals/tpwj

Received: 13.02.2025
Received in revised form: 24.04.2025
Accepted: 02.07.2025

DOI: https://doi.org/10.37434/tpwj2025.07.04

METHODS FOR INCREASING THE FATIGUE LIFE OF DEPOSITED PARTS (REVIEW)

I.O. Ryabtsev, A.A. Babinets, I.I. Ryabtsev, I.P. Lentyugov

E.O. Paton Electric Welding Institute of the NASU
11 Kazymyr Malevych Str., 03150, Kyiv, Ukraine

ABSTRACT

A review of literature data on the problem of increasing the fatigue life of deposited parts operated under the simultaneous action of various types of wear and cyclic mechanical loads is presented. It is shown that an increase in the fatigue life of deposited parts can be achieved by rational selection and optimization of the chemical composition of surfacing materials, development of the optimal design of deposited layers and the use of the technology of sequential surfacing of hard wear-resistant layers and intermediate layers with high ductile characteristics.

KEYWORDS: arc surfacing, multilayer surfacing, repair surfacing, ductile sublayer, fatigue life, fatigue cracks, stress intensity factor

INTRODUCTION

The service life of machine and mechanism parts in various industries depends primarily on their operating conditions and properties of the materials from which they are made. Many of these parts are operated simultaneously under different types of wear and cyclic mechanical loads of unequal varying intensity. The combination of such operating conditions often leads to premature and, sometimes, emergency failure of expensive process equipment. The time spent on replacing worn parts and subsequent reconfiguration of equipment reduces labour efficiency and significantly increases material costs.

This problem is particularly relevant for the mining and metals and machine-building industries, where high-performance equipment is used. Stopping the equipment to replace worn parts leads to losses caused from unproduced products that can be many times higher than the direct costs on purchasing new parts and replacing worn ones. These parts include cold and hot forming rolls and dies; rollers for continuous casting machines; parts of the support and rotary devices of lifting machines and excavators; teeth of large-module gears, etc. [1–4].

At the same time, many of these parts are deposited during manufacturing or repeatedly restored by surfacing methods after partial wear and reused [1]. In the course of further long-term operation under the simultaneous action of wear and cyclic mechanical loads, fatigue cracks can arise and propagate in the deposited and base metal, causing accidental failure of a part (Figure 1) [5].

The residual tensile stresses occurring as a result of the effect of thermal surfacing cycle contribute to the reduction in the cyclic fatigue life of deposited parts. The intensity of fatigue damage accumulation during cyclic loading of multilayer deposited metal can also be negatively affected by its structural and chemical heterogeneity.

In addition, during surfacing of hard-to-weld high-alloy steels and alloys, on structural carbon and high-carbon steels, which are also welded poorly,

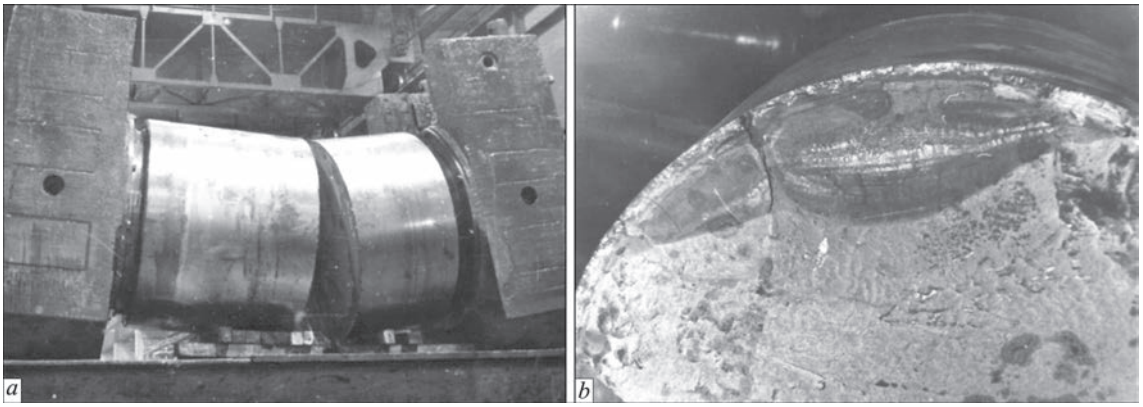

Figure 1. Fatigue fracture of a deposited roll: *a* — appearance of the roll with bearing assemblies after fracture; *b* — macrostructure of the crack initiation and propagation zone [5]

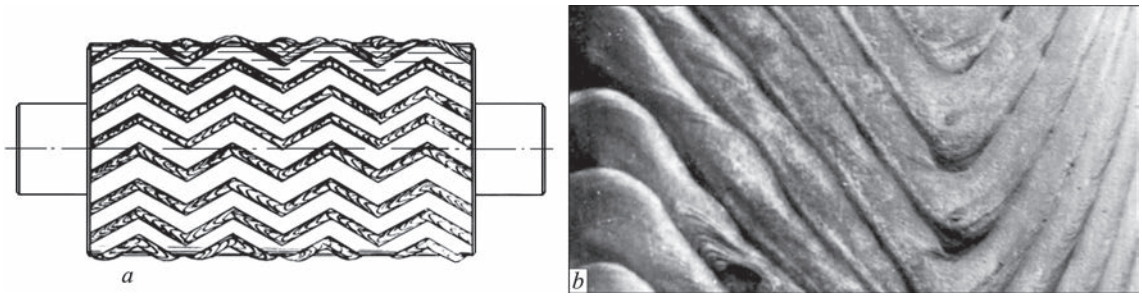

Figure 2. Surfacing of zigzag (*a*) and sinusoidal (*b*) beads with gaps between them to inhibit fatigue crack propagation [16]

there is a probability of formation of various defects. These defects can also serve as a source for initiation of fatigue cracks. Moreover, an increase in the number of deposited layers causes not only an increase in the probability of defect formation, but also in the level of residual tensile stresses, which can significantly reduce the cyclic fatigue life of deposited parts [1, 2].

It should also be remembered that surfacing materials with a higher degree of alloying are often used to increase the fatigue life and other operational properties of parts, as the properties of the cast deposited metal are usually inferior to those of a deformed metal of the same chemical composition [1–4]. However, this approach causes a growing cost of surfacing technology and the probability of forming defects in the deposited metal and at its fusion interface with the base metal.

THE AIM OF THE PAPER

is to summarize the data on methods for increasing the fatigue life of deposited parts obtained by the authors of the article and other researchers; to develop recommendations for their practical use in industry.

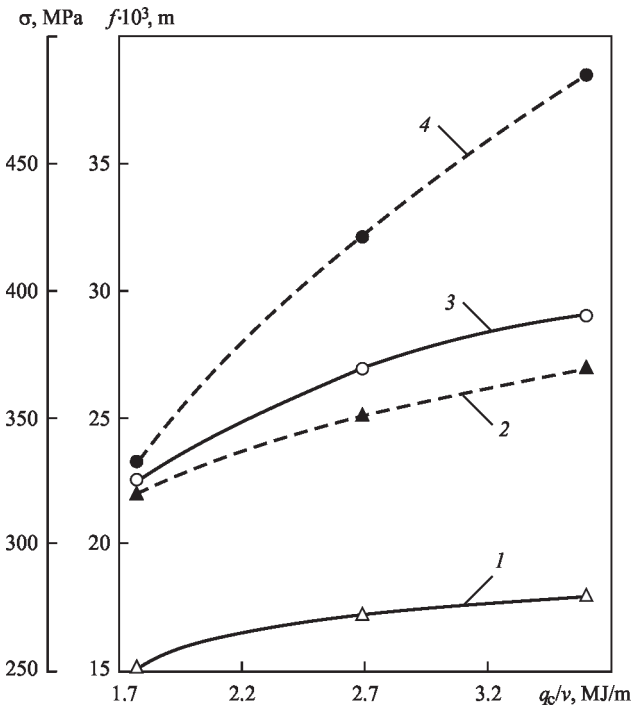

Figure 3. Dependence of welding stresses σ (*3*, *4*) and deflection strains *f* (*1*, *2*) in plates with dimensions of $(8\times120\times900)\cdot10^{-3}$ m (dashed curves) and $(30\times120\times900)\cdot10^{-3}$ m (solid curves) on welding heat input [9]

THE MAIN METHODS FOR INCREASING THE FATIGUE LIFE OF DEPOSITED PARTS

An analysis of the literature data shows that one of the most widespread methods for increasing the fatigue life of deposited parts is surface hardening [6], heat treatment [7, 8], reduction in the heat input of surfacing [9–11], etc. The mentioned operations reduce residual tensile stresses or create compressive stresses that contribute to an increase in fatigue crack resistance [12–15].

However, the depth of effect of most mechanical and chemical types of surface hardening ranges from 0.03 to 2.0 mm, and heat treatment capable of forming a specified structure to a greater depth (from 3 to 100 mm or more) is associated with significant energy losses and the need in using complex and large-sized equipment.

It is suggested to use methods for inhibiting crack growth, which consist in creating a system of other cracks that are more favourably located and can significantly reduce the value of tensile stresses. This is achieved, in particular, during formation of each deposited layer by depositing beads along a sinusoidal or zigzag trajectory (Figure 2) [16]. In this case, the effect of crack inhibition due to intersection with other cracks is used. However, the prospects of this approach in terms of the fatigue life of a part as a whole are rather doubtful, since it is almost impossible to control and regulate the location and propagation of cracks in the deposited metal. It is also impossible to guarantee that these cracks, in turn, will not become the beginning of fatigue failure.

Methods aimed at reducing the surfacing heat input [15, 16] may be promising. This is explained by the fact that a decrease in the effective heating power of a product by the welding arc leads to a decrease in the level of residual tensile stresses and strains (Figure 3), as well as refinement of the deposited metal structure as a result of an increase in the crystallization rate, which has a positive effect on crack resistance.

In our opinion, the most promising way to increase the fatigue life of deposited parts made of carbon

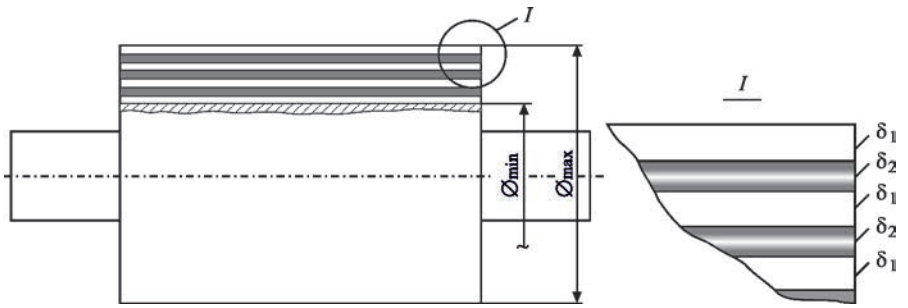

Figure 4. Design of a multilayer deposited metal of a roll made alternately using materials with lower (δ_1) and higher (δ_2) elastic moduli [5]

structural steels is to use multilayer surfacing with the sequential deposition of hard wear-resistant and ductile steels and alloys.

In [17], to increase the fatigue life of parts, it is proposed to use materials with different mechanical properties for their surfacing, creating a kind of barriers that help to inhibit the propagation of cracks or arrest them completely due to the need in additional energy consumption to overcome the boundary between the layers. Thus, when studying the effect of surfacing on the fatigue resistance of bronze-steel bimetal, it was found that the fusion boundary of two dissimilar materials acts as a barrier to crack growth that initiated on the surface [2].

Some researchers [5, 14, 17 and 18] propose alternating high-strength and ductile layers (Figure 4), which, in their opinion, can arrest cracks oriented perpendicular to the layer boundary. Thus, according to [14], a composition consisting of 3 layers (20Kh6GMFS + 12GS + 20Kh6GMFS) sequentially deposited one on top of the other has a higher crack resistance than a homogeneous three-layer metal of the 20Kh6GMFS type.

Studies in this direction, conducted at the PWI [2, 19–29], confirmed that an increase in the fatigue life of deposited parts can be achieved by rational selection and optimization of the chemical composition of materials for surfacing, development of the optimal design of deposited layers and the use of surfacing technology of intermediate layers with high ductile characteristics.

In particular, fatigue tests of deposited specimens without and with a sublayer with high ductility characteristics showed that the fatigue life of specimens with a sublayer was 40 % higher than that of specimens without a sublayer [19, 20 and 23].

It was found that the cyclic fatigue life of 40Kh steel specimens deposited using PP-Np-25X5FMS flux-cored wire with a sublayer deposited using Sv-08A solid wire with maximum compressive stresses from the zero cycle of 600 MPa exceeds $2 \cdot 10^6$ cycles of stress changes. The fatigue fracture kinetics of these specimens showed that the main crack mainly propagates along the fusion boundary of individual beads. No fatigue cracks parallel to the main one were found, unlike the specimens deposited without a sublayer. After the crack passed through the wear-resistant deposited layer and the sublayer, the specimens were fractured along the base metal [19, 20 and 23].

Paper [19] presents the results of determining the stress intensity factor (SIF) for the base metal (40Kh steel), the sublayer metal deposited using solid Sv-08A wire, and the wear-resistant layer metal deposited using flux-cored PP-Np-25Kh5FMS wire. SIF is an indicator of the stress intensity at the crack tip, and it characterizes the operability of a particular metal in the presence of cracks. It was found [19] that in the wear-resistant deposited 25Kh5FMS metal, the fatigue crack propagated unstably and its rate was constantly changing in the range of values 10^{-8}–10^{-7} m/cycle (SIF 45–60 MPa$\sqrt{m}$). In the metal of the sublayer, the fatigue crack growth rate increases by an order of magnitude: up to $2 \cdot 10^{-7}$–$2 \cdot 10^{-6}$ m/cycle in the SIF range of 60–100 MPa$\sqrt{m}$. In the base metal of 40Kh steel, the crack propagated steadily at a constantly increasing rate of $6 \cdot 10^{-7}$–$7 \cdot 10^{-6}$ m/cycle until the specimen fractured at SIF 140–180 MPa$\sqrt{m}$.

The analysis of the microstructure of the specimens also revealed that the fine grain size of the structure and a more uniform distribution of alloying elements in the specimen deposited with a sublayer of low-carbon rimmed steel 08kp, compared to other specimens, as well as its high ductile properties, have a positive effect on the resistance to fatigue cracking. This explains the 2.4–3.0-fold increase in the fatigue life of specimens with a low-carbon steel sublayer compared to other specimens [19, 20, 23].

The comparative fractographic analysis of fractures of multilayer specimens showed that specimens deposited with a sublayer of low-carbon rimmed steel 08kp and a wear-resistant working layer of 25Kh5MFS steel, which have a fairly uniform fibrous fracture type in the areas of the deposited and base metal, provide the best indices of fatigue life. Fractures of multilayer specimens deposited with a sublayer of low-alloy 12K1MF steel and a wear-resistant working layer of 25Kh5MFS steel have a predominantly crystalline nature and a high heterogeneity of the fracture sur-

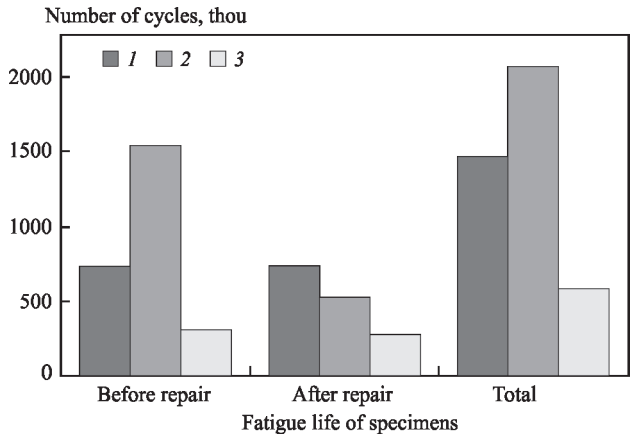

Figure 5. Fatigue life of deposited specimens before and after repair: *1* — surfacing using PP-Np-25Kh5FMS wire without a sublayer; *2* — the same, with rimmed steel 08kp sublayer; *3* — the same with 12Kh1MF sublayer [2]

face in the area of deposited metal, where there is a large number of columnar precipitations of crystalline type associated with the redistribution of carbon and chromium. This nature of fractures leads to a decrease in the fatigue life of multilayer deposited specimens [19, 20, 23 and 29].

The authors investigated the possibilities of repair (restorative) surfacing of specimens with fatigue cracks [2]. It was found that the cyclic fatigue life of 40Kh steel specimens with a deposited wear-resistant layer without or with a sublayer of rimmed steel 08kp after restorative repair is 31–56 % of the fatigue life of defect-free specimens after fabrication surfacing (Figure 5).

It was proved that repair of multilayer deposited parts after long-term operation, i.e. after the number of cycles close to the fatigue life at fabrication surfacing, is not effective, since it does not provide a significant increase in the fatigue life after repair due to the high level of accumulated fatigue damage in the wear-resistant deposited metal at a distance from the repair site.

CONCLUSIONS

1. The analysis of literature data shows that one of the most widespread methods of increasing the fatigue life of deposited parts is surface hardening, heat treatment and reduction in surfacing heat input, which result in the reduction of residual tensile stresses or creation of compressive stresses that contribute to the fatigue crack resistance of the deposited metal.

2. Increasing the fatigue life of deposited parts can be achieved by the rational selection and optimization of the chemical composition of surfacing materials, development of the optimal design of deposited layers, and the use of surfacing technology of intermediate layers with high ductile characteristics.

3. It is shown that repair of multilayer deposited parts after long-term operation, i.e., after the number of cycles close to the fatigue life at fabrication surfacing is not effective, since it does not lead to a significant increase in the fatigue life after repair as a result of the high level of accumulated fatigue damage in the wear-resistant deposited metal at a distance from the repair site.

REFERENCES

1. Ryabtsev, I., Fomichov, S., Kuznetsov, V. et al. (2023) *Surfacing and additive technologies in welded fabrication*. Springer Nature Switzerland AG. DOI: https://doi.org/10.1007/978-3-031-34390-2
2. Ryabtsev, I.A., Senchenkov, I.K., Turyk, E.V. (2025) *Surfacing. Materials, technologies, mathematical modeling.* Gliwice, Poland.
3. Czuchryj, J. (1991) Effects of arc surfacing on the fatigue strength of shafts. *Welding Inter.*, 5(**11**), 867–870. DOI: https://doi.org/10.1080/09507119109446804
4. Gulakov, S.V., Chigarev, V.V., Ivanov, V.P. et al. (2004) Improvement of technology for hardfacing of metallurgical equipment components. *The Paton Welding J.*, **10**, 48–51.
5. Ivanov, V.P., Stepnova, Yu.A. (2015) Improvement of technology for hardfacing of standard hot rolls by heterogeneous working layer. *Visnyk PDTU. Seriya: Tekhnichni Nauky,* **31**, 98–105. DOI: https://doi. org/10.31498/2225-6733.31.2015.71147
6. Dudnikov, A., Dudnikov, I., Kelemesh, A., Gorbenko, O. (2019) Improving the technology of part machining by surface plastic deformation. *Eastern-European J. of Enterprise Technologies*, 6(**1**), 26–32. DOI: https://doi.org/10.15587/1729-4061.2019.183541
7. Makhnenko, V.I., Shekera, V.M., Kravtsov, T.G., Sevryukov, V.V. (2001) Effect of subsequent mechanical treatment on redistribution of residual stresses in surfaced shafts. *The Paton Welding J.*, **7**, 2–5.
8. Zakharova, I. (2024) Welding processes in the restoration of industrial and energy facilities. *Machinery & Energetics*, 15(**1**), 56–64. DOI: https://doi.org/10.31548/machinery/1.2024.56
9. Chigaryov, V.V., Shchetinina, V.I., Shchetinin, S.V. et al. (2009) Increase of crack resistance of shrouded traveling rolls in high-speed hardfacing. *The Paton Welding J.*, **1**, 22–25.
10. Shchetinin, S.V. (2016) Improvement of crack resistance of banded supporting rolls at high-speed surfacing with low heat input. *The Paton Welding J.*, **8**, 10–14. DOI: https://doi.org/10.15407/tpwj2016.08.03
11. Krukovich, M.G., Klochkov, N.P., Savelieva, A.S. (2014) Ways for improvement of service life of parts restored by surfacing methods. *Novye Materialy i Tekhnologii v Mashinostroenii,* **20**, 45–50.
12. Brodovoj, V.A., Gushcha, O.I., Kuzmenko, A.Z., Mikheev, P.P. (2001) Interaction of residual stresses in the zones of stress concentrators and fatigue cracks. *The Paton Welding J.*, **9**, 42–43.
13. Gopkalo, A.P., Klipachevsky, V.V. (2015) Effect of surfacing on stress-strain state of rollers of machines for continuous casting of billets. *The Paton Welding J.*, **5–6**, 140–141. DOI: https://doi.org/10.15407/tpwj2015.06.31
14. Brodovoj, V.A., Mikheev, P.P., Knysh, V.V. et al. (2003) Effectiveness of fatigue crack retardation by the field of compressive residual stresses. *The Paton Welding J.*, **8**, 49–50.

15. Samotugin, S.S., Leshchinsky, L.K., Mazur, V.A., Samotugina, Yu.S. (2013) *Tool materials: properties and hardening.* Mariupol, PGTU.
16. Leshchinsky, L.K., Samotugin, S.S. (2005) *Lamellar surfaced and hardened compositions.*Mariupol, Novyi Mir.
17. Dombrovsky, F.S, Leshchinsky, L.K. (1995) *Serviceability of surfaced rolls of billet continuous casting machines.* Kyiv, PWI.
18. Korotkov, V.A., Chubelov, V.A. (2000) Depositing contact□loaded surfaces with alternating hard and soft sections. *Welding Inter.*, 14(**9**), 722–724. DOI: https://doi.org/10.15407/10.1080/09507110009549257
19. Ryabtsev, I.O., Knysh, V.V., Babinets, A.A., Solovei, S.O. (2022) *Fatigue life of surfaced parts.* Kyiv, Interservice.
20. Ryabtsev, I.A., Babinets, A.A., Ryabtsev, I.I. (2016) Fatigue life of multilayer hard-faced specimens. *Welding Inter.*, 30(**4**), 305–309. DOI: https://doi.org/10.1080/01431161.2015.1058004
21. Ryabtsev, I.A., Senchenkov, I.K. (2013) *Theory and practice of surfacing works.* Kyiv, Ekotekhnologiya.
22. Senchenkov, I.K., Chervinko, O.P., Ryabtsev, I.A. (2015) Calculation of fatigue life of cylindrical parts at multilayer surfacing and service cyclic thermo-mechanical loading. *The Paton Welding J.*, **5–6**, 134–139. DOI: https://doi. org/10.15407/tpwj2015.06.30
23. Senchenkov, I.K., Chervinko, O.P., Ryabtsev, I.A., Babinets, A.A. (2014) Determination of the service life of hard-faced components under thermal and cyclic loading. *Welding Inter.*, **28**(**1**), 80–84. DOI: https://doi.org/10.1080/09507116.2013.796661
24. Babinets, A.A., Ryabtsev, I.A., Kondratiev, I.A. et al. (2014) Investigation of thermal resistance of deposited metal designed for restoration of mill rolls. *The Paton Welding J.*, **5**, 16–20. DOI: https://doi.org/10.15407/tpwj2014.05.03
25. Barvinko, A.Yu., Knysh, V.V., Barvinko, Yu.P., Yashnik, A.N. (2012) Development of surface crack-like defect in welded joints of 06GB-390 steel at cyclic loading. *The Paton Welding J.*, **5**, 40–42.
26. Knysh, V.V., Solovei, S.O. (2013) Increase in fatigue resistance of welded joints with accumulated fatigue damage. *Visnyk TNTU,* **3**, 189–197.
27. Knysh, V.V. (2014) Method of calculation assessment of cyclic crack resistance in metal cyclic elements taking into account the influence of welding residual stresses. In: *Fracture mechanics and physics of construction materials and structures.* Ed. by Y.Y.Luchko. Lviv, Issue **10,** 239–250.
28. Knysh, V.V., Solovej, S.A., Nyrkova, L.I. et al. (2016) Improvement of cyclic fatigue life of tee welded joints by high-frequency mechanical peening under the conditions of higher humidity and temperature. *The Paton Welding J.*, **3**, 19–24. DOI: https://doi.org/10.15407/tpwj2016.03.02
29. Ryabtsev, I.O., Babinets, A.A., Student, O.Z. et al. (2022) Substantiation of the choice of materials for surfacing based on the fractographic analysis of fatigue fractures. *Mater. Sci.*, 58(**1**), 126–134. DOI: https://doi.org/10.1007/s11003-022-00640-8

ORCID
I.O. Ryabtsev: 0000-0001-7180-7782,
A.A. Babinets: 0000-0003-4432-8879,
I.I. Ryabtsev: 0000-0001-7550-1887,
I.P. Lentyugov: 0000-0001-8474-6819

CONFLICT OF INTEREST
The Authors declare no conflict of interest

CORRESPONDING AUTHOR
I.O. Ryabtsev
E.O. Paton Electric Welding Institute of the NASU
11 Kazymyr Malevych Str., 03150, Kyiv, Ukraine.
E-mail: ryabtsev39@gmail.com

SUGGESTED CITATION
I.O. Ryabtsev, A.A. Babinets, I.I. Ryabtsev, I.P. Lentyugov (2025) Methods for increasing the fatigue life of deposited parts (Review). *The Paton Welding J.*, **7**, 23–27.
DOI: https://doi.org/10.37434/tpwj2025.07.04

JOURNAL HOME PAGE
https://patonpublishinghouse.com/eng/journals/tpwj

Received: 27.11.2024
Received in revised form: 12.02.2025
Accepted: 08.07.2025

DOI: https://doi.org/10.37434/tpwj2025.07.05

ENHANCING LARGE-SCALE STRUCTURE DIAGNOSTICS THROUGH UAV-BASED DATA AND NEURAL NETWORK ANALYSIS

L.M. Lobanov, I.L. Shkurat, D.I. Stelmakh, O.P. Shutkevych, V.V. Savitsky

E.O. Paton Electric Welding Institute of the NASU
11 Kazymyr Malevych Str., 03150, Kyiv, Ukraine

ABSTRACT

The article presents an approach to remote diagnostics of damage to large-scale engineering structures using unmanned aerial vehicles (UAVs) and convolutional neural networks. The study was conducted to automate the process of detecting structural defects in the Kyiv TV tower. The research methodology involved the collection and preprocessing of 14187 images and the development of a modified architecture of the U-Net neural network for damage segmentation. An experimental study of different architectural settings of the model demonstrated the effectiveness of the proposed modifications, which allowed reducing the error of defect detection by 3–5 % compared to the baseline models. It was found that the optimal number of training iterations is 15–20 epochs. The developed model demonstrated the ability to detect damage that may be missed by the operator, which confirms the potential of automated diagnostic systems based on artificial intelligence. The study provides new prospects for improving the efficiency of monitoring infrastructure facilities, especially under conditions of limited access or increased risks to personnel.

KEYWORDS: remote diagnostics, defects, artificial intelligence, neural networks, image segmentation, UAVs

INTRODUCTION

Systematic monitoring of the technical condition of large-scale facilities is important for assessing their structural integrity. Over time, structures undergo changes caused by corrosion, ageing of materials, loads and external factors.

For the safe and continuous operation of large-scale facilities, it is necessary to periodically monitor and timely identify defective areas, determine the necessary preventive measures and plan priority repairs. This is especially relevant in the military and post-war periods, when infrastructure facilities suffer significant damage.

Non-destructive testing (NDT) methods are widely used as a diagnostic tool for engineering structures to assess their technical condition [1–4]. Conventional NDT methods, such as ultrasonic testing [5, 6], magnetic particle method [7], acoustic emission [8, 9], infrared thermography [10, 11], etc., although showing a significant progress, have a number of limitations. In particular, their accuracy depends on external factors (humidity, temperature, noise level), and the interpretation of the results can be complicated by the subjective factor of the operator. In addition, such methods are labour-intensive, require high financial costs, and envisage direct personnel involvement, which increases the level of risks, especially when inspecting large-scale and hard-to-access structures.

One of the most effective ways to visually inspect engineering structures is to use unmanned aerial vehicles (UAVs). Due to the rapid development of technologies, UAVs have been integrated into the system of remote monitoring of infrastructure facilities, demonstrating high efficiency in hard-to-access places where the use of traditional methods is limited [12–17]. Compared to traditional methods, surveys using UAVs are much faster and provide high spatial resolution of images. This allows obtaining detailed data with high accuracy, which is important for analyzing the condition of facilities and making reasoned decisions [18]. Their use not only improves the accuracy and speed of monitoring, but also significantly reduces the human and time resources, while minimizing the risks to the service personnel [19–22].

Due to the spread and improvement of artificial intelligence (AI) and neural networks (NN), the process of detecting defects in large-scale structures is gradually developing towards automation and intellectualization. This methodology is based on the high efficiency of neural networks in detecting and processing features, contributing to improving the quality and accuracy of the process of detecting defective areas.

The use of AI and NN in the field of data analysis is determined by their ability to automatically train and adapt to various input conditions, which makes these technologies promising in the context of improving the reliability and speed of defect localization processes on large-scale structural elements.

There are approaches to defect recognition based on the use of different NN architectures, training methods, and the choice of hyperparameters. The

NN hyperparameters are set manually or automatically before the training process starts: the number of layers in the NN, the type of activation function, the optimizer, etc. The choice of hyperparameters significantly affects the model accuracy, training speed, and quality of the obtained results. In particular, convolutional neural networks (CNNs) are quite effectively used to solve the problems of classification, segmentation, recognition and detection of defects in images.

With the development of computing capacities and the growth of image databases [23], CNN architectures continue to improve [24]. Compared to standard feed-forward NNs, convolutional NNs have significantly fewer couplings and parameters, which makes them less resource-intensive in training. CNNs use assumptions about the locality of pixel interactions, which allows them to effectively outline key structural elements of an image, reducing the number of parameters that need to be optimized [25].

Convolutional NNs are particularly effective for image processing tasks, as they automatically identify various image features at different levels of their representation. Due to applying the convolutional operation, CNNs are able to detect structural features in the input data, which ensures high accuracy in classification [26], segmentation [27, 28], and object recognition tasks [29, 30].

In recent years, the scientific community has made a significant progress in the application of machine training methods in various fields. In particular, NNs are actively used to detect defective areas based on images, including crack detection in concrete [31], exfoliation and surface delamination processes [32], fatigue cracks [33], and corrosion of steel structures [34]. The introduced image processing methods can partially replace the traditional monitoring carried out by operators in-situ, providing more efficient and accurate detecting features of defects on concrete and metal surfaces [35–38]. A considerable interest is paid to studies demonstrating the effectiveness of using UAVs in combination with deep training methods for the accurate identification of defective areas [39, 40].

Thus, the introduction of AI into the remote diagnostics of large-scale structures is a relevant area of automated diagnostics development aimed at enhancing the monitoring efficiency, optimizing resources, and improving the accuracy, speed, and reliability of detecting defective areas.

METHODOLOGY. DATA COLLECTION AND PREPARATION FOR NEURAL NETWORK TRAINING

The Kyiv TV tower, which suffered structural damage as a result of a missile strike, was chosen as the object of survey. A UAV with a camera resolution of 5280×3956 pixels was used to conduct remote diagnostics of the lower tier of the Kyiv TV tower. Planning the flight path is an important step that directly affects the efficiency of remote monitoring and data collection tasks.

The overflight methodology involved the following stages:

- determining a flight path that provides an optimal inspection of the object, taking into account the requirements for spatial positioning accuracy;
- taking into account the influence of external factors, such as weather conditions (wind, angle of incidence of sunlight, precipitation), safety rules (altitude restrictions, restricted flight zones), accuracy requirements (resolution, coverage).

The remote monitoring of the lower tier of the Kyiv TV tower consisted of video scanning of the outer surface from bottom to top, trajectory correction by side movement, and further scanning in the opposite direction (top to bottom). Taking into account the geometric parameters and configuration of the elevator shaft, the flight was performed in a circular path. The closed flight path around the shaft minimizes the risk of loss of spatial coverage.

To minimize the impact of uneven lighting, the monitoring was carried out under stable weather conditions with an even distribution of natural light. This allowed avoiding sharp contrasts and improving image quality for further analytics.

An analysis of possible risks was conducted, which involved:

- alternative flight routes;
- backup takeoff and landing points;
- algorithms for emergency return of an UAV in case of loss of communication.

The data was collected at the lowest possible distance to the object in the "slow flight" mode, which helped to enhance the spatial resolution and quality of the obtained images. Optimization of the viewing angle was achieved by dynamically adjusting the camera tilt to minimize shadowing and ensure a full coverage of structural elements. The flight height was varied depending on the size of the structural elements of the lower tier of the TV tower to obtain highly detailed images from different angles.

After data collection, the images were processed, which involved the following steps:

- framing, which resulted in generating a set of images with a resolution of 5472×3078 pixels;
- size adaptation for further processing by the neural network, namely, each image was divided into smaller fragments of 128×128 pixels with an overlap of 50 % in width and height. This approach ensured a

uniform coverage of the images and the creation of a diverse training set. As a result, 14187 segments were obtained, that were prepared for NN training;

● annotating defective areas, which was carried out in the Labelme software environment using polygon meshes, which allowed for accurate marking the contours of objects by approximating with polygons;

● normalization of brightness and contrast in the Labelme software environment, which allowed for detection of low-contrast damage that was not clearly visible in the output images;

● classification of damage in the images into two types: corrosion and significant structural defects (holes, cracks);

● creation of masks that were used to segment the damage and outline the key areas of analysis.

NEURAL NETWORK ARCHITECTURE

Detecting structural defects in images is a segmentation task that involves classifying each pixel of the input image. Convolutional neural networks (CNNs) are used to solve such tasks, in particular, the U-Net architecture and its modifications. Differences between the U-Net variations: number of layers and filters, use of normalization, type of activation function, loss function, etc. [41].

In order to improve the segmentation efficiency, a series of experiments were conducted with different configurations of the U-Net architecture (Figure 1). The following parameters varied: the initial number of convolutional layer filters, the number of convolutional operation levels, and the activation functions.

To improve the efficiency of the NNs based on the U-Net architecture, the following improvements were used:

● adding a concatenation mechanism for the corresponding encoder and decoder layers to preserve spatial information;

● doubling of the number of convolutional layers to improve the model's ability to extract features;

● normalizing input data to enhance the stability of the training process.

NEURAL NETWORK TRAINING

The NN models were implemented in Python 3.10.12 using the TensorFlow and Keras libraries, version 2.9.0. During NN training, its parameters were saved after each training epoch.

The created dataset was divided into training, validation, and test sets in the ratio of 80 to 20 %. The training dataset (images with corresponding meshes) was used to train the model, taking into account the training parameters, such as the number of epochs, the batch size, the training speed, and the loss function. Additionally, optimizers were used to adapt the model weights to minimize the loss function during training and to ensure efficient training and model convergence.

Data augmentation was used to enhance the model's generalization capability, i.e. its ability to work correctly on new, previously unseen data. This is an artificial increase in the diversity of the training set that improves the model's stability. For images, augmentation involved such methods as rotation, colour change, etc.

The parameters were optimized using the Adam algorithm with the Sparse Categorical Crossentropy loss function, where Adam is an algorithm that helps the neural network in finding the optimal weights faster and more accurately during training. Sparse Categorical Crossentropy is a way to measure NN error in

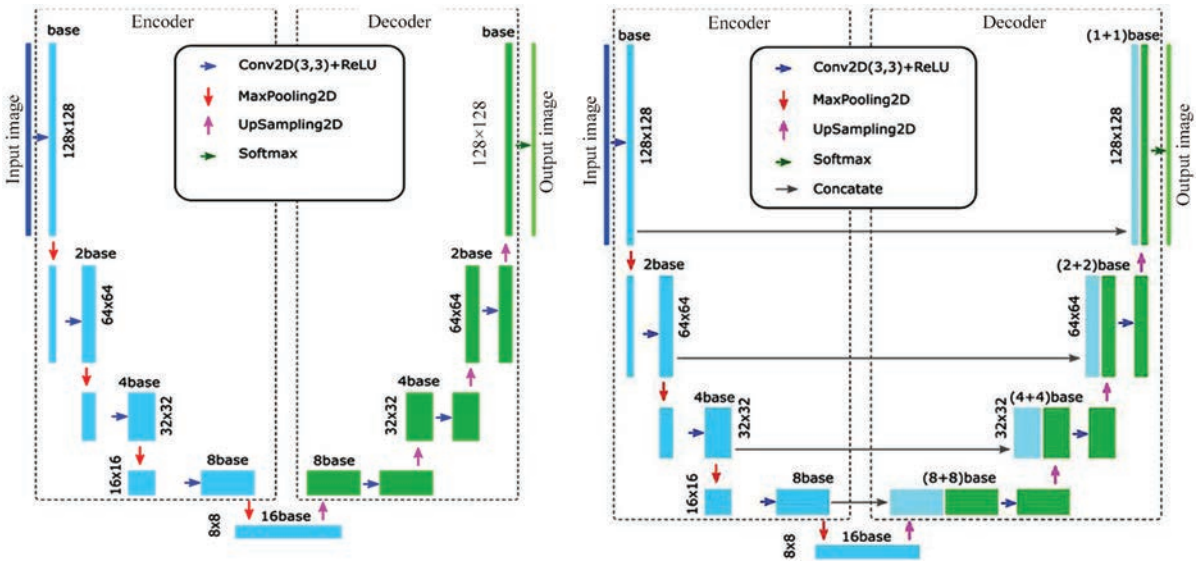

Figure 1. Architecture of the U-Net model: *a* — baseline model; *b* — model with additional layer coupling

Table 1. Influence of activation functions on U-Net model with different number of filters and parameters calculated during training

Initial number of filters (base)	Error on the training dataset (loss)	Error on the test dataset (val_loss)	Number of epochs	Number of model parameters
Linear function for activating the last layer				
4	0.0907	0.1131	20/50	49267
8	0.0520	0.0874	33/50	196451
16	0.0761	0.0894	15/50	784579
Activation of the last Softmax layer				
4	0.0561	0.0758	43/50	49267
8	0.0486	0.0824	30/50	196451
16	0.0626	0.1012	16/50	784579

classification when each image or object belongs to one of several classes.

The influence of different activation functions in the last layer of the network, including linear and Softmax was also tested, which allowed evaluating their effectiveness in recognizing classes of defects (Table 1).

The Softmax function is an activation function that is often used in machine learning, especially in classification tasks with several classes [41]. It converts a vector of arbitrary numbers (output values of a neural network) into a probability vector, where each value corresponds to the probability of belonging to a certain class. For the vector $z = [z_1, z_2, \ldots, z_n]$, where z_i is the output of the neural network for the i-th class, the Softmax function is calculated by the formula:

$$\text{Softmax}(z_i) = \frac{e^{z_i}}{\sum_{j=1}^{n} e^{z_j}}$$

where e^{z_i} is the exponent of the i-th element of the vector z; $\sum_{j=1}^{n} e^{z_j}$ is the sum of the exponents of all elements of the vector z.

Softmax is a probability vector where each value is in the range from zero to one, and the sum of all values is 1.

Table 1 shows the results of NN training, where the influence of the initial number of convolutional layer filters and the activation function of the output layer on the model accuracy is investigated. The evaluation is based on the loss function for the training (loss) and test (val_loss) datasets, the number of epochs required for training, and the total number of model parameters.

Comparison of the two output layer options (linear activation and Softmax) shows that using Softmax provides a lower test error (val_loss) in all configurations. This indicates a better generalization ability of the model, especially with fewer filters.

An increase in the number of filters (from 4 to 16) leads to an increase in the number of model parameters, which can improve its training ability, but also increases the risk of overtraining, when the model demonstrates high accuracy on training data, losing the ability to generalize on new, previously unseen test or actual data, especially when using a large number of filters (base = 16). This is confirmed by an increase in the error on the test set (val_ loss) after 15–20 epochs of training, which indicates a possible transition from generalization to overtraining.

Figure 2 shows the dependence of the loss function for the training and test datasets on the number of epochs during NN training when using a model with a linear activation function and a base number of filters of 4 (base = 4).

In the initial stages of training (0-10 epochs), there is a rapid decrease in both errors (loss and val_loss), which indicates that the model is training effectively. However, after the 20th epoch, the error on the training dataset (train_loss) continues to decrease, while the error on the test dataset (val_loss) starts to increase. This is a sign of overtraining, when the model loses its ability to generalize to new data. Thus, the optimal number of training iterations is 20 epochs, which prevents overmemorization of training samples.

One of the main characteristics that determine the effectiveness of NNs is the segmentation error (val_loss) on images that were not used to train the CNN model. As a result of carried out research, it was

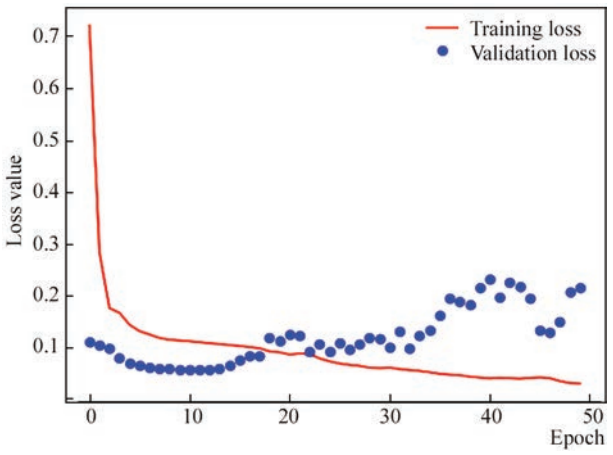

Figure 2. Dependence of the loss function for the training and validation datasets on the number of epochs during neural network training

Table 2. Testing results of improved U-Net models

Initial number of filters (base)	Error on the training dataset (loss)	Error on the test dataset (val_loss)	Number of epochs	Number of model parameters
Baseline model + block coupling				
4	0.0683	0.0703	36/50	61507
8	0.0601	0.0599	18/50	245411
16	0.0314	0.0656	36/50	980419
Baseline model with a doubled number of convolutional layers + block coupling				
4	0.1335	0.1342	26/50	86107
8	0.0483	0.0841	21/50	343571
16	0.0658	0.0527	10/50	1372579
Baseline model with a doubled number of convolutional layers + block coupling + normalization				
4	0.0403	0.0518	48/50	86587
8	0.0292	0.0575	15/50	344531
16	0.0308	0.0598	14/50	1374499

found that the error of defect detection ranged from 7 to 11 % (Table 1).

The optimal model configuration for generalizing the results is to use eight filters together with the Softmax activation function. This configuration provides the lowest test error value (0.0824).

The results of testing various modifications of the U-Net architecture with varying the initial number of filters, the number of convolutional layers, using normalization, and increasing the number of blocks are shown in Table 2.

Three variants of the U-Net model architecture were studied:

- baseline model with additional block coupling;
- baseline model with a doubled number of convolutional layers with block coupling;
- baseline model with a doubled number of convolutional layers, block coupling and normalization.

Each of these architectures was tested with a different initial number of filters (base = 4, 8, 16), which resulted in 9 different model configurations.

The baseline model with an increased number of blocks shows improved results compared to the initial architecture, but its accuracy is limited, especially with a small number of filters. Adding additional convolutional layers reduces the error on the training set, but without normalization, instability is observed on the test data, which is especially noticeable with the initial number of filters, base = 4 (val_ loss = 0.1342). The use of normalization in combination with an increase in the number of blocks and convolutional layers allows achieving a minimum error value on the test set val_loss = 0.0518 with base = 4, which indicates the effectiveness of this approach for less complex architectures. Thus, the best option is an architecture with a doubled number of convolutional layers, increased blocks, and normalization, which minimizes the error with a controlled model complexity.

Figure 3 shows the dependence of the loss function for the training and test datasets on the number of epochs during training of the baseline model with additional block coupling, as well as the improved U-Net model with a doubled number of convolutional layers, block coupling, and layer normalization.

The baseline model with additional block coupling (Figure 3, *a*) demonstrates fast training, but it is prone to overtraining, as evidenced by an increase in the error on the test dataset (val_loss) after 20 epochs.

Compared to Figure 2, a significant decrease in the difference in error values during training to 3–5 % can

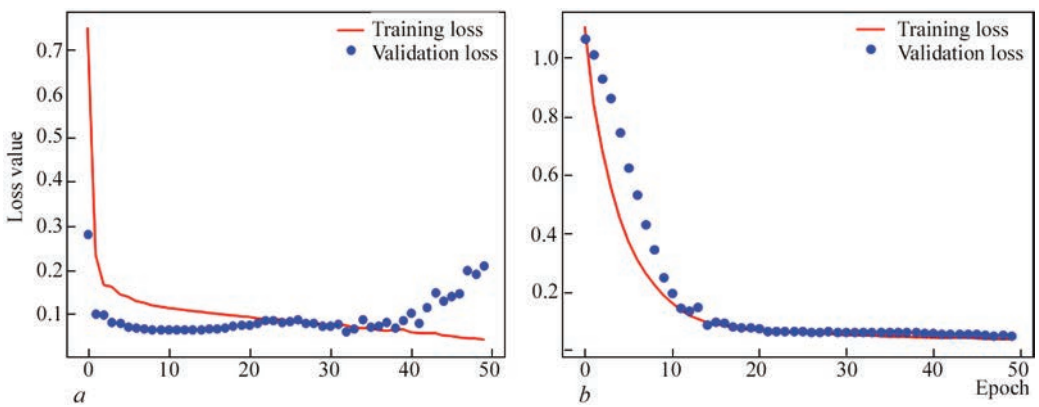

Figure 3. Dependence of the loss function for the training and test image datasets: *a* — baseline model with additional block coupling; *b* — improved U-Net model with a doubled number of convolutional layers, block coupling and layer normalization

be seen, which indicates a more accurate calculation of model parameters compared to using the baseline U-Net architecture (Figure 3, *a*).

At the initial stages of training (0–10 epochs) of the improved U-Net model (Figure 3, *b*), the values of the loss function for the training (loss) and test (val_loss) sets decrease rapidly. The close values of these errors at the start are explained by the fact that the model has not yet formed complex patterns and generalizations, therefore its efficiency on training and test data is similar. In the course of further training, the model adapts to the peculiarities of the training data. After 15–20 epochs, the training and test errors stabilize without significant differences, indicating good generalization and lack of overtraining. This indicates that the model has achieved optimal efficiency and can be effectively generalized to new data. Thus, the proposed modifications to the U-Net architecture have improved the model's accuracy in detecting defects in images of structures.

ANALYSIS OF THE OBTAINED RESULTS

Figure 4 shows the results of automatic detection of damaged areas in the images using the baseline model with the number of filters base = 4. A visual comparison of the areas marked by the operator (Figure 4, *b*) and the segmented areas obtained by the neural network (Figure 4, *c*) shows that the model is able to detect damage that remained unnoticed by the operator. However, the segmentation result obtained by the neural network has a significant error, missing areas, which indicates insufficient accuracy.

Figure 5 shows the results of applying the improved U-Net model, the number of filters base = 16 and with Softmax activation, which show a more accurate segmentation of defective areas, reducing the number of false classifications compared to the baseline version (Figure 4).

Figure 6 shows an example where the NN successfully identified a defective area caused by the penetration of debris through the wall of a tubular element of the TV tower, which was missed by the operator when creating the annotation. Comparison of the masks (Figures 6, *b* and 6, *c*) shows that the predicted damage areas coincide well with the actual data. This confirms the effectiveness of the model. The obtained results confirm the model's ability to detect damage that may remain unnoticed, thereby minimizing the influence of the human factor during the visual diagnostics of structures.

The obtained results demonstrate the effectiveness of the U-Net neural network for automatic damage detection. However, incomplete or inaccurate marking of defective areas by the operator in the training

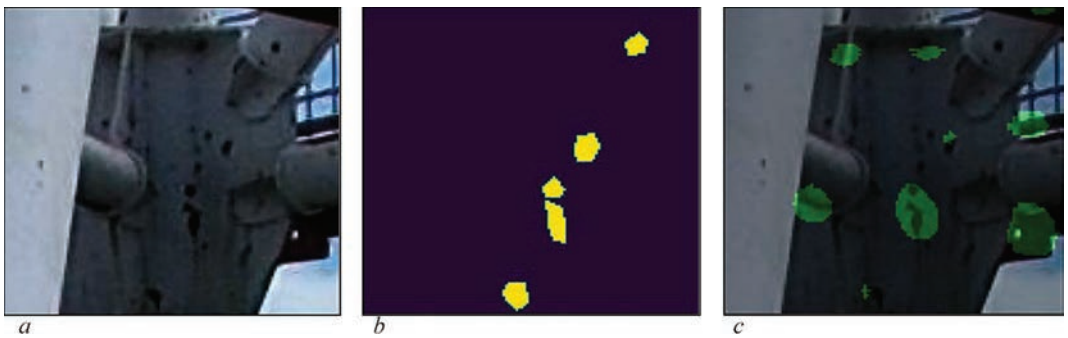

Figure 4. Automatic detection of damaged areas by the model with parameters: base = 4, the last activation layer is linear: *a* — fragment of the image with the damaged assembly; *b* — damaged areas marked by the operator in yellow; *c* — result of segmentation obtained by the neural network (green)

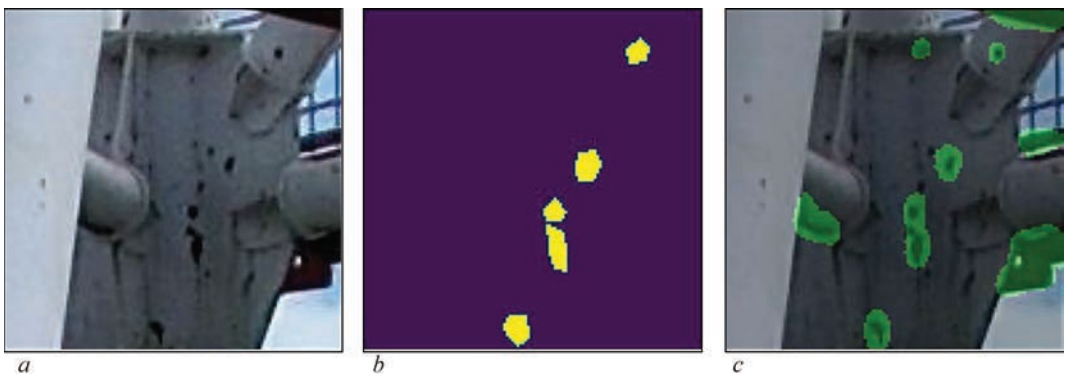

Figure 5. Automatic detection of damaged areas using the improved U-Net model with parameters: base = 16, the last activation layer is Softmax: *a* — fragment of the image with the damaged assembly; *b* — damaged areas marked by the operator in yellow; *c* — result of segmentation obtained by the neural network (green)

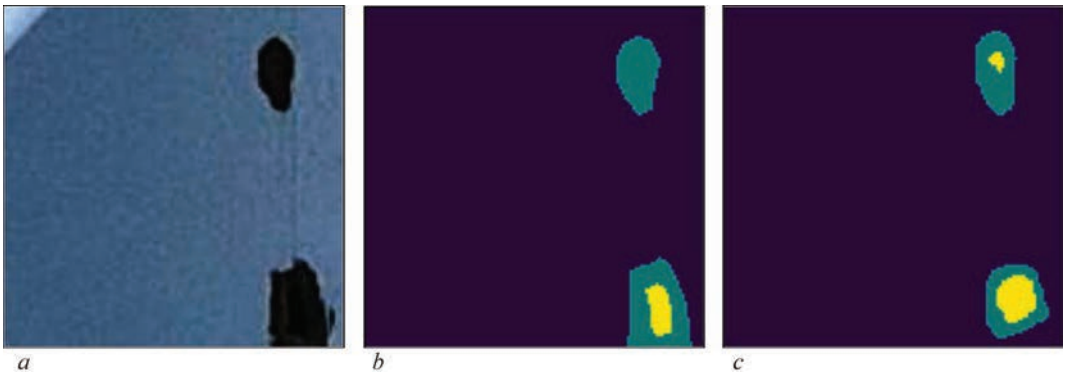

Figure 6. Automatic detection of damaged areas using the improved U-Net model with parameters: base = 16, the last activation layer is Softmax: *a* — fragment of the image with damaged areas; *b* — damaged areas marked by the operator; *c* — result of segmentation obtained by the neural network. Green colour indicates a corrosion damage, yellow — a hole. Model, number of filters — 16 (base = 16) with the last activation Softmax layer

dataset can negatively affect the quality of the model, since its training depends on the correspondence to the meshes marked by the operator. Therefore, the formation of a high-quality database with complete and accurate defect marking is an important factor in creating a highly accurate NN.

CONCLUSIONS

The carried out study confirmed the effectiveness of using neural networks for automated defect detection, which helps to improve the diagnostic accuracy and minimize the influence of the subjective factor.

The analysis of the effectiveness of different neural network architectures showed that models with more filters provide an improved defect detection capability, but their use requires significant computing resources and training time. The modified U-Net architectures, in particular by adding additional blocks and normalization, allowed reducing the defect detection error to 3–5 %, which is a significant improvement over the baseline models. It was found that the optimal number of iterations for training models with a modified architecture is 15–20, since further training leads to overtraining and an increase in the error on test data.

The use of modified neural network architectures with the use of mechanisms for normalization and adaptive adjustment of hyperparameters is a promising direction for improving the accuracy and reliability of automated defect diagnostics based on image analysis, which opens up opportunities for further integration of such systems into the monitoring process.

ACKNOWLEDGMENTS

The published results were obtained within the framework of the project 022.01/0095 “Development of technology for remote diagnostics of damaged large-scale objects based on the use of unmanned aerial vehicles (UAVs) and photogrammetry” funded by the National Research Foundation of Ukraine in the framework “Science for the Recovery of Ukraine in the War and Post-War Periods”.

REFERENCES

1. Balayssac, J.-P., Garnier, V. et al. (2018) *Non-Destructive testing and evaluation of civil engineering structures.* STE Press Ltd., Elsevier Science. DOI: https://doi.org/10.1016/C2016-0-01227-5
2. Reddy, K.A. (2017) Non-destructive testing, evaluation of stainless steel materials. *Mater. Today Proc.*, 4(**8**), 7302–7312. DOI: https://doi.org/10.1016/j.matpr.2017.07.060
3. Deepak, J.R., Raja, V.K.B., Srikanth, D. et al. (2021) Non-destructive testing (NDT) techniques for low carbon steel welded joints: A review and experimental study. *Mater. Today Proc.*, 44(**8**), 3732–3737. DOI: https://doi.org/10.1016/j.matpr.2020.11.578
4. Polimeno, M., Roselli, I., Luprano, V.A.M. et al. (2018) A non-destructive testing methodology for damage assessment of reinforced concrete buildings after seismic events. *Eng. Structures*, **163**, 122–136. DOI: https://doi.org/10.1016/j.engstruct.2018.02.053
5. Bahonar, M., Safizadeh, M. (2021) Investigation of real delamination detection in composite structure using air-coupled ultrasonic testing. *Composite Structures*, **280**, 114939. DOI: https://doi.org/10.1016/j.compstruct.2021.114939
6. Chen, Y., Kang, Y., Feng, B., Li, Y., Cai, X. (2022) Automatic defect identification in magnetic particle testing using a digital model aided de-noising method. *Measurement*, **198**, 111427. DOI: https://doi.org/10.1016/j.measurement.2022.111427
7. Van Steen, C., Pahlavan, P., Wevers, M., Verstrynge, E. (2018) Localisation and characterisation of corrosion damage in reinforced concrete by means of acoustic emission and X-ray computed tomography. *Construction and Building Materials*, **197**, 21–29. DOI: https://doi.org/10.1016/j.conbuildmat.2018.11.159
8. Suzuki, T., Ogata, H., Takada, R. et al. (2010) Use of acoustic emission and X-ray computed tomography for damage evaluation of freeze-thawed concrete. *Construction and Building Materials*, **24**, 2347–2352. DOI: https://doi.org/10.1016/j.conbuildmat.2010.05.005
9. Pedram, M., Taylor, S., Hamill, G. et al. (2022) Experimental evaluation of heat transition mechanism in concrete with subsurface defects using infrared thermography. *Construction and Building Materials*, **360**, 129531. DOI: https://doi.org/10.1016/j.conbuildmat.2022.129531
10. Shrestha, P., Avci, O., Rifai, S. et al. (2025) A review of infrared thermography applications for civil infrastructure. *Struc-*

tural Durability & Health Monitoring, 19(**2**), 193–231. DOI: https://doi.org/10.32604/sdhm.2024.049530
11. Lobanov, L.M., Stelmakh, D., Shkurat, I. et al. (2025) Determination of a TV tower verticality using UAVs, RTK and photogrammetry. In: *Proc. of VIIth Inter. Conf. on Welding and Related Technologies, Yaremche, Ukraine, 7–10 October 2024*, 149–153. DOI: https://doi.org/10.1201/9781003518518-30
12. Lobanov, L., Stelmakh, D., Savitsky, V. et al. (2024) Damage detection and analysis using unmanned aerial vehicles (UAVs) and photogrammetry method. *Procedia Structural Integrity*, **59**, 43–49. DOI: https://doi.org/10.1016/j.prostr.2024.04.008
13. Lobanov, L.M., Stelmakh, D.I., Savitsky, V.V. et al. (2023) Remote assessment of damage to Kyiv TV tower based on the application of aerial photography and photogrammetry method. *Tekh. Diagnost. ta Neruiniv. Kontrol,* **3**, 16–20 [in Ukrainian]. DOI: https://doi.org/10.37434/tdnk2023.03.03
14. Onososen, A., Musonda, I., Onatayo, D. et al. (2023) Impediments to construction site digitalization using unmanned aerial vehicles (UAVs). *Drones*, 7(**1**), 45. DOI: https://doi.org/10.3390/drones7010045
15. Albeaino, G., Gheisari, M., Franz, B.W. (2019) A systematic review of unmanned aerial vehicle application areas and technologies in the AEC domain. *J. of Information Technology in Construction*, **24**, 381–405. DOI: https://doi.org/www.itcon.org/2019/20
16. Ham, Y., Han, K.K., Lin, J.J., Golparvar-Fard, M. (2016) Visual monitoring of civil infrastructure systems via camera-equipped unmanned aerial vehicles (UAVs): A review of related works. *Visualization in Eng.*, **4**, 1. DOI: https://doi.org/10.1186/s40327-015-0029-z
17. Pant, S, Nooralishahi, P., Avdelidis, N.P. et al. (2021) Evaluation and selection of video stabilization techniques for UAV-based active infrared thermography application. *Sensors*, **21**, 1604. DOI: https://doi.org/10.3390/s21051604
18. Ciampa, E., De Vito, L., Rosaria Pecce, M. (2019) Practical issues on the use of drones for construction inspections. *J. of Physics: Conf. Series*, **1249**, 012016. DOI: https://doi.org/10.1088/1742-6596/1249/1/012016
19. Duque, L., Seo, J., Wacker, J. (2018) Synthesis of unmanned aerial vehicle applications for infrastructures. *J. Perform. Constr. Facil*., 32(**4**). DOI: https://doi.org/10.1061/(ASCE)CF.1943-5509.0001185
20. Rakha, T., Gorodetsky, A. (2018) A review of unmanned aerial system (UAS) applications in the built environment: Towards automated building inspection procedures using drones *Aut. in Constr*., **93**, 252–264. DOI: https://doi.org/10.1016/j.autcon.2018.05.002
21. Wu, W., Qurishee, M.A., Owino, J. et al. (2018) Coupling deep learning and UAV for infrastructure condition assessment automation. In: *Proc. of IEEE Inter. Smart Cities Conf., ISC2, 2018 Sept. 16–19, Kansas City, MO, USA*. DOI: https://doi.org/10.1109/ISC2.2018.8656971
22. Gu, J., Wang, Z., Kuen, J. et al. (2016) Recent advances in convolutional neural networks. *Pattern Recognition*, **77**, 354–377. DOI: https://doi.org/10.1016/j.patcog.2017.10.013
23. Gulgec, N.S., Takáč, M., Pakzad, S.N. (2017) Structural damage detection using convolutional neural networks. In: *Proc. of Conf. on Society for Experimental Mechanics Series*, 331–337. DOI: https://doi.org/10.1007/978-3-319-54858-6_33
24. Krizhevsky, A., Sutskever, I., Hinton, G. (2012) Imagenet classification with deep convolutional neural networks. *Advances in Neural Information Processing Systems*, 25(**2**), 1097–1105. DOI: https://doi.org/10.1145/3065386
25. Lee, S.Y., Tama, B.A., Moon, S.J., Lee, S. (2019) Steel surface defect diagnostics using deep convolutional neural network and class activation map. *Applied Sci.*, 9(**24**), 5449. DOI: https://doi.org/10.3390/app9245449
26. Tabernik, D., Šela, S., Skvarc, J., Skocaj, D. (2020) Segmentation-based deep-learning approach for surface-defect detection. *J. of Intelligent Manufacturing*, 31(**3**), 759–776. DOI: https://doi.org/10.1007/s10845-019-01476-x
27. Prappacher, N., Bullmann, M., Bohn, G. et al. (2020) Defect detection on rolling element surface scans using neural image segmentation. *Applied Sci.*, 10(**9**), 3290. DOI: https://doi.org/10.3390/app10093290
28. Li, J., Su, Z., Geng, J., Yin, Y. (2018) Real-time detection of steel strip surface defects based on improved YOLO detection network. *IFAC-PapersOnLine*, 51(**21**), 76–81. DOI: https://doi.org/10.1016/j.ifacol.2018.09.412
29. Wei, R., Song, Y., Zhang, Y. (2020) Enhanced faster region convolutional neural networks for steel surface defect detection. *ISIJ Inter.*, 60(**3**), 539–545. DOI: https://doi.org/10.2355/isijinternational.isijint-2019-335
30. Cha, Y.-J., Choi, W., Buyukozturk, O. (2017) Deep learning-based crack damage detection using convolutional neural networks. *Computer-Aided Civil and Infrastructure Eng.*, 32(**5**), 361–378. DOI: https://doi.org/10.1111/mice.12263
31. Hutchinson, T., Chen, Z. (2006) Improved image analysis for evaluating concrete damage. *J. of Computing in Civil Eng.*, 20(**3**), 210–216. DOI: https://doi.org/10.1061/(ASCE)0887-3801(2006)20:3(210)
32. Dung, C., Sekiya, H., Hirano, S. et al. (2019) A vision-based method for crack detection in gusset plate welded joints of steel bridges using deep convolutional neural networks. *Automation in Construction*, **102**, 217–229. DOI: https://doi.org/10.1016/j.autcon.2019.02.013
33. Shen, H.-K., Chen, P.-H., Chang, L.-M. (2013) Automated steel bridge coating rust defect recognition method based on color and texture feature. *Automation in Construction*, **31**, 338–356. DOI: https://doi.org/10.1016/j.autcon.2012.11.003
34. Xu, Y., Bao, Y., Chen, J. et al. (2018) Surface fatigue crack identification in steel box girder of bridges by a deep fusion convolutional neural network based on consumer-grade camera images. *Structural Health Monitoring*, 18(**3**), 653–674. DOI: https://doi.org/10.1177/1475921718764873
35. Prasanna, P., Dana, K.J., Gucunski, N. et al. (2016) Automated crack detection on concrete bridges. *IEEE Transact. on Automation Sci. and Eng.*, 13(**2**), 591–599. DOI: https://doi.org/10.1109/TASE.2014.2354314
36. An, Y.-K., Jang, K.-Y., Kim, B., Cho, S. (2018) Deep learning-based concrete crack detection using hybrid images. In: *Proc. of SPIE 10598 on Sensors and Smart Structures Technologies for Civil, Mechanical, and Aerospace Systems*, 1059812. DOI: https://doi.org/10.1117/12.2294959
37. Chow, J.K., Su, Z., Wu, J. et al. (2020) Anomaly detection of defects on concrete structures with the convolutional autoencoder. *Advanced Eng. Informatics*, **45**, 101105. DOI: https://doi.org/10.1016/j.aei.2020.101105
38. Miranda, J., Veith, J., Larnierc, S. et al. (2019) Machine learning approaches for defect classification on aircraft fuselage images acquired by an UAV. In: *Proc. of Fourteenth Inter. Conf. on Quality Control by Artificial Vision*, **1117208**. DOI: https://doi.org/10.1117/12.2520567
39. Avdelidis, N.P., Tsourdos, A., Lafiosca, P. et al. (2022) Defects recognition algorithm development from visual UAV inspections. *Sensors*, 22(**13**), 4682. DOI: https://doi.org/10.3390/s22134682
40. Ronneberger, O., Fischer, P., Brox, T. (2015) U-net: convolutional networks for biomedical image segmentation. In: *Proc. of the Medical Image Computing and Computer-Assisted In-*

tervention, 234–241. http://lmb.informatik.uni-freiburg.de/people/ronneber/u-net
41. Ren, J., Wang, H. (2023) Calculus and optimization. In: *Mathematical Methods in Data Science*. Chapter 3. Elsevier, 51–89. DOI: https://doi.org/10.1016/B978-0-44-318679-0.00009-0

ORCID
L.M. Lobanov: 0000-0001-9296-2335,
I.L. Shkurat: 0009-0003-1888-4203,
D.I. Stelmakh: 0000-0002-0412-9747,
O.P. Shutkevych: 0000-0001-5758-2396,
V.V. Savitsky: 0000-0002-2615-1793

CONFLICT OF INTEREST
The Authors declare no conflict of interest

CORRESPONDING AUTHOR
I.L. Shkurat
E.O. Paton Electric Welding Institute of the NASU
11 Kazymyr Malevych Str., 03150, Kyiv, Ukraine.
E-mail: innashkurat2909@gmail.com

SUGGESTED CITATION
L.M. Lobanov, I.L. Shkurat, D.I. Stelmakh, O.P. Shutkevych, V.V. Savitsky (2025) Enhancing large-scale structure diagnostics through UAV-based data and neural network analysis. *The Paton Welding J.*, **7**, 28–36.
DOI: https://doi.org/10.37434/tpwj2025.07.05

JOURNAL HOME PAGE
https://patonpublishinghouse.com/eng/journals/tpwj

Received: 06.03.2024
Received in revised form: 08.05.2024
Accepted: 26.06.2025

DOI: https://doi.org/10.37434/tpwj2025.07.06

RESEARCH OF THE EDDY-CURRENT RESONANCE METHOD FOR MEASURING THE THICKNESS OF THE CARBON FIBER REINFORCED PLASTIC LAYER ON METALLIC STRUCTURES

V.M. Uchanin[1], **O.G. Aleschenko**[1], **A. Savin**[2], **V.Ja. Derecha**[3]

[1]G.V. Karpenko Physico-Mechanical Institute of the NASU
5 Naukova Str., 79060, Lviv, Ukraine
[2]Nondestructive Testing Department,
National Institute of Research and Development for Technical Physics, Iasi, Romania
[3]SE "ANTONOV"
1 Mrija Str., 03062, Kyiv, Ukraine

ABSTRACT

The possibility of non-contact measurement of a carbon fiber reinforced plastic (CFRP) layer on structures made of non-magnetic aluminium alloy and ferromagnetic steel by the eddy current method was investigated. The research was carried out using flat specimens made of aluminium alloy D16T and ferromagnetic steel St20, on which a set of 1 mm thick flat plates made of CFRP were tightly laid. The number of the plates was varied to simulate the different thickness of CFRP layer. Parametric type eddy current probes (ECP) in the form of windings with 300 and 600 turns installed on an 8 mm diameter ferrite core were studied (magnetic permeability — 600). The ECP output voltages were investigated in the resonant mode at operating frequencies of 5, 8.5 and 20 kHz. The obtained dependences of voltage in the resonant circuit on the thickness of the CFRP layer became the basis for development of a device for non-contact measurement of the CFRP layer thickness on products made of aluminium alloys in the range of thicknesses up to 12 mm and ferromagnetic steel in the range of thicknesses up to 15 mm. The ability to measure the CFRP layer on metal structures is relevant not only for non-destructive inspection of their quality during production, but also for monitoring the integrity of such layered structures during their operation. Operational monitoring envisages preliminary determination of the thickness of CFRP layer in the reference points with the purpose of their further use as reference values. An increase in the results of measuring the thickness of the CFRP layer in the reference points during monitoring relative to the reference values will indicate the formation of delamination at the "metal–CFRP" boundary or between individual CFRP layers in operation.

KEYWORDS: carbon fiber reinforced plastic, aluminium alloy, ferromagnetic steel, eddy current probe, thickness measurement, resonant mode, operating frequency

INTRODUCTION

Composite materials (CM) are becoming widely applied for fabrication of the modern structures, in particular in the aviation and space industry, shipbuilding and automotive industry, which allows a significant reduction of the structure weight without loss of the load-carrying capacity and reliability and reducing the fuel consumption [1, 2]. CM began to be developed in the 50s of the previous century in order to replace the metal structural alloys. The main purpose consisted in combining two or more components with different physical properties to achieve characteristics, not inherent to each material separately. It should be noted that the scope of application of CM parts in the aviation and space industry is continuously increasing. In particular, at SC "Antonov" the CMs were used in the designs of the following aircraft: AN-26, AN-28, AN-32, AN-70, AN-71, AN-72, AN-74, AN-124 and AN-225 [3]. Famous leaders of aircraft manufacturing, such as Boeing, Airbus and Saab AB create aircraft, in which the quantity of CM of different types reaches 60 % by weight. A special place is occupied by fibrous CM, in which different matrices are used in combination with the fibrous filler. These could be fiberglass plastics, which can be considered dielectrics, as they are made of fiberglass and matrix based on epoxy resin. A widely used CM is the Carbon Fiber Reinforced Polymer (CFRP) Composite [4–6]. They can be multilayer with different orientation (for instance, 0°, 45°, 90°) of the carbon fibers in the different layers. CFRP is an almost ideal material for making aircraft as their strength is comparable with that of steel with the specific weight almost twice smaller than that of aviation aluminium alloys. The properties of such a multilayer structure are a combination of the high strength of the carbon fibers with the elasticity of the matrix filler. On the whole, CFRP have unique properties, to which, alongside the abovementioned ones, we can add a low coefficient of thermal expansion, high damping capacity and corrosion resistance [7]. CFRP also have a high cyclic loading resistance, but they perform better under one-dimensional loads. This, among other things, encourages combining CFRP with the tradi-

tional metals [8], as the aircraft structures are subject to more complex three-dimensional loading.

With wider acceptance of CM, the need for development of new NDT technologies is increased, as the currently available NDT methods and means do not always allow solving the respective complex of new tasks [9, 10]. NDT problems arise due to the diversity of damage and defects, which are inherent only to CM and which differ significantly from those characteristic for the traditional materials. Such characteristic CFRP defects include poor adhesion between the components, which leads to various types of delaminations, disturbance of fiber orientation in the different layers, etc.

On the whole, CFRP can be considered heterogeneous structures, which consist at least of two homogeneous components (carbon fibre and polymer matrix), having pronounced interfaces and differing essentially by their electrical and physical properties. As regards the eddy current method, it is important that the polymer matrix is a dielectric, and the carbon fiber has sufficiently high specific electrical conductivity (SEC). In addition, the CFRP fibrous structure creates different SEC in different directions, i.e. there exists at least uniaxial SEC anisotropy, which can differ in the different layers, because of the different direction of the carbon fibers. Here it is rational to use the approach proposed by us, which consists in introducing the notion of an effective medium for heterogeneous materials, the theory of properties of which is at the development stage. The effective medium approximation can be used for CFRP, when we will conditionally consider the heterogeneous material (CFRP) as a homogeneous (uniform) material with effective SEC, which depends on the quantitative composition of the components. It can be assumed that effective SEC, allowing for different SEC and anisotropy of SEC of the CFRP components, will be significantly greater than that of the polymer matrix, but smaller than for the carbon fiber. We used the effective medium approximation to study the possibility of determination of copper content in the copper ores, where the material heterogeneity is due to a low SEC of diorite (host rock) and chalcogenite (copper pyrite), which has much higher SEC [11]. We also used the notion of effective SEC for analysis of the influence of SEC anisotropy on the signal of eddy current probe (ECP) with circular windings [12]. The effective medium approach and the "effective coercive force" term were also used to study the parameters of the magnetic hysteresis loop of layered objects, consisting of layers with different magnetic characteristics [13].

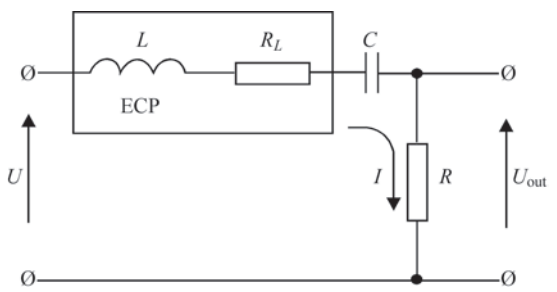

Figure 1. Schematic of connection of ECP of parametric type into the sequence oscillatory circuit

Lately there has been a problem of measuring the thickness of CFRP layer on metal structures, which is important not only for NDT of such layered structures in fabrication. A promising task is conducting the monitoring of CFRP integrity during the structure operation, which is related to the possible formation of delamination both at the CFRP interface with the metal base, and inside the CFRP. The known methods of measuring the CFRP thickness do not allow solving this problem. At first glance, the problem looks similar to that of measurement of the dielectric coating thickness. However, the known eddy current thickness meters for dielectric coatings are not suitable for measurement of CFRP thickness, because of its comparatively large SEC, and fast attenuation of the eddy currents at the used operating frequencies, respectively [14, 15]. The idea of solving the problem of measurement of a layer of metal-based CFRP consists in lowering the operating frequency, when the CFRP becomes "transparent" and its SEC will not have any significant influence on the depth of eddy current penetration.

THE OBJECTIVE

of the work is to study the possibility of measuring the CFRP thickness on structures and products from an aluminium alloy and ferromagnetic steel, based on application of ECP of parametric type in the resonant mode; determination of the optimal operating frequency and measurement range required for designing the appropriate instrument.

PARAMETERS OF THE STUDIED ECP, INVESTIGATION PROCEDURE, EXPERIMENTAL SPECIMENS

Investigations were performed using the resonant mode of eddy current testing, which envisages ECP connection into a series or parallel circuit with excitation from an external generator [1–17]. It is important that this allows separating the information component of the change in ECP impedance with tuning from the influence of uncontrolled parameter P_{ch}, which we will consider in the case of connecting the ECP into the series oscillatory circuit, the variant of which is given in Figure 1. The capacity and

resistance of the resonant circuit are selected so that output voltage U_{out} did not depend on changes in uncontrolled parameter P_{ch}.

The diagram of the impedance of the operating circuit, when mounting the ECP on a non-magnetic tested object (TO) with certain initial values of ECP impedance parameters (point P_0) is given in Figure 2.

The diagram (Figure 2) shows the contribution of each of the components into formation of the vector of the impedance of the series circuit (points *A*, *B*, *C* and P_0). The values of resistance *R* and capacitance *C* of the capacitor, and its reactance, respectively, are selected such that the vector of impedance Z_0, formed the right angle with tangent *TT* to the line of influence of uncontrolled parameter P_{ch} in point P_0. In this case, change of parameter P_{ch} within certain limits (point *D*) practically does not cause any change in the module of the circuit impedance. At the same time, a change in the controlled parameter P_c (transition to point *E*) essentially influences its module. Under the condition of a constant amplitude of input voltage and parameters of the circuit elements, the output voltage amplitude is determined only by the module of the circuit impedance. Therefore it will change only slightly in case of changes in uncontrolled parameter P_{ch}, but at the same time it will significantly depend on controlled parameter P_c. Similar possibilities for tuning from the uncontrolled parameter can be also obtained with ECP connection into the parallel oscillatory circuit.

Two ECPs of parametric type were made for investigation: one with winding of 300 turns, wound with 0.09 mm wire, and the other with 600 turn winding. In both the ECPs the windings are mounted at the end of a ferrite core 8 mm in diameter and 40 mm long. The relative magnetic permeability of the core material is 600. The outer diameters of ECP windings are 9.5 and 11 mm, respectively, winding length is 8 mm. ECP inductances in case of their location in "air" (at a distance from the electrically conducting material) were equal to 5.2 mH (ECP with 300 turns) and 15 mH (ECP with 600 turns).

Investigations were conducted using a flat rectangular specimen 3 mm thick of 10x10 mm size from D16T aluminium alloy and a similar specimen 2 mm thick of carbon steel St20. During investigations the metal specimens were tightly packed into a set of flat plates from CFRP, which were provided by SC "ANTONOV". The thickness of each plate was 1 mm. The different thickness of CFRP layer was simulated by the different number of plates (from 1 to 15). Investigations of changes in output voltage of the resonant circuit with CFRP layer were conducted at operating frequencies of 5; 8.5 and 20 kHz. The influence of the

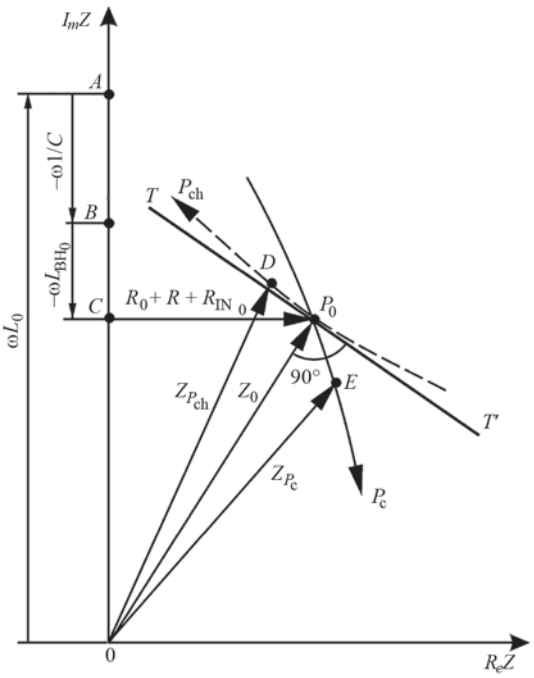

Figure 2. Influence of controlled P_c and uncontrolled P_{ch} parameter on the diagram of ECP complex resistances

thickness of CFRP layer on ferromagnetic steel St20 was studied at operating frequency of 5 kHz.

ANALYSIS OF THE DERIVED RESULTS

Figure 3, *a* gives the dependence of output voltage *U* in the resonant circuit on thickness h_c of the CFRP layer on the metal specimen from aluminium alloy at operating frequencies of 5; 8.5 and 20 kHz. Figure 3, *b* gives the dependence of sensitivity S_{hc} of the output voltage on thickness h_c of CFRP layer, which was assessed as the difference of output voltage amplitudes with 1 mm increase in the thickness of CFRP layer in the different parts of the range.

The given results (Figure 3) demonstrate the fundamental possibility of measuring the thickness of CFRP layer in up to 12 mm range on structures from aluminium alloys by the eddy current method at the selected operating frequencies. The output voltage amplitudes are increased with increase in thickness h_c with the studied operating frequencies, asymptotically approaching the output voltage values during ECP placement "in air", which are equal to 3.27; 6.95 and 8.1 V for the operating frequencies of 5; 8.5 and 20 kHz, respectively. One can see that the rate of increase is inversely proportional to the value of thickness h_c of CFRP, which is confirmed by the respective dependencies of sensitivity S_{hc} in Figure 3, *b*, the shape of which can be considered close to the exponent. Here, at operating frequency of 20 kHz, the maximum changes in output voltage (from 4.29 to 8.04 V) have been obtained with increase in CFRP thickness from zero value to 12 mm. For smaller op-

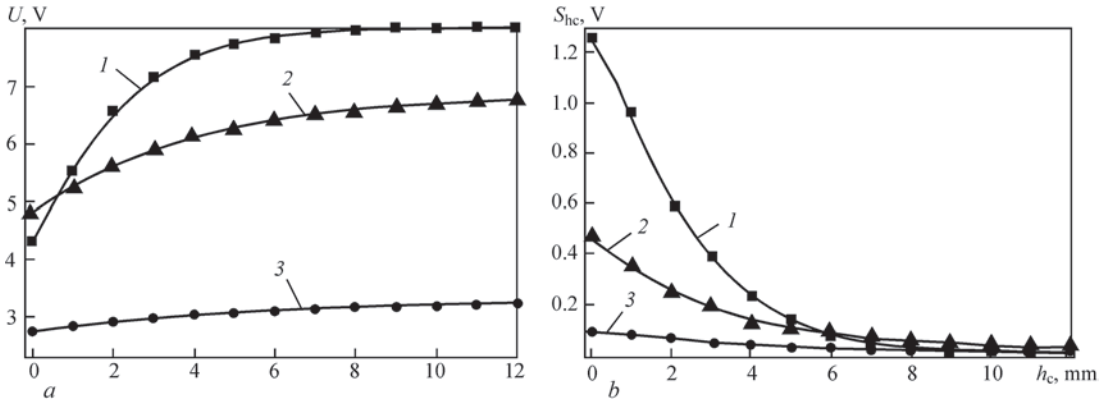

Figure 3. Dependence of output voltage U and respective dependencies of sensitivity S_{hc} on thickness h_c of CFRP layer for an aluminium alloy specimen at operating frequencies of: *1* — 20; *2* — 8.5, *3* — 5 kHz

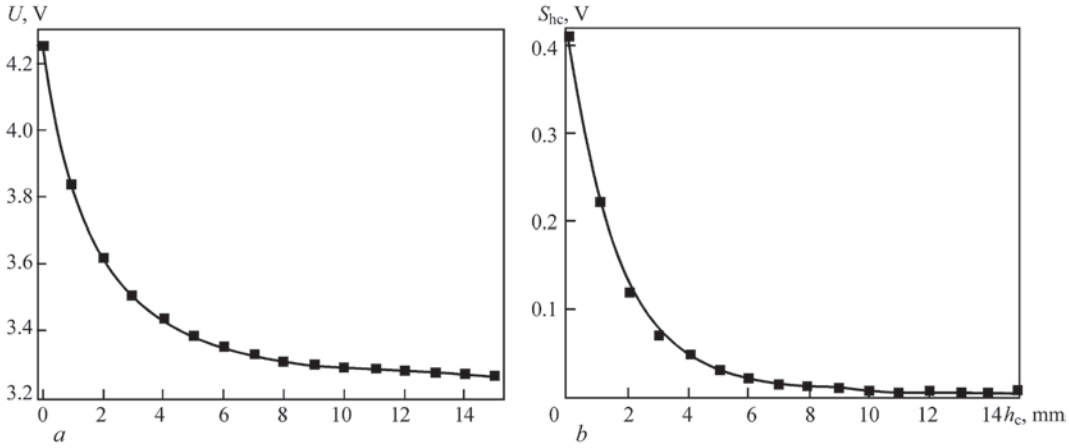

Figure 4. Dependence of output voltage U (*a*) and respective dependencies of sensitivity S_{hc} on thickness h_c of SFRP layer for a specimen from ferromagnetic steel St20 at operating frequency of 5 kHz

erating frequencies the respective voltage changes are significantly smaller: from 2.74 to 3.27 V at the frequency of 5 kHz and from 4.78 to 6.78 V at the frequency of 8.5 kHz. Thus, the operating frequency of 20 kHz can be considered optimal for measuring the CFRP thickness on aluminium alloy structures, the more so that the sensitivity at this operating frequency is the highest, particularly in the initial section in the range of changes in CFRP thickness.

Figure 4, *a* gives the dependence of output voltage U in the resonant circuit on thickness h_c of the CFPR layer on the specimen of St20 steel at operating frequency of 5 kHz, and Figure 4, *b* shows the respective dependence of sensitivity S_{hc} of output voltage on thickness h_c of CFRP layer on St20 steel.

The results given in Figure 4 also demonstrate the possibility of measurement of the thickness of CFRP layer on structures from ferromagnetic steel at operating frequency of 5 Hz. Here the possible range of measurement of CFRP thickness is up to 15 mm, which is attributable to a stronger influence of ferromagnetic steel on ECP inductance. One can see that the dependencies in Figure 3, *a* and Figure 4, *a* is symmetrical relative to the horizontal axis. However, unlike the previous dependencies for the non-magnetic aluminium alloy, here the output voltage amplitude decreases with increase of thickness h_c according to the law, close to the exponential one, asymptotically approaching the value of 3.25 V, corresponding to output voltage during ECP placement in "air". This is easily explained by the opposite influence of the non-magnetic and ferromagnetic metal on the change in ECP inductance. With ECP approaching the non-magnetic metal its inductance decreases, and, contrarily, ECP inductance increases at interaction with a ferromagnetic object. The rate of output voltage decrease is inversely proportional to the value of CFRP thickness h_c in the entire thickness range, which is confirmed by the respective curves of sensitivity S_{hc} in Figure 4, *b*. Let us recall that this property of proportionality between the rate of change of a quantity and the quantity proper is characteristics for an exponential dependence. It is obvious that such a non-linearity of the dependencies obtained in Figure 3, *a*, *b* should be taken into account during development of a resonant instrument for measurement of the thickness of CFRP layer on metal structures by introducing the linearization unit.

CONCLUSIONS

The eddy current method provides the possibility of non-contact measurement of the thickness of CFRP

layer on metal structures from aluminium alloys in the thickness range of up to 12 mm and those from ferromagnetic steels in the thickness range of up to 15 mm. Derived dependencies of voltage in the resonant circuit on CFRP thickness will be used for development of an experimental specimen of a device for non-contact measurement of the thickness of CFRP layer on metal structures.

Measurement of the CFRP layer on metal structures is relevant not only for NDT of the quality of layered structure of "metal–CFRP" type in production. The authors proposed an approach for application of the developed method for monitoring the integrity of layered structures of "metal–CFRP" type during their operation, which envisages previous determination of the thickness of CFRP layer in the reference points for use as reference values. Increase in the results of measurement of the thickness of CFRP layer during operational monitoring in the reference points relative to the predetermined reference values will be indicative of formation of delaminations at the "metal–CFRP" interface or between the individual CFRP layers.

REFERENCES

1. Pezzuti, E., Donnici, G. (2014) Structural composites for aircraft design. *ARPN J. of Eng. and Applied Sci.*, 9(**10**), 1889–1898.
2. Kondratiev, A.V., Kovalenko, V.A. (2011) Review and analysis of world tendencies and problems of expansion of application of polymer composite materials in the units of rocket-space technology. *Collect. of Design and Production of Flying Vehicle Structures*, 3(**67**), 7–18. Kharkiv, KhAI [in Russian].
3. Kiva, D. (2014) Stages of formation and beginning of the deployed application of polymer composite materials in passenger and transport aircraft structures (1970–1995). *Aviatsyonno-Kosmicheskaia Tekhnika i Tekhnologiya*, **6**, 5–16 [in Russian].
4. Ozkan, D., Gok, M.S., Karaoglanli, A.C. (2020) Carbon fiber reinforced polymer (CFRP) composite materials, their characteristic properties, industrial application areas and their machinability. *Adv. Struct. Mater.,* **124**, 235–253. DOI: https://doi.org/10.1007/978-3-030-39062-4_20
5. Othman, R., Ismail, N.I., Pahmi, M.A.A.H. et al. (2018) Application of carbon fiber reinforced plastics in automotive industry: A review. *J. Mech. Manuf.*, **1**, 144–154.
6. Wisnom, M.R. (1992) On the high compressive strains achieved in bending tests on unidirectional carbon-fibre/epoxy. *Composites Sci. and Technol.*, 43(**3**), 229–235. DOI: https://doi. org/10.1016/0266-3538(92)90093-I
7. (2011) *Machining technology for composite materials: Principles and practice*. Ed. by H. Hocheng. Elsevier Science.
8. Pramanik, A., Basak, A., Dong, Y. et al. (2017) Joining of carbon fibre reinforced polymer (CFRP) composites and aluminium alloys — A review. Composites: Pt A: *Applied Science and Manufacturing,* **101**, 1–29. DOI: http://dx.doi.org/10.1016/j.compositesa.2017.06.007
9. Savin, A., Steigmann, R., Stanciu, M.D. et al. (2024) Evaluation of the mechanical characteristics of CFRP composites and modeling of the delamination phenomenon. *The Paton Welding J.*, **12**, 30–34. DOI: https://doi.org/10.37434/tpwj2024.12.05
10. Sharabura, O.M., Muravsky, L.I., Kuts, O.G. (2024) Detection of circular subsurface defects in laminated composites using optical-acoustic nondestructive testing system. *Tekh. Diahnost. ta Neruiniv. Kontrol*, **4**, 18–22 [in Ukrainian]. DOI: https://doi.org/10.37434/tdnk2024.04.03
11. Uchanin, V.M., Rybachuk, V.G. (2022) Possibility of eddy current testing of low-conductive heterogeneous media. *Vidbir ta Obrobka Informatsii,* 50(**126**), 5–12 [in Ukrainian]. DOI: https://doi. org/10.15407/vidbir2022.50.005
12. Rybachuk, V.H., Uchanin, V.M., Kulynych, Y.P. (2022) Specific features of testing of anisotropic nonmagnetic materials by eddy-current probes with circular windings. *Mater. Sci.,* **57**, 452–458 [in Russian]. DOI: https://doi.org/10.1007/s11003-022-00565-2
13. Rybachuk, V.G., Uchanin, V.M. (2023) A recurrent formula for determination of the effective coercive force in layered ferromagnetic materials. *Mater. Sci.,* **58**, 533–539. DOI: https://doi. org/10.1007/s11003-023-00695-1
14. Dorofeev, A.L., Nikitin, A.Y., Rubin, A.L. (1978) *Induction thickness measurement*. Moscow, Energiya [in Russian].
15. (1986) *Non-destructive testing of metals and products:* Handbook. Ed. by G.S. Samoilovich. Moscow, Mashinostroenie [in Russian].
16. Polulyakh, K.S. (1980) *Resonant measurement methods*. Moscow, Energiya [in Russian].
17. Arsh, E.I. (1979) *Autogenerator methods and measuring instruments*. Moscow, Mashinostroenie [in Russian].

ORCID

V.M. Uchanin: 0000-0001-9664-2101,
A. Savin: 0000-0001-9863-3110,
V.Ja. Derecha: 0000-0003-1773-912X

CONFLICT OF INTEREST

The Authors declare no conflict of interest

CORRESPONDING AUTHOR

V.M. Uchanin
G.V. Karpenko Physico-Mechanical Institute of the NASU
5 Naukova Str., 79060, Lviv, Ukraine.
E-mail: vuchanin@gmail.com

SUGGESTED CITATION

V.M. Uchanin, O.G. Aleschenko, A. Savin, V.Ja. Derecha (2025) Research of the eddy-current resonance method for measuring the thickness of the carbon fiber reinforced plastic layer on metallic structures. *The Paton Welding J.*, **7**, 37–41. DOI: https://doi.org/10.37434/tpwj2025.07.06

JOURNAL HOME PAGE

https://patonpublishinghouse.com/eng/journals/tpwj

Received: 07.04.2024
Received in revised form: 12.05.2024
Accepted: 09.07.2025

DOI: https://doi.org/10.37434/tpwj2025.07.07

SMALL-SIZED PROCESS TEST FOR THE EVALUATION OF COLD CRACKING SUSCEPTIBILITY OF WELD METAL

L.S. Zakharov, A.R. Havryk

E.O. Paton Electric Welding Institute of the NASU
11 Kazymyr Malevych Str., 03150, Kyiv, Ukraine

ABSTRACT

A new weldability test has been developed that allows experimental determination of the critical preheating temperature necessary to prevent the formation of cold cracks in welded joints. The new geometry of the welding unit allows combining the bending stresses with normal transverse and longitudinal ones, increasing the test stiffness. The proposed test sample design has lower metal content and allows its repeated use. The weldability of hardening steels with different degrees of alloying was tested with application of the new test. The obtained test results are comparable to the results obtained in other studies of steel weldability and they have been recommended for use under production conditions.

KEYWORDS: welded joints, cold cracks, welding tests

INTRODUCTION

The most dangerous defect of the welded joints is cold cracks, occurring in welding the hardening steels. Their formation is due to the action of a complex of factors, in which some of the main ones are the structural stresses arising as a result of martensitic or bainitic transformation and presence of hydrogen in the metal. Appearance of cold cracks can be also promoted by formation of segregation interlayers, nonmetallic inclusions, etc.

The cold cracking process is essentially influenced by the welding modes, as the width of the HAZ, cooling rate of the weld and HAZ and level of postweld stresses depend on the welding mode. Diverse process tests are used to assess the susceptibility of the welded joint metal to cold cracking. Such process tests have their advantages over the full-scale tests of the welded structures, first of all, due to a lower metal content and cost [1].

Research on development of the methods for assessment of the cold cracking susceptibility of the welds began as far back as in the thirties of the last century and continues to this day [2–6]. Process tests differ by their design, dimensions, conditions and technology of welding, method of detection of the presence or absence of cracks, and crack resistance index. Each test envisages intensive development of one or several factors, causing the cold cracking. Such factors can be: hydrogen concentration; accelerated cooling to increase the degree of hardening; and higher stress level. Test samples of different design have different effectiveness of evaluation of the cold cracking susceptibility of the materials.

A large number of tests for assessment of the cold cracking susceptibility of steels and alloys are known in the world practice of studying their weldability [7]. Most of the tests, as well as the methods for calculated assessment of the cold cracking resistance were developed and tried out on the classical high-strength low-alloyed steels. Recently, however, the high-alloyed martensitic steels have been ever wider used, which often differ considerably by their reaction to the loads arising during welding.

The main feature of the high-chromium martensitic steels is the fact that their multiphase composition is at the junction of the austenitic, ferritic and martensitic structures. This causes significant difficulties in their welding, as, depending on the temperature and duration of heating and the cooling rate, the austenite and martensite can have “good” and “bad” modifications: lath or plate martensite; residual, reversed or allotriomorphic and Widmanstatten austenite, etc. In many cases when controlling the weldability it is necessary to use different variants of test stiffness.

For instance, study [8] showed that during testing of a weld of the modified martensitic 9Cr–Mo steel greater stiffness is required that for the standard tests. Contrarily, in the case of the martensitic-austenitic weld metal, which has higher ductility, cold cracks are observed at a low stiffness of the joint [9]. A similar tendency was revealed during application of welding consumables of Cr–Ni type [10].

Cold cracking tests provide qualitative (cracks/no cracks) or quantitative results (determination of test parameters for welds without cracks) for the studied combinations of the base material, filler material and welding parameters. Alongside the above-mentioned criteria, it is important to take into account the labour intensity of machining the blanks for the test samples, metal content and possibility of their further application. Many different testing methods have been developed to determine the potential risk of cracking by creating special conditions of the weld restraint, as is shown in numerous reviews on the subject [11].

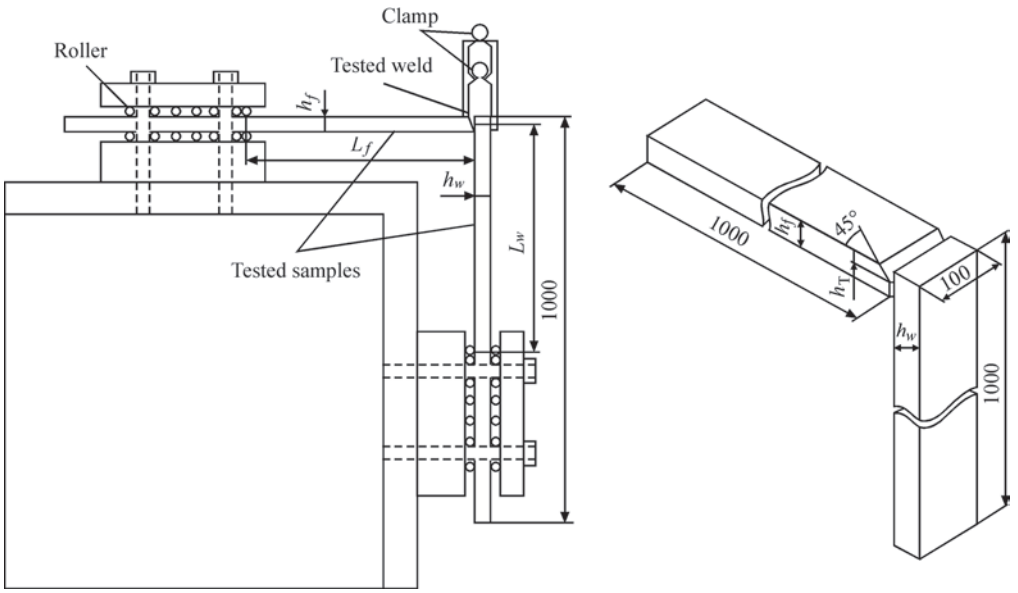

Figure 1. Design of CJC-test

The main part of the laboratory tests consists of a particular individual form of the fillet or butt weld, where higher stiffness is ensured either by the rigidity of the test samples proper, or by using anchor welds, bolts, jigs and other holding devices or their combination [12]. At the same time, it was established [13] that for a valid assessment of the influence of some factors on cracking in the welded joints and selection of an optimal procedure of structure welding during fabrication, the intensity of restriction during bending should be added during testing. However, the availability of laboratory tests, which best correspond to the probability of cold cracking, as the welds are simultaneously subjected not only to tension, but also to bending, is very limited.

Additional measurement of bending stresses together with the normal transverse and longitudinal stresses in the 3D testing facility BAM 2-MN [14] demonstrated a noticeable increase in the bending moment based on the restriction of angular deformation, particularly in the critical root zone, with accompanying risk of cracking. Values have been determined which exceed similar parameters of the slot test several times [15]. This is indicative of the fact that the bending stresses rise in welding and cause higher local residual stresses. Unfortunately, the complex design limits the application of such a test.

Sufficiently informative is the CJC-test [16], in which the stress-strain state of the joints is regulated by a special device, which allows combining the angular stress with the transverse one (Figure 1). A significant drawback of this test is its high metal content and the need to apply a complex jig.

The small-size test, in which bending stresses are recorded during welding, is the WIC test [1], which is used in welding pipelines from high-strength steels (Figure 2). Changing the height of the base plate stiffener, it is possible to model the high intensities of out-of-plane bending of the weld. The intensity of restriction in the transverse direction of welding can be changed, depending on the length of anchor welds between the WIC sample and the base plate [7]. As shown by practice, the test is sufficiently informative. However, the high metal content, significant cost of the unit mounting, complex fixation of the gap between the plates and one-time use of the unit should be noted.

THE OBJECTIVE

of the work is to develop a simplified design of the test sample to assess the weld metal susceptibility to cold cracking.

DEVELOPMENT OF THE DESIGN OF A SIMPLIFIED PROCESS TEST AND ITS PRACTICAL APPLICATION

We have conducted investigations on development of a cost-effective small-sized process test for the weld susceptibility to cold cracking. Both the plates

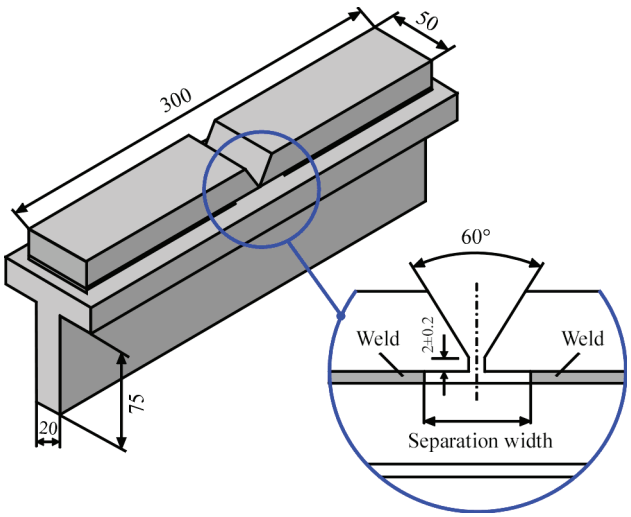

Figure 2. Design of WIC-test

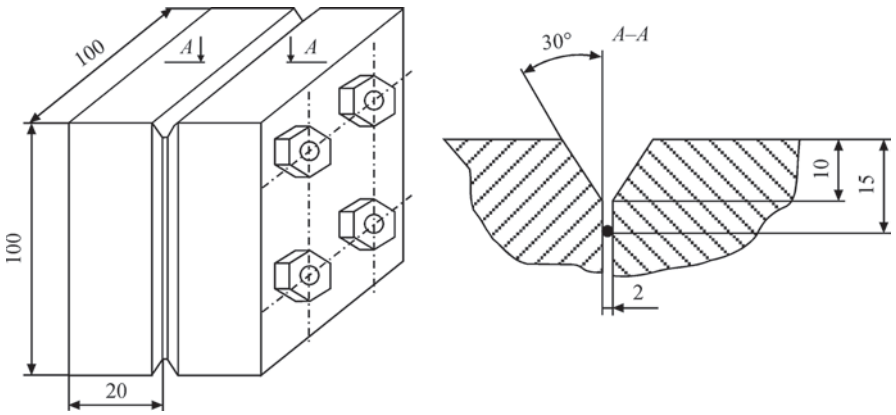

Figure 3. Design of the developed test sample

are fastened vertically in order to record the bending moment. It allows combining the bending stresses with the normal transverse and longitudinal ones. Test plates 20 mm thick are fastened using anchor bolts or jig (Figures 3, 4). The testing slots are located at the plate end faces. The slot geometry can be selected as required: *Y*, *V*, *U*-shaped and others. We selected the *V*-shaped groove, as cracks in the HAZ of the modern martensitic steels are practically absent.

The length of the reference weld in small-sized tests is selected within the range of 50–100 mm. The length of 85 mm was chosen, because in this case as it was determined [17], the highest both longitudinal and transverse residual stresses are ensured in the weld. The width of the slot between the plates is fixed with an insert of 2 mm diameter at 15 mm distance from the surface (Figure 1). If required, the test stiffness can be regulated by changing the distance from the fixing insert to the root zone. When making the test unit using anchor bolts, the groove can be made around its perimeter, which allows using one unit four times. In case of application of the jig (Figure 4), with a fixed width of the test plates it is possible to increase their length indefinitely, which also allows using one test unit many times.

The test joint design allows eliminating complex edge preparation, as for instance, in Tekken sample, which is particularly important with a large thickness of the materials being welded. More over, cutting out templates for metallographic analysis is greatly simplified. The sample metal is almost completely preserved for further use in multiple tests.

The requirements to sample preparation and procedure to be performed during application of the developed simplified process test were established by the recommendations of DSTU EN ISO 17642-2:2019 [18].

The test is used predominantly, but not exclusively, for martensitic alloyed and high-alloyed steels in coated-electrode arc and semi-automatic gas-shielded welding with solid and flux-cored wires. The plates are joined by bolts 20 mm in diameter. Under the condition of ensuring a uniform compression of the test sample elements and impossibility of the thread destruction, the tightening torque of all the bolts should be the same, being in the range of 100–184N·m, which is controlled by a torque wrench. Welding is performed in the downhand position, presence of cracks in the samples is controlled visually, or using a magnifying glass with ×2–4 magnification. The absence of cracks can be also confirmed during examination of transverse macrosections with magnification of approximately ×100–200.

Based on the proposed test, experiments were conducted to assess the cold cracking susceptibility of welded joints of martensitic 25Kh2MNFA, 15Kh5M and Kh10CrMoVNb91 (P91) steels 20 mm thick. Welding was performed with 3 mm electrodes. The material chemical composition is given in the Table 1.

Welding was conducted at reverse polarity direct current. The welding current source was VDU-505. Welding current was equal to 100 A. Before the start of welding, the electrodes were baked in the furnace at the temperature of 300 °C for 2 hours.

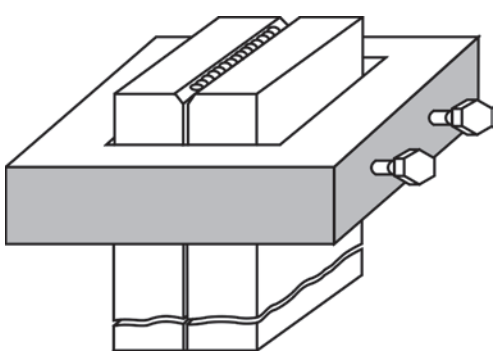

Figure 4. Design of the test sample with the jig

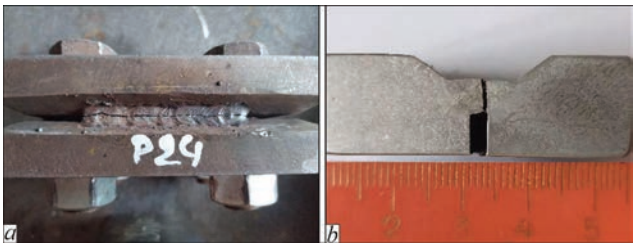

Figure 5. Cold crack in a sample in welding without preheating: top view (*a*), transverse section (*b*)

Table 1. Chemical composition of the used materials

Variant No.	Material grade	Weight fraction of elements, %						
		C	Si	Mn	Cr	Ni	Mo	V/Nb
1	Steel 25Kh2NMFA	0.24	0.17	0.50	2.20	1.50	0.50	0.2 V
	Electrodes Thernanit P 24 (EZ CrMo2VNb B42H5)	0.11	0.24	0.62	2.52	–	0.98	0.24 V
2	Steel 15Kh5M	0.11	0.4	0.6	4.8	0.6	0.34	–
	Electrodes TsL-17 (E 10Kh5MF)	0.07	0.45	0.90	4.5	–	0.65	0.25 V
3	Steel 10Kh9MFB (R91)	0.10	0.3	0.6	8.9	0.63	0.85	0.06 Nb
	Electrodes ANL-8 (E9018-B9)	0.09	0.13	0.72	9.15	0.52	0.83	0.05 Nb

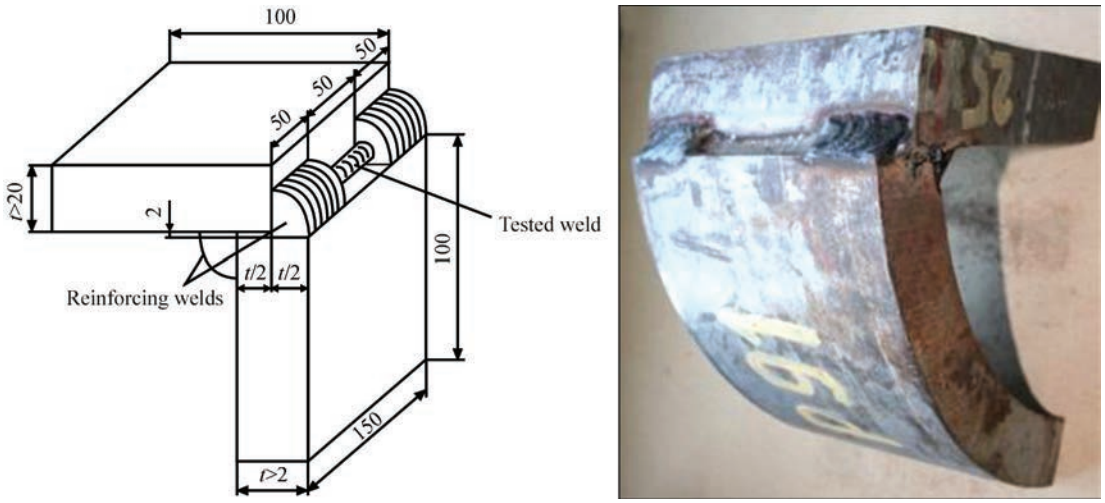

Figure 6. Angular sample design

Plate preheating before welding was conducted in a muffle electric furnace of SNOL type. Then the unit was moved to the welding table. Welding was begun after the planned temperature of the sample metal had been reached, which was controlled using a contact thermocouple. The test blocks were welded without preheating and with preheating with a step of 50 °C. The units welded without preheating cracked completely during testing of all the three steel grades (Figure 5).

Investigations conducted with application of the proposed test, showed that in the joints of the welded steels the cracks form solely in the weld metal. Cracks in the HAZ are absent with all the testing parameters.

Depending on the steel grades, the lowest critical preheating temperature to prevent cold cracking was determined as follows:

- in welding 25Kh2NMFA steel — 150 °C;
- in welding 15Kh5M steel — 300 °C;
- in welding R91 steel — 200 °C.

Critical preheating temperature derived in welding R91 steel, correlates well with the results of testing this steel using G-BOP test (200 °C) [19], which is considered the stiffest among the laboratory tests in the investigations. It is also noted there that in application of the Tekken test, a lower critical temperature of 150 °C was obtained. Similar results were derived in work [20].

To check the informativeness of the proposed test, a semi-scale testing of a higher stiffness was conducted. Plates of P91 steel 45 mm thick were welded at 90° angle with a 2 mm gap (Figure 6). It allowed eliminating the complex edge preparation, which is particularly important with large thickness of the materials being welded. More over, weld cutting out and preparation of templates for metallographic analysis are greatly simplified, the sample metal being preserved almost completely for further use.

The test weld was deposited after making the anchor welds from the inner and outer sides. Crack resistance was assessed by the critical preheating temperature. Performed testing showed that cracks in the reference weld, similar to application of the proposed test, are absent at the preheating temperature of 200 °C.

The considered approaches to testing the cold cracking susceptibility have been accepted in the research practice, and the obtained individual results have been used in development of the technologies of welding the elements of boiler, turbine, and hydroelectric power equipment from hardening bainitic and martensitic steels.

CONCLUSIONS

The design of a small-sized simplified process test for weld metal testing for cold cracking susceptibility was proposed. The test allows combining the bending stresses with the normal transverse and longitudinal stresses, providing a high stiffness of the experimental welded joints. A special feature of the test is its low metal content and the possibility of multiple application. The thermal conditions of welding of hardening heat-resistant steels

with bainitic and martensitic structure determined by the developed method, have been recommended for manufacturing the welded components of power equipment.

REFERENCES

1. North, T.H., Rothwell, A.B., Glover, A.G., Pick, R.J. (1982) Weldability of high strength line pipe steels. *Welding J.*, 61(**8**), 243–257.
2. Swinden, T., Reeve, L. (1938) Metallurgical aspects of the welding of low alloy structural steels. *Transact. Inst. Welding*, **1**, 7–18.
3. Leder, P.L.J. (1948) Factors influencing the weldability of high tensile alloy steels, and a new weld cracking test. *Proc. of the Inst. of Mechanical Eng.*, 159(**1**), 173–190.
4. Kurji, R., Coniglio, N., Griggs, J., Ghomashchi, R. (2017) Modified WIC test: An efficient and effective tool for evaluating pipeline girth weldability. *Sci. and Tech. of Welding and Joining*, 22(**4**), 287–299. DOI: https://doi.org/10.1080/13621718.2016.1232674
5. Schaupp, T., Schroeder, N., Schroepfer, D., Kannengiesser, T. (2021) Hydrogen-assisted cracking in GMA welding of high-strength structural steel — A new look into this issue at narrow groove. *Metals*, 11(**6**), 904. DOI: https://doi.org/10.3390/met11060904
6. Bourgeois, D., Alexandrov, B. (2022) Hydrogen-assisted cracking fracture analysis using high-speed camera and delayed hydrogen cracking test. *J. of Failure Analysis and Prevention*, **22**, 385–389. DOI: https://doi.org/10.1007/s11668-021-01308-2
7. Kannengiesser, T., Boellinghaus, T. (2013) Cold cracking tests — An overview of present technologies and applications. *Welding in the World*, 57(1), 3–37. DOI: https://doi.org/10.1007/s40194-012-0001-7
8. Karthikeyan, J., Varadharajan, R., Pitchaimuthu, K. (2015) Investigation of hydrogen assisted crack in welding by using Y-groove test. *Inter. J. of Eng. Research and Tech.*, 4(**10**), IJERTV4IS100187. DOI: https://dx.doi.org/10.17577/ijertv4is100187
9. Kasuya, T., Hashiba, Y., Inoue, H. et al. (2012) Cold cracking susceptibility of austenitic and martensitic weld metals. *Welding in the World*, 56(**9**), 76–84. DOI: https://doi.org/10.1007/BF03321383
10. Zenitani, S., Hayakawa, N., Yamamoto, J. et al. (2007) Development of new low transformation temperature welding consumable to prevent cold cracking in high strength steel welds. *Sci. and Tech. of Welding and Joining*, 12(**6**), 516–522. DOI: https://doi.org/10.1179/174329307X213675
11. Kurji, R., Coniglio, N. (2015) Towards the establishment of weldability test standards for hydrogen-assisted cold cracking. *The Inter. J. of Advanced Manufacturing Technology*, 77(**9–12**), 1581–1597. DOI: https://doi.org/10.1007/s00170-014-6555-3
12. Makarov, E.L. (1981) *Cold cracks in welding of alloyed steels*. Moscow, Mashinostroenie [in Russian].
13. Masubuchi, K., Ich, N.T. (1970) Computer analysis of degree of constraint of practical butt joints. *Welding J.*, 49(**4**), 166.
14. Lausch, T., Kannengiesser, T., Schmitz-Niederau, M. (2013) Multi-axial load analysis of thick-walled component welds made of 13CrMoV9-10. *J. of Materials Proc. Tech.*, 213(**7**), 1234–1240. DOI: https://doi.org/10.1016/j.jmatprotec.2013.01.008
15. Schroepfer, D., Kromm, A., Kannengiesser, T. (2017) Optimization of welding loads with narrow groove and application of modified spray arc process. *Welding in the World*, **61**, 1077–1087. DOI: https://doi.org/10.1007/s40194-017-0484-3
16. Ueda, Y., Nishimura, I., Iiyama, H., Chiba, N. (1977) Effects of intensity of bending restraint on lamellar tearing and root cracking in corner joint. *J. of the JWS*, 46(**7**), 408–415. DOI: https://doi.org/10.2207/qjjws1943.46.7_408
17. Sun, J., Hensel, J., Nitschke-Pagel, T., Dilger, K. (2019) Influence of restraint conditions on welding residual stresses in H-type cracking test specimens. *Materials*, 12(**17**), 2700. DOI: https://doi.org/10.3390/ma12172700
18. EN ISO 17642-2:2019: *Destructive tests on welds in metallic materials. Cold cracking tests for weldments-arc welding processes*. Pt 2: Self-restraint tests (EN ISO 17642-2:2005).
19. Chakraborty, G., Rejeesh, R., Ramana, O.V., Albert, S.K. (2020) Evaluation of hydrogen-assisted cracking susceptibility in modified 9Cr–1Mo steel welds. *Welding in the World*, **64**, 115–122. DOI: https://doi.org/10.1007/s40194-019-00812-2
20. Albert, S.K., Ramasubbu, V., Sundar Raj, S.I., Bhaduri, A.A. (2011) Hydrogen-assisted cracking susceptibility of modified 9Cr–1 Mo steel and its weld metal. *Welding in the World*, **55**, 66–74. DOI: https://doi.org/10.1007/BF03321309

ORCID

L.S. Zakharov: 0009-0006-4604-4561,
A.R. Havryk: 0000-0002-0793-2754

CONFLICT OF INTEREST

The Authors declare no conflict of interest

CORRESPONDING AUTHOR

L.S. Zakharov
E.O. Paton Electric Welding Institute of the NASU
11 Kazymyr Malevych Str., 03150, Kyiv, Ukraine.
E-mail: leza45@gmail.com

SUGGESTED CITATION

L.S. Zakharov, A.R. Havryk (2025) Small-sized process test for the evaluation of cold cracking susceptibility of weld metal. *The Paton Welding J.*, **7**, 42–46.
DOI: https://doi.org/10.37434/tpwj2025.07.07

JOURNAL HOME PAGE

https://patonpublishinghouse.com/eng/journals/tpwj

Received: 04.12.2024
Received in revised form: 13.01.2024
Accepted: 04.07.2025